

**High-Resolution Magic Angle Spinning
Proton Nuclear Magnetic Resonance
Study of Water absorbed in Single Wall
Carbon Nanotubes**

‘Study in Nano-Physics’

Dissertation

Zur Erlangung des akademischen Grades eines
Doktors der Naturwissenschaften

am Fachbereich Chemie
an der Universität Duisburg-Essen

vorgelegt von
Wassef Al Sekhaneh
aus Turra

Referent: Prof. Dr. Wiebren S. Veeman
Koreferent: Prof. Dr. Christian Mayer
Datum der mündlichen Prüfung: 17.07.2008

Die vorliegende Arbeit wurde in der Zeit von August 2001 bis 20.05.2008 im Fachgebiet der Physik. Chemie an der Universität Duisburg-Essen unter Anleitung vom **Herrn Prof. Dr. Wiebren.Veeman** angefertigt.

Hiermit bestätige ich, dass die vorliegende Arbeit nur mit den angegebenen Hilfsmitteln ohne fremde Hilfe angefertigt zu haben.

Essen, 20.05.2008

To my Mother and Father

To my Children

Marline

Ahmed

Maria

Miriam

Acknowledgements

This thesis is the testimony of the hard work of many people to whom I am most grateful. I would first of all like to thank my supervisor, Prof. Dr. of physics Wiebren S. Veeman at Duisburg-Essen University - for leading me into this novel exciting field and for his strong support to me during the past seven years, from the start till the end of my work. His continuing encouragement, patience and wisdom have been a tremendous asset during my preparation of my thesis. His attitude towards science as well as his expertise, endless optimism, his ability to find a new way to make things happen have shown me that anything can be achieved, if one really puts one's mind to it, really I am deeply grateful to him for his valuable discussions and suggestions, and thank him for his constructive critical reading and correcting of the manuscript.

Moreover, I would like to thank Prof. Dr. Christian Mayer for accepting the duty of the co-reference and Prof. Dr. Eckhard Spohr.

I heartily thank Dr. Ursula Dettlaff for her support from the start of my work in nanotubes till the end and for helping me to work in the Department of Prof. Dr. Klaus von Klitzing in the Max Max Planck Institute for Solid State Physics. She inspired me to step into the world of nanotechnology and nanotubes, and I really enjoyed her constructive discussions, her valuable suggestions, and her everlasting scientific enthusiasm.

Also I thank Prof. Dr. of physics Viera Skakalova in the Max Planck Institute for solid state physics; I want to thank all members of the group of Prof. Dr. of physics Siegmund Roth in the department von Klitzing. I thank also Dr. of physics Mrignayani Kotecha for her support and for the Matlab calculations helping in my work.

I have had the pleasure working with and learning from of them, thank you Zorro (Dipl. Ing. Manfred Zähres) and you Uwe (Dipl. Ing. Uwe Bachorski) for helping me with the nuclear magnetic resonance measurements, tuning, matching, the difficulty of the samples in NMR spectrometers. I also thank all friends and colleagues who have encouraged and assisted me in completing this work whose names were overlooked.

I would like also to thank all who helped me, Prof. Dr. M. Shabat at department of electro-optics at Duisburg- Essen university, Prof. Dr. Nazmi Al-Masri, Dr. Anwar Abo-Amer, Dr. Boris Epel, Dr. Mojgan Zandi, Dr. of physics Hala Al Khozondar, Dr. of physics Refa Al Khozondar, Dr. Holger Schmidt, Dr. Michael Vogt, Ms Janine Bauer, Mr. Daniel Schunk, Dr. Michael Hess, Schwark, Kirsten, Bergmann, Dirk, Tomic, Katarina, Wunderlich, Stefan, Linders, Jürgen, Beuermann , Sven, Christine Kallweit, Anik Deutmarg, Frau Gudrun Ciolek Ms Dahmani Habiba, Mrs Mokrani Khaoula, Mrs Mokrani Selma.

Finally, I wish to express my loving thanks to my children, Marline, Ahmed, Maria and Miriam, without whom none of this would have much meaning. I wish to thank them for sharing the highs and the lows of this work, but most of all for bringing love and joy to my life and always believing in me. To my brothers Wasfi Shaheen and Wael Al Sekhaneh. I would like also to thank all of my friends particularly Frau Helme Scholtz, Dr. Edna Hoffmann, Ms Lara Hoffmann and Gerda.

Summary

Single wall carbon nanotubes (SWNTs) have attracted scientific interest because of their fascinating physical and chemical properties and for their application in materials physics and the chemical industry.

The main topic of this Nano-Physics study is the investigation of the properties of water in carbon nanotubes, at different temperatures and at different concentrations of water by using the proton Magic Angle Spinning solid state nuclear magnetic resonance technique. Also the influence of metal clusters, which exist near the carbon nanotubes as a result of the synthesis, is investigated.

From the Nuclear magnetic Resonance investigations on water in single wall carbon nanotubes (SWCNTs), as described in this thesis, we can draw the following conclusions:

- Water is not absorbed inside SWCNTs, synthesized by the HiPCO method with a Fe catalyst, without further purification. The only water that is sorbed by the sample is water adsorbed at the outside of the nanotubes with a chemical shift of 4.6 – 4.8 ppm.
- Acid treatment removes the Fe clusters. After this treatment two water signals are detected, at 4.6 – 4.8 ppm and at 1.3 ppm.
- Temperature dependent solid state NMR spectra show that the water which is responsible for the 1.3 ppm line freezes at a temperature much lower than the freezing point of bulk water. This water is assigned to water absorbed inside the nanotubes.
- The NMR spectra as a function of the amount of water added to the SWCNT sample shows that the first water that is added to the sample, is absorbed in the tubes. In spite of the hydrophobicity of the inside of the carbon nanotubes water is absorbed due to the water surface tension.
- The investigated sample contains SWCNTs with diameters ranging from 0.9 to 1.1 nm and different chiralities. Also from theory it is expected that the tubes can be divided in metallic and semi-conducting tubes. Nevertheless the diameter range, the chirality and the conductivity of the tubes seem to have no effect on the chemical shift of absorbed water.
- A simple model calculation using the ring current contribution of each benzene ring of the SWCNT to the chemical shift of water located at the centre axis of the tube yields a water chemical shift value very close to the experimental value of 1.3 ppm.

CHAPTER ONE

1. MOTIVATION AND APPLICATIONS	1
1.1 Introduction	1
1.2 References to Chapter One	3

CHAPTER TWO

2. CARBON MATERIALS.....	5
2.1 Carbon Material	5
2.1.1 The Electronic Structure of the Carbon Atom	5
2.1.2 Hybridization of the Carbon Atom in Carbon Bonds	5
2.2 Carbon Forms	6
2.2.1 The Allotropic Forms of Carbon	7
2.2.1.1 Graphite	7
2.2.1.2 Diamond	8
2.2.1.3 Fullerenes	9
2.2.2 Fullerenes and Graphite related Structures	9
2.2.2.1 Fullerenes	9
2.2.2.2 Carbon Nanotubes	10
2.2.2.3 Peapods	12
2.2.3 Other Carbon Structures	12
2.2.3.1 Amorphous Carbon	12
2.3 References to Chapter Two	14

CHAPTER THREE

3. THE PHYSICAL PROPERTIES OF CARBON NANOTUBES.....	16
3.1 The structure of Carbon Nanotubes	16
3.2 Physics of Carbon Nanotubes	19
3.2.1 Lattice Structure	19
3.2.2 Reciprocal Space	20
3.2.3 Brillouin Zone	21
3.2.4 Band Structure	21
3.2.5 Lattice Structure of Graphene	22
3.2.6 Electronic Band Structure of Graphene	23
3.2.7 Hydrophobicity of Carbon Nanotubes	27

CHAPTER FOUR

4. SYNTHESIS, PURIFICATION AND CHARACTERIZATION OF CARBON NANOTUBES 32

4.1	<i>Synthesis of Carbon Nanotubes</i>	32
4.1.1	<i>Arc Discharge Technique</i>	33
4.1.2	<i>Laser Ablation</i>	37
4.1.3	<i>Chemical Vapor Deposition (CVD)</i>	38
4.1.4	<i>Decomposition of CO over Fe Catalyst</i>	39
4.2	<i>Purification</i>	40
4.2.1	<i>Oxidation in Air</i>	40
4.2.2	<i>Sonication of Carbon Nanotubes</i>	41
4.2.3	<i>Centrifugation</i>	41
4.2.4	<i>Acidic Treatments of SWCNTs</i>	41
4.3	<i>Characterization</i>	42
4.3.1	<i>Electron Microscopy</i>	62
4.3.1.1	<i>Microscopy of SWCNTs</i>	43
4.3.2	<i>Differential Scanning Calorimetry (DSC)</i>	49
4.3.2.1	<i>Differential Scanning Calorimetry of SWCNTs</i>	49
4.3.3	<i>Thermogravimetry (TGA)</i>	51
4.3.3.1	<i>Thermogravimetric Analysis of SWCNTs</i>	51
4.3.4	<i>Raman Spectroscopy</i>	54
4.3.4.1	<i>Raman Spectroscopy of SWCNTs</i>	55
4.3.5	<i>X-ray diffraction (XRD)</i>	57
4.3.5.1	<i>X-Ray Diffraction (XRD) Measurements of SWCNTs</i>	58
4.4	<i>References to Chapter Four</i>	61

CHAPTER FIVE

5. PROTON NUCLEAR MAGNETIC RESONANCE SPECTROSCOPY 65

5.1	<i>Introduction</i>	65
5.2	<i>Physics of Nuclear Magnetic Resonance Spectroscopy</i>	66
5.2.1	<i>The nucleus</i>	67
5.2.2	<i>Theoretical description of the Interaction of Spin with Magnetic Field</i>	68
5.2.2.1	<i>Quantum Mechanical Description</i>	68

5.2.2.2	<i>Classical Mechanical Description</i>	71
5.2.3	<i>The Rotating Frame of Reference</i>	74
5.2.4	<i>Radio-Frequency Pulses</i>	77
5.2.5	<i>Relaxation Process</i>	79
5.2.5.1	<i>Spin-lattice or Longitudinal Relaxation (T1)</i>	79
5.2.5.2	<i>Spin-spin or Transverse Relaxation (T2)</i>	81
5.3	<i>Solid State Proton NMR</i>	83
5.3.1	<i>Nuclear Spin Interactions in Solids</i>	83
5.3.1.1	<i>The Chemical Shift Interaction</i>	84
5.3.1.2	<i>The Dipolar Coupling</i>	89
5.3.2	<i>Magic Angle Spinning</i>	93
5.3.2.1	<i>Magic Angle Spinning and Line Broadening</i>	93
5.4	<i>Types of Line Broadening</i>	94
5.5	<i>References to Chapter five</i>	98

CHAPTER SIX

6.	THE NUCLEAR MAGNETIC RESONANCE TECHNIQUES.....	100
6.1	<i>Nuclear Magnetic Resonance (NMR) technique</i>	100

CHAPTER SEVEN

7.	RESULTS AND DISCUSSION.....	102
7.1	<i>Introduction</i>	102
7.2	<i>Experimental Results and Discussion</i>	103
7.3	<i>The chemical shift of water inside a single wall carbon nanotube</i>	121
7.4	<i>References to Chapter Seven</i>	136

CHAPTER EIGHT

8.	CONCLUSIONS.....	137
-----------	-------------------------	------------

LIST OF FIGURES

Figure (2.1)	Different types of hybridization of the carbon atom.	6
Figure (2.2)	<i>A view of graphite layers</i>	7
Figure (2.3)	<i>Diamond in the cubic form (left) and the hexagonal Lonsdaleite form (right).</i>	8
Figure (2.4)	<i>Different types of fullerene (to the right: C60).</i>	10
Figure (2.5)	<i>The rolling of a graphite sheet to form the SWCNT.</i>	10
Figure (2.6)	<i>Closed carbon nanotube: the hexagons and heptagons in a capped nanotube.</i>	11
Figure (2.7)	<i>Curved graphene varieties classified through the Gaussian curvature K</i>	11
Figure (2.8)	<i>Peapod, fullerene (C60) inside a single wall nanotube.</i>	12
Figure (2.9)	<i>SEM of peapod: C60 inside a single wall nanotube (permitted by J. Meyer).</i>	12
Figure (3.1)	<i>The structure of a nano tube generated by the chiral vector</i> $\vec{C}_h = 4\vec{a}_1 + 2\vec{a}_2$	16
Figure (3.2)	<i>Three different types of nano tubes can be constructed by folding along different lines: zig-zag for AB, armchair for A_1B_1 and chiral for A_2B_2.</i>	18
Figure (3.3)	<i>Carbon Nanotubes forms ;(a) armchair ;(b) zigzag ;(c) chiral.</i>	18
Figure (3.4)	<i>Real and reciprocal lattices in two dimensions</i>	20
Figure (3.5)	<i>The band structure of a direct-gap material</i>	22
Figure (3.6)	<i>Hexagonal lattice of a graphite sheet in real space (left) and at right the corresponding reciprocal space; the first Brillouin zone has been indicated by the shaded hexagon.</i>	23
Figure (3.7)	<i>The complete electronic band of graphene. The bonding (π) bands and antibonding (π^*) bands touch at K and K' points, calculated by using the tight-binding approximation..</i>	25
Figure (3.8)	<i>Three-dimensional plot of the graphene electron energy band structure near the Fermi energy E_F. The cones represent the low- and high-lying parts of the conduction and valence bands, touching at the K points of the Brillouin zone..</i>	25
Figure (3.9)	<i>(a) E-k diagram of a semiconducting carbon nanotube (b) E-k diagram of a metallic carbon nanotube .</i>	26
Figure (3.10)	<i>STM image of chiral nanotube (semiconductor) showing the</i>	27

	<i>hexagonal arrangement of the carbon atoms.</i>	
Figure (3.11)	<i>Metallic or semiconducting depends on which point the (0, 0) point is rolled to.</i>	27
Figure (3.12)	<i>Vertical equilibrium for a drop of a liquid on a solid</i>	28
Figure (4.1)	<i>Root growth mechanism for formation of a SWCNT</i>	33
Figure (4.2)	<i>Scheme of the SWCNT generator which has been used to produce arc-discharge material and the rod filled with powdered Ni, Y catalysts.</i>	35
Figure (4.3)	<i>Arc-discharge reactor used for synthesis of SWCNTs. The photographs describe the SWCNT reactor A) Chamber of the reactor, B) graphitic disc-cathode C) graphitic rod-anode which is filled with catalysts, D) complete view of the reactor.</i>	35
Figure (4.4)	<i>The appearance of SWCNTs in different deposits.</i>	36
Figure (4.5)	<i>The energy-dispersive X-ray (EDX) diagram of cluster metals used in generation of Carbon nanotubes (NiY).</i>	37
Figure (4.6)	<i>Illustration of a laser ablation apparatus.</i>	38
Figure (4.7)	<i>Basic schematic of the CVD apparatus used to grow nanotubes.</i>	39
Figure (4.8)	<i>SEM micrograph of raw SWCNT (NiY).</i>	43
Figure (4.9)	<i>TEM picture of a raw SWCNT (Fe) with 20% wt Fe impurity.</i>	44
Figure (4.10)	<i>SEM picture of the samples with 13wt % NiY impurity (raw sample).</i>	44
Figure (4.11)	<i>SEM micrograph of SWCNT (NiY) after first cycle of purification.</i>	45
Figure (4.12)	<i>SEM micrograph of SWCNT (NiY) after second cycle of purification.</i>	45
Figure (4.13)	<i>SEM micrograph of SWCNTs (NiY) after the third cycle of purification.</i>	46
Figure (4.14)	<i>SEM micrograph of SWCNTs (NiY) after heat treatment at 370 °C and centrifugation without any cycle of purification</i>	46
Figure (4.15)	<i>SEM micrograph of SWCNTs (Fe pure) after treatment at 370 °C and centrifugation without acidic treatment</i>	47
Figure (4.16)	<i>SEM micrograph of SWCNTs (Fe pure) after treatment at 370 °C and centrifugation without acidic treatment</i>	47
Figure (4.17)	<i>SEM micrograph of SWCNTs (Fe pure) after treatment at 370 °C and centrifugation and many acidic treatments to make the tube shorter.</i>	48
Figure (4.18)	<i>SEM micrograph of SWCNTs (Fe pure) after treatment at 370 °C and centrifugation</i>	48
Figure (4.19)	<i>Scheme of DSC Instrument</i>	49

Figure (4.20)	<i>The thermal behavior of opened SWCNT (Fe pure).</i>	50
Figure (4.21)	<i>The thermogravimetric analysis of raw SWCNTs by using nitrogen gas as a sample bath.</i>	51
Figure (4.22)	<i>The thermogravimetric analysis of SWCNTs oxidized at 350 C° determined in H₂ flowing gas.</i>	52
Figure (4.23)	<i>The thermogravimetric analysis of pure open HiPco SWCNTs under bath of nitrogen gas.</i>	53
Figure (4.24)	<i>The radial breathing mode (RBM) of SWCNT</i>	54
Figure (4.25)	<i>Raman spectrum of three SWCNT samples measured at laser wave line $\lambda = 632$ nm, showing the radial breathing mode (RBM), the D-band, the G-band, and the G'-band.</i>	56
Figure (4.26)	<i>Distributions of SWCNTs Radial breathing mode (RBM)</i>	56
Figure (4.27)	<i>The theory of X-ray diffraction (XRD)</i>	57
Figure (4.28)	<i>XRD diffractograms of SWNT are characterized at each stage by powder X-ray diffraction.</i>	58
Figure (4.29)	<i>The effect of centrifugation: X-ray diffraction patterns of the SWCNTs are heat-treated in air at 370 °C</i>	59
Figure (4.30)	<i>The effect of centrifugation: X-ray diffraction patterns of the SWCNTs heat-treated in air at 370 °C with more centrifugation</i>	60
Figure (5.1)	<i>The range of radio frequencies in the electromagnetic spectrum</i>	65
Figure (5.2)	<i>The classes of nuclear charge distribution</i>	67
Figure (5.3)	<i>Orientation of angular momentum \mathbf{J} in the magnetic field for proton with: $I = 1/2$ (b): Precession of the nuclear dipole of a proton around a double cone and energy states with α spin and β spin</i>	70
Figure (5.4)	<i>Energy levels of a nuclear spin with $I = 1/2$ as a function of the magnetic field \mathbf{B}_0.</i>	71
Figure (5.5)	<i>A static magnetic field applied to the nucleus causes it to precess at a rate dependent on the field strength and gyromagnetic ratio</i>	72
Figure (5.6)	<i>The positive precession for nuclei with negative gyromagnetic ratio (left), and negative precession for nuclei with positive gyromagnetic ratio (right)</i>	72
Figure (5.7)	<i>(Left): The nuclear magnetic moment μ rotates about the z axis of an applied magnetic field in the laboratory frame. (Right): The nuclear magnetic moment μ under the influence of an applied magnetic field appears stationary in the rotating frame of reference.</i>	74
Figure (5.8)	<i>Representation of a linearly alternating field as the sum of two</i>	77

	rotating fields ($B_{1(right)}$ clockwise) and $B_{1(left)}$ anticlockwise)	
Figure (5.9)	Magnetic fields in (a) the laboratory frame and (b) the rotating frame of reference	78
Figure (5.10)	The effect of (a) a pulse of arbitrary angle θ ; (b) after 90_x° pulse; (c) after 180_x° , all pulses are in the rotating frame of reference.	79
Figure (5.11)	Distribution of the spin population (a) at equilibrium and (b) after excitation by a 90° pulse.	80
Figure (5.12)	The longitudinal relaxation process.	81
Figure (5.13)	The transverse relaxation process (a) magnetization lies along the z axis; (b) Magnetization is tipped into x'y' plane; (c) spins begin to dephase; (d) spins are completely dephased.	82
Figure (5.14)	The transverse relaxation process.	82
Figure (5.15)	Schematic representation of B_0 field in PAS. Its orientation is defined by polar angles θ and φ	86
Figure (5.16)	Schematic representations of chemical shift in PAS (a) as non-spherical shape or ellipsoid where $\sigma_{11}^{PAS} = \sigma_{22}^{PAS} \neq \sigma_{33}^{PAS}$ and (b) spherical shape for isotropic where $\sigma_{11}^{PAS} = \sigma_{22}^{PAS} = \sigma_{33}^{PAS}$.	87
Figure (5.17)	Schematic representation of the typical powder patterns for various chemical shift tensors (a) Asymmetrical pattern for $\sigma_{11} \neq \sigma_{22} \neq \sigma_{33}$; (b) Powder spectrum for a chemical shift tensor with axial symmetry, where $\sigma_{11} = \sigma_{22} = \sigma_{\perp}$; (c) Powder spectrum for chemical shift tensor with axial symmetry, where $\sigma_{33} = \sigma_{22} = \sigma_{\perp}$.	88
Figure (5.18)	The polar angles θ and φ specifying the coupled spin pair in a magnetic field B_0 .	90
Figure (5.19)	The Magic angle spinning technique	94
Figure (5.20)	The change of a dipolar powder pattern under MAS conditions and the dependence on the spinning rate.	94
Figure (5.21)	(a) An inhomogeneous broadening and (b) a homogeneous broadening.	95
Figure (5.22)	The effect of MAS on: (a) Proton spectra of homogeneous lineshapes of Homonuclear dipolar interaction, (b) ^{13}C spectra of inhomogeneous linshapes of shielding tensor interaction (R. K. Harris)	96

Figure (5.23)	<i>Influence of the MAS spinning speed on the ^1H-NMR spectrum of adamantane, at room temperature and for a ^1H frequency of 300.13 MHz; spinning sidebands are marked with * [30]</i>	97
Figure (6.1)	<i>Pulse scheme of ^1H single pulse excitation.</i>	101
Figure (7.1)	<i>Temperature dependence of NMR spectra obtained by Ghosh et al</i>	103
Figure (7.2)	<i>^1H MAS-NMR spectra of SWCNT loaded with about 250 wt % water as a function of Fe impurity concentration (a) 5.9 wt %, (b) 13 wt % and (c) 20 wt %</i>	104
Figure (7.3)	<i>A different spinning rate is used to determine the center band of the ^1H MAS SWCNT (20% Fe impurity) spectrum, (yellow line shows the centerband).</i>	105
Figure (7.4)	<i>^1H MAS-NMR spectra of water in SWCNT with 5.9 % Fe as a function of the increasing amount of water (*= sidebands).</i>	107
Figure (7.5)	<i>^1H NMR spectra of a) solid water (ice) and b) liquid water at 400 MHz.</i>	108
Figure (7.6)	<i>^1H MAS NMR spectra of water in SWCNT HiPco (5.9% Fe) as a function of temperature with 43 wt % water (*= sidebands).</i>	110
Figure (7.7)	<i>^1H NMR spectra of water in SWCNT HiPco (5.9%Fe) as a function of temperature with 87 wt % water (*= sidebands).</i>	111
Figure (7.8)	<i>^1H MASNMR spectra of water in SWCNT HiPco (5.9% Fe) as a function of temperature with 43 wt % water (*= sidebands).</i>	112
Figure (7.9)	<i>^1H MAS-NMR spectra of water in SWCNT (5.9%Fe) as a function of temperature with 214 wt % water (*= sidebands).</i>	113
Figure (7.10)	<i>^1H MAS-NMR spectra of water in SWCNT (5.9%Fe) as a function of temperature with 318 wt % water (*= sidebands).</i>	114
Figure (7.11)	<i>The effect of water concentration on the proton spectra of SWCNT with 13 wt% Fe; at the left the total spectrum is shown, at the right the centerbands.</i>	115
Figure (7.12)	<i>^1H MAS-NMR spectra of water in SWCNT (13% Fe) as a function of temperature with 203 wt % water(*= sidebands).</i>	116
Figure (7.13)	<i>^1H MAS-NMR spectra of water in SWCNT (13% Fe) as a function of temperature with 278 wt % water (*= sidebands).</i>	116
Figure (7.14)	<i>^1H MAS-NMR spectra of water in SWCNT (13% Fe) as a function of temperature with 314 wt % water (*= sidebands).</i>	117
Figure (7.15)	<i>^1H MAS-NMR spectra of water in SWCNT Fe (20 % impurity) as a</i>	118

	<i>function of temperature with 110 wt % water, the spinning speed was 3250 Hz spectrum at different temperatures.</i>	
Figure (7.16)	<i>¹H MAS-NMR spectra of water in SWCNT Fe (20 % impurity) as a function of temperature with 180 wt % water, the spinning speed was 3250 Hz.</i>	119
Figure (7.17)	<i>¹H MAS-NMR spectra of water in SWCNT Fe (20 % impurity) as a function of temperature with 258 wt % water, the spinning speed was 3250 Hz.</i>	120
Figure (7.18)	<i>The dimension of water molecules relative to the nanotube.</i>	121
Figure (7.19)	<i>Schematic structure of a SWCNT bundle.</i>	122
Figure (7.20)	<i>The ring-current effect</i>	123
Figure (7.21)	<i>The magnetic field induced by a circular current loop located in x-y plane.</i>	124
Figure (7.22)	<i>The calculated isoshielding lines for a tube (8,8) $d \approx 1.06$ nm making the magic angle with \mathbf{B}_0.</i>	126
Figure (7.23)	<i>The calculated isoshielding lines for nanotubes with varying diameters</i>	134

LIST OF TABLES

Table (2.1)	<i>Hybridization state and orbitals of a central carbon atom.</i>	6
Table (4.1)	<i>Yield and appearance of different deposits in the arc-discharge reactor for nanotubes.</i>	36
Table (4.2)	<i>The distribution frequencies of SWCNT in the sample.</i>	55
Table (5.1)	<i>The properties of some common nuclei.</i>	68
Table (7.1)	<i>The isoshielding ring current contribution inside carbon nanotube, it varies inversely with the diameter of the tube.</i>	127

SYMBOLS AND ABBREVIATIONS

$\mathbf{a}_1, \mathbf{a}_2$	Primitive vectors of graphene
a_{c-c}	Inter-atomic distance between the nearest neighbors in the graphene plane
\mathbf{B}_0	Vector of the applied magnetic field.
\mathbf{B}_{eff}	Effective magnetic field
\mathbf{B}_1	Radio frequency pulse.
$\mathbf{b}_1, \mathbf{b}_2$	Basis vectors in reciprocal space of graphene
bcc	Body-centered cubic
\mathbf{B}_{loc}	Local magnetic field

C_h	Chiral vector
CSA	Chemical shift anisotropy
CVD	Chemical vapor deposition
HiPco	The high pressure catalytic decomposition of carbon monoxide
1D/2D/3D	One-/two-/three-dimensional
DOS	Density of states
d_{NT}	Nanotube diameter
Δp	A pressure difference.
$\Delta \omega_d$	Dipolar width
δ_{ij}	Kronecker delta function
ΔE	Energy difference between the two levels
δ_{iso}	Isotropic shift
δ	Shift tensor
DSC	Differential Scanning Calorimetry.
EDX	The energy-dispersive X-ray microanalysis diagram.
FID	Free induction decay
FWHM	Full width at half maximum
FID	Free induction decay
γ	Nuclear spin gyromagnetic ratio
γ_e	Electron gyromagnetic ratio
γ_{sl}	The solid-liquid interfacial tensions
γ_{sv}	The solid-vapor interfacial tensions
g	Lande' factor
\hat{H}	Hamiltonian
HOMO	The highest occupied valence band state
I	Nuclear spin vector
I	Spin quantum number
\vec{k}	Translational vector
k_B	Boltzmann factor
LUMO	The lowest unoccupied conduction state.
M	Magnetization
μ	Magnetic dipole moment
μ_0	Vacuum permeability constant
μ_B	Bohr magneton
$ m\rangle$	Eigenstates of the Zeeman Hamiltonian
MAS	Magic angle spinning
$^1\text{HMAS}$	Proton high resolution magic angle spinning.
MWNT	Multi-walled carbon nanotube
NMR	Nuclear magnetic resonance
(n, m)	Nanotube index from C_h
N_i	The population of the energy level i
PAS	Principal Axis System:
ppm	Parts per million (10^{-6})
ψ	Wave function
σ_{ii}	Shift tensor elements
σ	Chemical shift tensor
$\hat{\sigma}$	The chemical shielding tensor

τ	Time delay
SDS	Dodecylsulfate
SEM	Scanning electron microscope
SWCNT	Single-walled carbon nanotube
T	Temperature
T_1	Spin-lattice relaxation time
T_2	Spin-spin relaxation time
$T_{1\rho}$	Spin-lattice relaxation time in the rotating frame
TEM	Tunneling electron microscope
TGA	Thermogravometric analysis
TMS	Tetra methyl silane
ω_{ISO}	Resonance angular frequency of the isotropic shift
ω_O	Larmor frequency
ω_R	Magic angle spinning rate
XRD	X-ray diffraction

CONSTANTS AND FACTORS

g	=2.002319304386
h	= $6.626076 \cdot 10^{-34}$ Js = $4.135667 \cdot 10^{-15}$ eVs = $h/2\pi = 1.054571596 \cdot 10^{-34}$ Js
k_B	= $1.380658 \cdot 10^{-23}$ JK ⁻¹ = $8.617347 \cdot 10^{-5}$ eVK ⁻¹
μ_B	= $\gamma_e/g = 9.274015 \cdot 10^{-24}$ Am ²
μ_0	= $1.25663706 \cdot 10^{-6}$ mkg s ⁻² A ⁻² = $4\pi 10^{-7}$ T ² m ³ /J
N_A	= $6.0221415 \cdot 10^{22}$ mol ⁻¹
e	= $1.60217653 \cdot 10^{-19}$ C

1

Chapter One: Motivation and Applications

1.1 *Introduction*

Single wall carbon nanotubes (SWNTs) have attracted scientific interest because of their fascinating physical and chemical properties and for their application in materials physics and the chemical industry. The application includes modern electronic devices [1, 2], molecular storage like hydrogen storage [3], field emission displays [4], transistors [5], electromechanical devices such as actuators [6], supercapacitors or charge storage [7], nanocomposites, sensors [8, 9], nanometer-sized semiconductor devices [10] interconnects [11, 12], conductive high-strength composites, nanofluidic devices [13, 14], and one-dimensional cellular probes [15-17].

The main topic of this thesis is the investigation of the properties of water in carbon nanotubes, at different temperatures and at different concentrations of water by using the proton Magic Angle Spinning nuclear magnetic resonance technique. Also the influence of metal clusters, which exist near the carbon nanotubes as a result of the synthesis, is investigated.

Many scientists have been theoretically and experimentally trying to search the structure of confined water in carbon nanotubes [8-31]. Water in restricted spaces is expected to give unusual water behavior in the interior of nanotubes as well as in the grooves between adjacent nanotubes on the outside surface of SWCNT bundle, the behavior should differ from that of bulk water [24].

The interaction of water with SWCNTs has been investigated theoretically [26] and experimentally [27]. Hummer and co-workers [28] concluded from classical molecular dynamics (MD) simulations that water spontaneously fills the hydrophobic channel of SWCNTs with periodic transitions between filled and empty states. Byl [32] presents in his study by using vibrational spectroscopy evidence of a water phase inside single-walled carbon nanotubes that exhibits an unusual form of hydrogen-bonding at temperature between 123 -183 K.

In another study, Koga and co-workers [27] found that confined water inside SWCNT under axial pressure can show a first-order freezing transition (at 123 K) to hexagonal and heptagonal ordered ice in nanotubes, and a continuous phase transformation into solid-like square or pentagonal ice in nanotubes.

This dissertation has been organized in the following format. The **first Chapter** conducts the motivation and the applications of SWCNTs. **Chapter two** is devoted to the theoretical background of Carbon Materials, related to the present work. **Chapter three** describes the physical properties of Carbon Nanotubes. **Chapter four** presents synthesis, purification and characterization of carbon nanotubes by applying scanning electron microscopy, Raman spectroscopy, differential scanning calorimetry, thermal gravimetry and X-ray diffraction in order to analyze the main parameters related to single wall carbon nanotubes with close attention to their structure. **Chapter five** introduces the main theoretical parameters of Nuclear Magnetic Resonance spectroscopy focusing on Solid State proton nuclear magnetic resonance. **Chapter six** gives consideration to the main experimental techniques of proton NMR used in this work, namely, proton magic angle spinning nuclear magnetic resonance. **Chapter seven** is the most important part of the work and presents the results and discussion. The main findings of the thesis are summarized in **Chapter eight**.

1.2 References to Chapter One

- [1] S. Iijima, *Nature* **1991**, 354, 56.
- [2] T. W. Ebbesen, P. M. Ajayan, *Nature* (London) **1992**, 358, 220.
- [3] R. Bacon, *J. Appl. Phys.* **1960**, 31, 283.
- [4] W. Krätschmer, L. D. Lamb, K. Fostiropoulos, D. R. Huffman, *Nature* **1990**, 37, 354.
- [5] P. A. Ajayan, S. Iijima, *Nature* **1992**, 358, 23.
- [6] V. P. Dravid, X. Lin, Y. Wang, X. K. Wang, A. Yee, J. B. Ketterson, R. P. H. Chang, *Science* **1993**, 259, 1601.
- [7] S. Iijima, *Mater. Sci. Eng. B* **1993**, 19, 172.
- [8] A. G. Rinzler, J. Liu, H. Dai, P. Nikolaev, C.B. Huffman, F.J. Rodriguezmacias, P. J. Boul, A. H. Lu, D. Heymann, D. T. Colbert, R. S. Lee, J. E. Fischer, A. M. Rao, P. C. Eklund, R. E. Smalley, *Appl. Phys. A.* **1998**, 67, 29.
- [9] Y. L. Li, Y. D. Yu, Y. Liang, *J. Mater. Res.* **1997**, 12, 1678.
- [10] D. T. Colbert, J. Zhang, S. M. McClure, P. Nikolaev, Z. Chen, J. H. Hafner, D. W. Owens, P. G Kotula, C. B. Carter, J. H. Weaver, A. G. Rinzler, R. E. Smalley. *Science*, **1994**, 266, 1218.
- [11] T. Guo, P. Nikolaev, A. G. Rinzler, D. Tomanek, D. T. Colbert, R. E. Smalley, *J. Phys. Chem.* **1995**, 99, 10694.
- [12] A. Thess, R. Lee, P. Nikolaev, H. Dai, P. Petit, J. Robert, C. Xu, Y.H. Lee, S.G. Kim, A.G. Rinzler, D.T. Colbert, G.E. Scuseria, D. Tomanek, J.E. Fischer, R.E. Smalley, *Science* **1996**, 273, 483.
- [13] I. Wirth, S. Eisebitt, G. Kann, W. Eberhardt, *Phys. Rev. B* **2000**, 61, 5719.
- [14] H. Kataura, Y. Kumazawa, Y. Maniwa, I. Umezu, S. Suzuki, Y. Ohtsuka and Y. Achiba, *Synthetic Metals*, **1999**, 103, 2555
- [15] J. Kong, H. T. Soh, A. M. Cassell, C. F. Quate, H. Dai, *Nature* **1998**, 395, 878.
- [16] V. Ivanov, A. Fonseca, I. B. Nagy, A. Lucas, P. Lambin, D. Bemaerts, X. B. Zhang, *Carbon* **1995**, 33, 1727.
- [17] M. Yudasaka, R. Kikuchi, T. Matsui, Y. Ohki, S. Yoshimura, E. Ota, *Appl. Phys. Lett.* **1995**, 67, 17.

- [18] M. Shiraishi, T. Takenobua, A. Yamada., M. Ata, H. Kataura., *Chem. Phys. Lett.* **2002**, 358, 213.
- [19] J. Zhao., Buldum A., J. Han J., *Nanotechnology*, **2002**, 13, 195.
- [20] J. Wei, K. Shi, *Phys. Rev. Lett.* **2003**, 91, 015504.
- [21] G. Stan., et al., *Phys. Rev. B*, **2000**, 62, 2173.
- [22] X. Fan., et al., *Phys. Rev. Lett.*, **2000**, 84, 4621.
- [23] T. Meng-Hung, L. Hong-Min, T. Wen-Li, H. Yeukuang, *Rev. Adv. Mater. Sci.*, **2003**, 5, 302.
- [24] L. D. Gelb, K. E. Gubbins, R. Radhakrishnan, M. Sliwinska-Bartkowiak, *Rep. Prog. Phys.* 1999, 62, 1573.
- [25] Y. Gogotsi, J. A. Libera., A. Guvenc-Yazicioglu., C: M. Megaridis, *App. Phys. Lett.*, **2001**, 79, 1021.
- [26] Waghe Aparna, Jayendran C.R., Hummer G., *J. Chem. Phys.*, **2002**, 117, 10789.
- [27] Koga K., Gao G.T., Tanaka H., Zeng X.C., *Nature*, **2001**, 412, 802.
- [28] G. Hummer, J. C. Rasaiah, J. P. Noworyta, *Nature* **2001**, 414, 188.
- [29] A. I. Kolesnikov., J. M Zanotti., C. K. Loong., P. Thiyagarajan., A. P. Moravsky, R. O. Loufty., C. J. Burnham, *Phys. Rev. Lett.*, **2004**, 93, 035503.
- [30] C. Gordillo M., J. Marti. *Chem. Phys. Lett.*, **2000**, 329, 341.
- [31] Berezhkovskii A., Hummer G., *Phys. Rev. Lett.*, **2002**, 89, 064503.
- [32] Oleg Byl, Hummer G., Jin-Chen Liu, Yang Wai-Leung Yim, Wang, J. Karl Johnson, and John T. Yates, Jr.*, *JACS*, **08/29/2006**, Published on Web.

2

Chapter Two: Carbon Materials

In this chapter we present a review of carbon material, focusing on nanotubes as it forms the core of this study. The basic concepts, notions and physical properties of carbon materials will be discussed.

2.1 Carbon Material

2.1.1 The Electronic Structure of the Carbon Atom

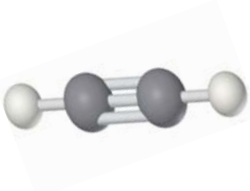
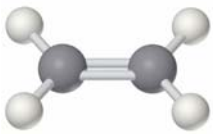
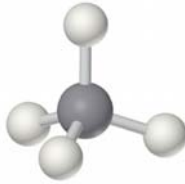
The carbon element [1] carries the C symbol and the atomic number of 6, i.e., the neutral atom has six protons in the nucleus and correspondingly six electrons. In addition, the nucleus includes six neutrons for the carbon ^{12}C (stable) isotope, seven neutrons for ^{13}C (NMR or magnetically active) and eight neutrons for ^{14}C (radioactive).

The electron configuration of the six carbon electrons in the ground state is $1s^2 2s^2 2p^2$, where two electrons are in the K shell (1s) and four in the L shell, two of which in the 2s orbital and two in 2p orbitals. Each carbon atom has four valence electrons. It should be stressed at this stage that no electron in an atom or a molecule can be accurately located. The electron wave function ψ is related to the probability of an electron being located in a given volume with the nucleus being the origin of the coordinate system. The function $\psi \psi^*$ has a mathematically finite value in space, but this value rapidly decreases at a distance of a few angstroms from the nucleus [2].

2.1.2 Hybridization of the Carbon Atom in Carbon Bonds [3-4]

In compounds containing carbon atoms, the 2s- and 2p- orbitals form linear combinations which lead to hybrid orbitals. The three possible combinations that occur are shown in table (2.1):

Table (2.1): Hybridization state and orbitals of a central carbon atom

Hybridization state and orbitals of a central carbon atom		
sp	sp²	sp³
Acetylene HC ≡ CH	Ethylene H ₂ C = CH ₂	Methane CH ₄
carbyne	graphite, fullerene, carbon nanotube	diamond
2 atoms bound to each carbon	3 atoms bound to each carbon	4 atoms bound to each carbon
Linear 	Trigonal planar 	Tetrahedral 

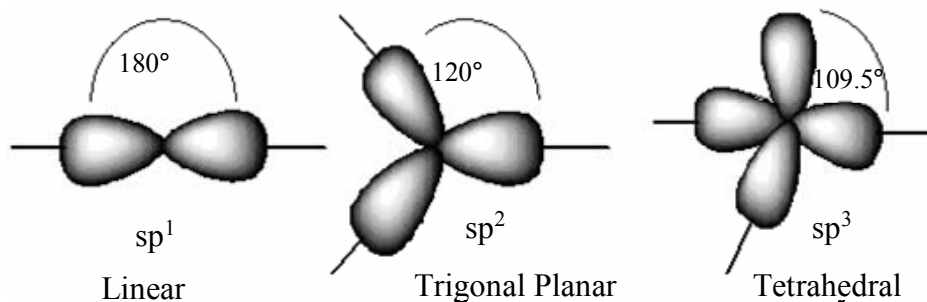


Figure (2.1): Different types of hybridization of the carbon atom.

2.2 Carbon Forms

The element carbon is widely found in nature in several forms. Some of these forms are composed entirely of carbon but have different physical structures and names: graphite, diamond, Lonsdaleite, fullerene, carbon nanotubes and amorphous carbon. The most important recent discovery was the exploration of the structure of the fullerenes in 1985

by Kroto et al. [5] who discovered the so-called C₆₀ molecule or Bucky-ball. Another new carbon form was discovered in 1991 by the Japanese electron microscopist Sumio Iijima[6] at the NEC Research Laboratory, when Iijima created an electric arc with DC current between two carbonic electrodes immersed in an argon gas atmosphere, he obtained the first carbon nanotube (CNT). Since that time, characterization studies and application of carbon nanotubes has been exploded due to the unique electronic and extraordinary mechanical properties of CNTs.

2.2.1 The Allotropic Forms of Carbon

The basic allotropic forms of carbon are graphite, diamond and fullerene.

2.2.1.1 Graphite

Graphite is a stable carbon structure with sp² hybridization, resulting in an extremely stable covalent bond between carbon and the in-plane nearest neighbor atoms. The carbon atoms in graphite are arranged in an open honeycomb pattern (Figure 2.2).

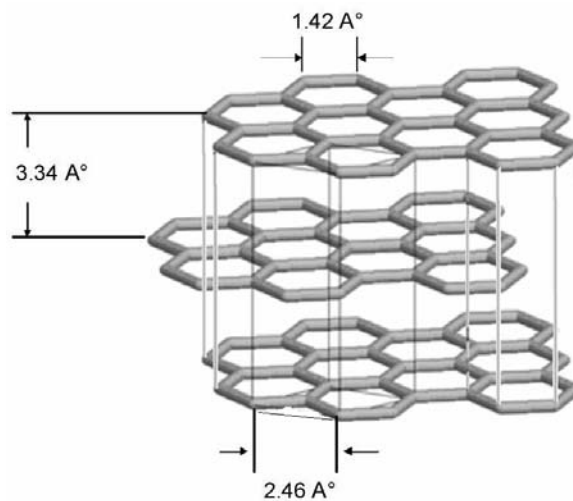


Figure (2.2): A view of graphite layers.

It is a layered structure, made up of parallel graphene planes, each carbon atom is connected to three neighboring atoms in the plane of hexagons by hybrid bonds of type sp², making an angle of 120° between them. The bond between atoms in each plane is strong; however, it is weak between atoms in different planes. The interaction between planes is caused by van der Waals forces [7].

The electronic properties of graphite are determined by the fourth carbon valence electron. Its p_z atomic orbital contributes to the molecular π - orbitals. The π - orbitals produce a cloud of electrons floating above and below the graphene plane. These electrons are mobile enough to make the material a good electrical conductor. Specifically designed defects in the carbon arrays can alter the physical properties of these arrays, including the electronic properties, in a controlled manner.

The inter-atomic distance between the nearest neighbors in the graphene plane a_{c-c} is 0.142 nm, and the in-plane lattice constant a is equal to 0.246 nm. The distance between planes is 0.334 nm (Figure 2.2) [8, 9].

2.2.1.2 Diamond

Diamond exists in a cubic and hexagonal form (Lonsdaleite) (Figure 2.3). In the most frequently found cubic form each carbon atom is bound to four other carbon atoms located at the corners of a regular tetrahedron with a cube edge length of $a_0 = 0.3567\text{nm}$.

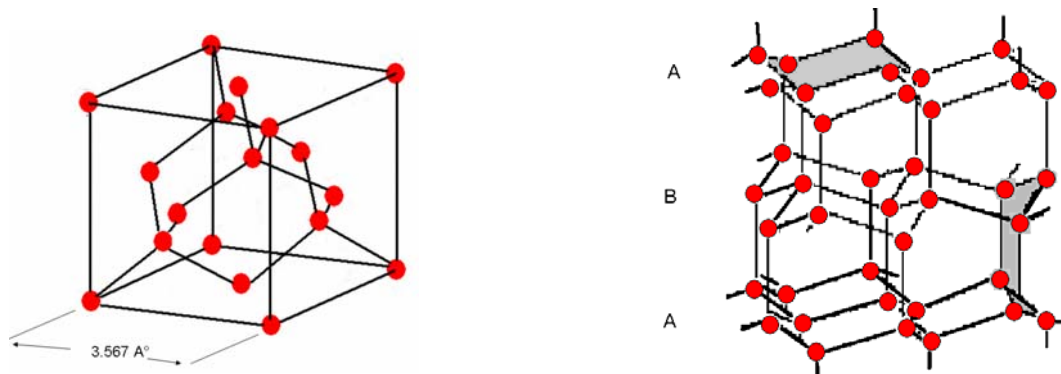


Figure (2.3): Diamond in the cubic form (left) and the hexagonal Lonsdaleite form (right).

The C–C covalent bond length is 0.1544 nm [10]. This is nearly 10% larger than in graphite. However the atomic density ($1.77 \times 10^{23} \text{ cm}^{-3}$ or $1.76 \times 10^{23} \text{ cm}^{-3}$) [11] is 56 % higher than in graphite. The crystal structure is of the zinc blend type (FCC) with a

diatomic basis. The second carbon atom is at position $(\frac{1}{4}, \frac{1}{4}, \frac{1}{4})$ in the unit cell and the lattice constant $a_0 = 0.3567$ nm (Figure (2.3 left) [11]. Diamond is the hardest natural material, with a Young modulus of up to 1250 GPa [1], due to the very strong covalent bonding between all atoms [1].

The attractive physical properties of diamond are determined by its structure. with a large band gap of 5.47eV diamond behaves as semiconductor material. Both the thermal conductivity and the mobility of conduction electrons of diamond are very large [1]. Diamond, like graphite (in-plane), has the highest thermal conductivity ($25 \text{ W}\cdot\text{cm}^{-1}\cdot\text{K}^{-1}$) as well as the highest melting point (4500 K). The hexagonal diamond (Lonsdaleite) has a wurtzite crystal structure (see Figure 2.3 right) and a C–C bond length of 0.152 nm. The gravimetric density of both types of diamond is $3.52 \text{ g}\cdot\text{cm}^{-3}$ [12 - 13].

2.2.1.3 Fullerenes

Fullerene molecules are closed, hollow, aromatic, spherical structures of C atoms made up of pentagonal and hexagonal faces [12]. The fullerenes form a group of spherical carbon molecules, synthesized by Kroto et al. in 1986 as a new form of carbon, in addition to the two already known forms of graphite and diamond [5].

2.2.2 Fullerenes and Graphite related Structures

2.2.2.1 Fullerenes

Experimental and theoretical work has shown that the most stable form of a carbon cluster of up to about 10 atoms is a linear chain [14]. For clusters that have 10 to 30 carbon atoms the ring is the most stable form [15]. Carbon clusters from 30 to 40 atoms are improbable and clusters above 40 atoms form cage structures. A stable structure is especially the C60 fullerene (Figure 2.4). The carbon atoms are located at the 60 vertices of a truncated icosahedron that has 90 edges and 32 faces, of which 12 are pentagons and 20 hexagons. The average nearest-neighbor C–C distance is with $a_{c-c} = 0.144$ nm equal to that in graphite. Each carbon atom is bonded to three other carbon atoms in a sp^2 -like bonding configuration. The curvature of the bonds in C60 is due to a rare blend of sp^2 and sp^3 hybridization [16]. Besides C60 newer and larger fullerene shapes were discovered with 84, 82, 76, 70 atoms see figure (2.4) [17 - 19].

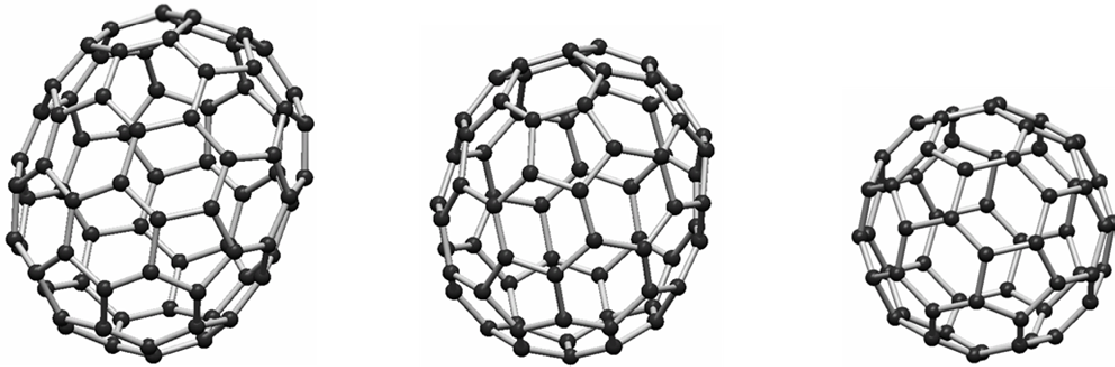


Figure (2.4): Different types of fullerene.

2.2.2.2 Carbon Nanotubes

Carbon nanotube is another new stable carbon form with sp^2 hybridization structure [[7, 9]. A single walled carbon nanotube (SWCNT) is usually described as a rolled up graphene sheet forming a hollow cylinder (figure 2.5) [6]. The tubular shells made of cylindrical graphite sheets of sp^2 carbon hexagonal rings are closed at each end with spherical fullerene caps containing pentagonal rings (Figure 2.6).

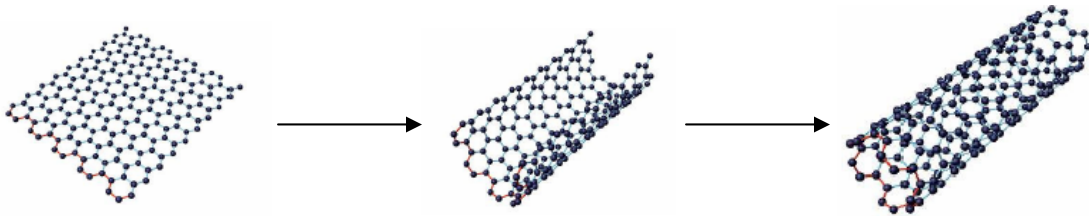


Figure (2.5): The rolling of a graphite sheet to form the SWCNT.

The curvature of the tube side-walls is due to the rolling of the sheet into the tubular structure, whereas the curvature in the end caps is due to the presence of pentagons in the otherwise hexagonal structure of the underlying lattice. The role of a pentagonal ring is to give a convex curvature to the surface, which helps in the closing of the tube at the two ends (figure 2.6) [6].

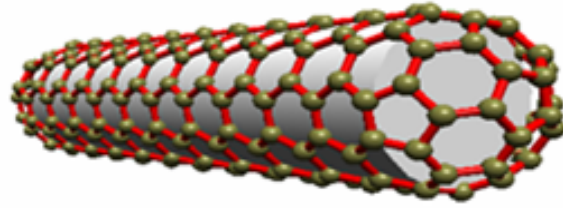


Figure (2.6): Closed carbon nanotube: the hexagons and heptagons in a capped nanotube.

Furthermore, the curved surface gives new properties to nanotubes, depending on the surface energy and the edge of graphene that contains dangling bonds before closing the tube. The total cohesion energy can be decreased by curving the sheets and forming closed structures such as nanotubes or fullerenes [7]. A topological classification for the curved surfaces has been proposed by Schwartz [7], who classifies the surface varieties by a mean and a Gaussian curvature H and K . These curvatures are proportional to the inverse of the length of graphene and the surface, respectively. There are three geometrical shapes as shown in figure (2.7):

$K > 0$ for spheres, $K = 0$ for planes or cylinders if $H = 0$ and $K < 0$ for a saddle configuration

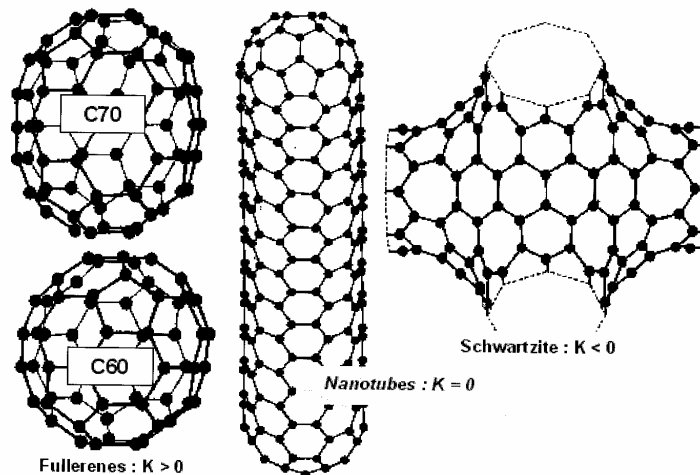


Figure (2.7): Curved graphene varieties classified through the Gaussian curvature K [7].

2.2.2.3 Peapods

Novel materials with modified electronic properties can be obtained when the innerspace of SWCNTs is filled with molecules or metal clusters. Even SWCNTs filled with fullerenes are possible. Such structures are called peapods (figures. 2.8 and 2.9).

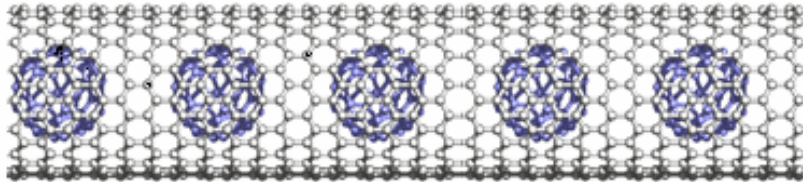


Figure (2.8): Peapod, fullerene (C60) inside a single wall nanotube.

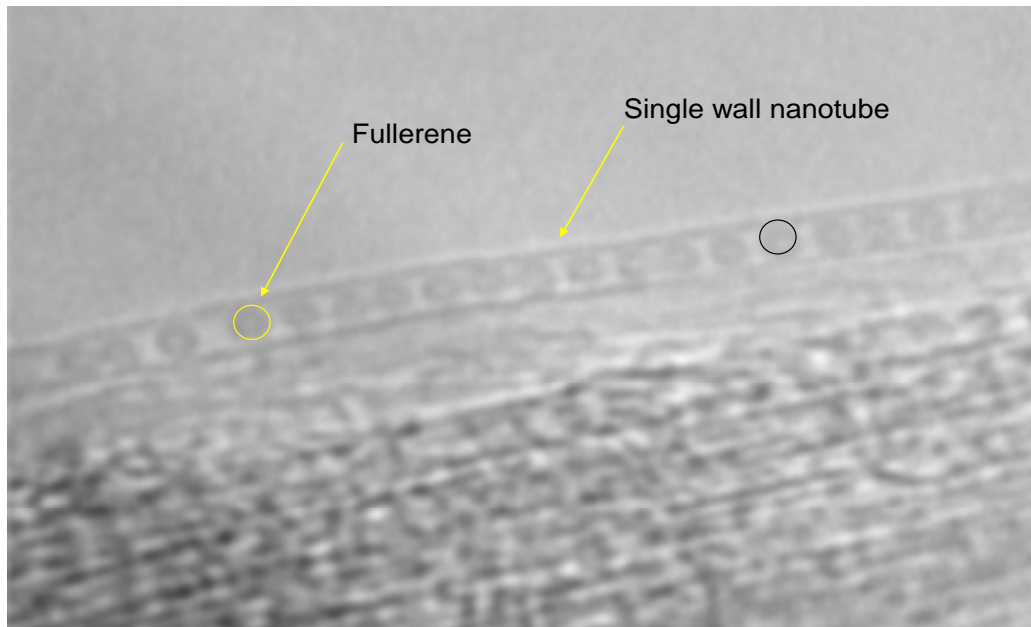


Figure (2.9): SEM of peapod: C60 inside a single wall nanotube (permitted by J.Meyer).

2.2.3 Other Carbon Structures

2.2.3.1 Amorphous Carbon

Amorphous carbon consists of a disordered network of carbon atoms with predominantly sp^2 bonds, with only approximately 10 % of sp^3 bonds and no sp bonds [10]. Amorphous

or glassy carbon has no long-range order but only some short-range order (~1 nm) that depends on the carbon bonding type (sp^2/sp^3) and the hydrogen content. Amorphous carbon can be produced by degradation of polymers at temperatures in the order of 900 to 1000 °C [10]. Coal and soot both belong to the class of amorphous carbon.

2.3 References to Chapter Two

- [1] H. O. Pierson. “*Handbook of carbon, graphite, diamond and fullerenes*”, Noyes, New Jersey, **1993**
- [2] P. L. Walker, Jr. and P. Thrower, eds., “*Chemistry and Physics of Carbon*”, Marcel Dekker, New York 1968.
- [3] T. W. Graham Solomons, *Understanding Organic Chemistry*, 8th Edition, Univ. of South Florida Craig B. Fryhle, Pacific Lutheran Univ., **2004**.
- [4] P. Delhaes: In *Carbon molecules and materials*, ed by R. Setton, P. Bernier and S. Lefrant (Taylor and Francis), **2002**
- [5] H. W. Kroto, J. R. Leath, S. C. O’Brien, R. F. Curl, R. E. Smalley, *Nature* **1985**, 318, 162.
- [6] M. S. Dresselhaus, G. Dresselhaus, R. Saito, “*Physics in Carbon Nanotubes*”, M. Endo, S. Iijima, M. S. Dresselhaus, Pergamon, **1996**, 27.
- [7] A. Loiseau, P. Launois, P. Petit, S. Roche, J.-P. Salvetat, *Understanding Carbon Nanotubes: From Basics to Applications (Lecture Notes in Physics)*, Springer, **2006**.
- [8] H. Zabel, S. A. Solin, *Graphite Intercalation Compounds I*, Springer Verlag, **1990**.
- [9] C. Dupas, Ph. Houdy, Marcel Lahmani, “*Nanoscience: Nanotechnologies and Nanophysics*”, Springer-Verlag. Berlin, **2007**.
- [10] T. W. Ebbesen, “*Carbon Nanotubes*”, CRC Press, Boca Raton, New York, **1997**.
- [11] E. Schaller, “*Study of the interface between highly oriented diamond and silicon*”, Dissertation, Université de Fribourg, Switzerland, **1996**.
- [12] B. McEnaney, “*Carbon Materials for Advanced Technologies*”, T. D. Burchell, Pergamon Amsterdam, **1999**, Chapter 1.
- [13] A. A. Valter, G. K. Eremenko, V. N. Kvasnytsya, Yu. A. Pokanov, “*Shockmetamorphogenic carbon minerals*”, Kyiv, Naukova Dumka, **1992**.
- [14] A. Kaldor, *J. Chem. Phys.* **1984**, 81, 3322.
- [15] H. S. Carman, R. N. Compton, *J. Chem. Phys.* **1993**, 98, 2473
- [16] M. Monthieux. *Carbon*, **2002**, 40, 1809.
- [17] H. W. Kroto, *Nature* **1987**, 329, 529

- [18] F. Diederich, R. Ettl, Y. Rubin, R. L. Whetten, R. Beck, M. Alvarez, S. Anz, D. Sensharma, F. Wudl, K. C. Khemani, A. Koch, *Science* **1991**, 252, 548.
- [19] B. L. Zhang, C. Z. Wang, K. M. Ho, *Chem. Phys. Lett.* **1992**, 193,

3

Chapter Three:

The Physical Properties of Carbon Nanotubes

This chapter describes the structure and physics of carbon nanotubes.

3.1 The Structure of Carbon Nanotubes

In order to understand the structure of a carbon nanotube, we have to consider how a graphite sheet can be rolled up into a cylindrical shape. The electronic properties of the tube depend on the orientation of the graphite plane with respect to the axis of the nanotube (see figure 3.1).

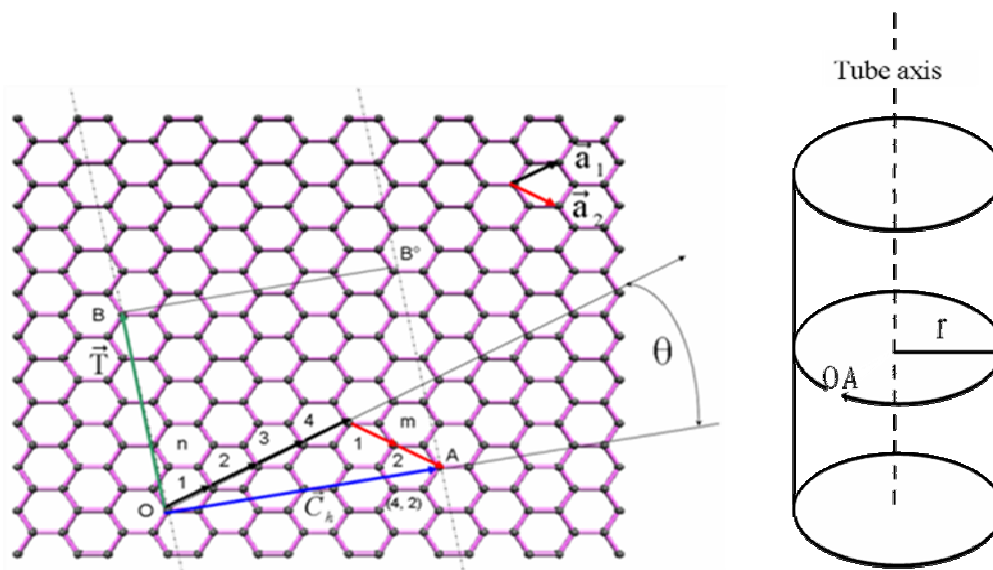


Figure (3.1): The structure of a nanotube generated by the chiral vector

$$\vec{C}_h = 4\vec{a}_1 + 2\vec{a}_2$$

In figure (3.1) it is demonstrated how a chiral vector $\vec{C}_h = m\vec{a}_1 + n\vec{a}_2$, specified by two vectors \vec{a}_1 and \vec{a}_2 and two integers m and n (in the Figure m=4 and n=2), defines the transformation of a sheet into a cylinder by bringing the points O and A, and B and B' together. Each cylinder that can be constructed is therefore defined by the two integer m

and n . The diameter of the constructed nanotube d_{NT} is related to the length of the chiral vector L :

$$\begin{aligned}
|\vec{C}_h|^2 &= \vec{C}_h \cdot \vec{C}_h = (n \vec{a}_1 + m \vec{a}_2) \cdot (n \vec{a}_1 + m \vec{a}_2) \\
&= n^2 \vec{a}_1 \cdot \vec{a}_1 + m^2 \vec{a}_2 \cdot \vec{a}_2 + 2nm \vec{a}_1 \cdot \vec{a}_2 \\
&= n^2 (\sqrt{3}a_{c-c})^2 + m^2 (\sqrt{3}a_{c-c})^2 + 2nm \sqrt{3}a_{c-c} \sqrt{3}a_{c-c} \cdot \cos 60 \\
&= (\sqrt{3}a_{c-c})^2 (n^2 + m^2 + nm)
\end{aligned} \tag{3.1}$$

where a_{c-c} is the C-C distance.

$$\begin{aligned}
|\vec{C}_h| &= \pi d_{NT} = \sqrt{3}a_{c-c} \sqrt{n^2 + m^2 + nm} \\
d_{NT} &= \frac{\sqrt{3}a_{c-c}}{\pi} \sqrt{n^2 + m^2 + nm}
\end{aligned} \tag{3.2}$$

The chiral angle θ is defined by:

$$\tan \theta = \frac{\sin \theta}{\cos \theta} = \frac{|\vec{C}_h \times \vec{a}_1|}{\vec{C}_h \cdot \vec{a}_1} \tag{3.3}$$

The scalar and vector products of Equation (3.3) are easily determined [1],

$$\begin{aligned}
\vec{C}_h \cdot \vec{a}_1 &= (n \vec{a}_1 + m \vec{a}_2) \cdot \vec{a}_1 \\
&= \frac{3}{2} a_{c-c}^2 (2n + m)
\end{aligned} \tag{3.4}$$

$$\vec{C}_h \times \vec{a}_1 = \begin{pmatrix} x & y & z \\ C_{hx} & C_{hy} & C_{hz} \\ \vec{a}_{1x} & \vec{a}_{1y} & \vec{a}_{1z} \end{pmatrix} \equiv \begin{pmatrix} x & y & z \\ C_{hx} & C_{hy} & 0 \\ a_{1x} & a_{1y} & 0 \end{pmatrix} = \tag{3.5}$$

$$\begin{aligned}
(\vec{C}_h \times \vec{a}_1)_z &= \det \begin{pmatrix} C_{hx} & C_{hy} \\ a_{1x} & a_{1y} \end{pmatrix} \times z \\
&= C_{hx} a_{1y} - C_{hy} a_{1x} \\
&= \frac{3\sqrt{3}}{2} m a_{c-c}^2
\end{aligned} \tag{3.6}$$

Then:

$$\theta = \arctan \frac{\sqrt{3}m}{2n+m} \quad 0 \leq \theta \leq \frac{\pi}{6} \quad (3.7)$$

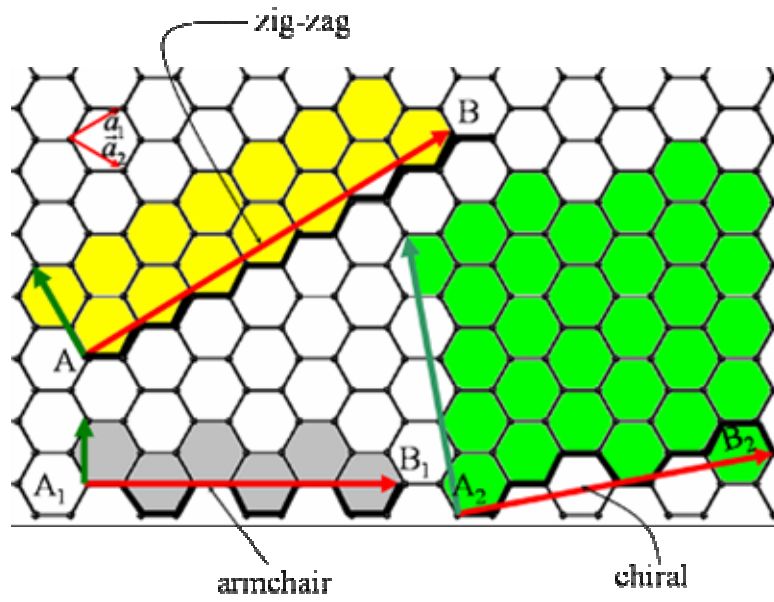


Figure (3.2): Three different types of nanotubes can be constructed by folding along different lines: zig-zag for AB, armchair for A_1B_1 and chiral for A_2B_2 .

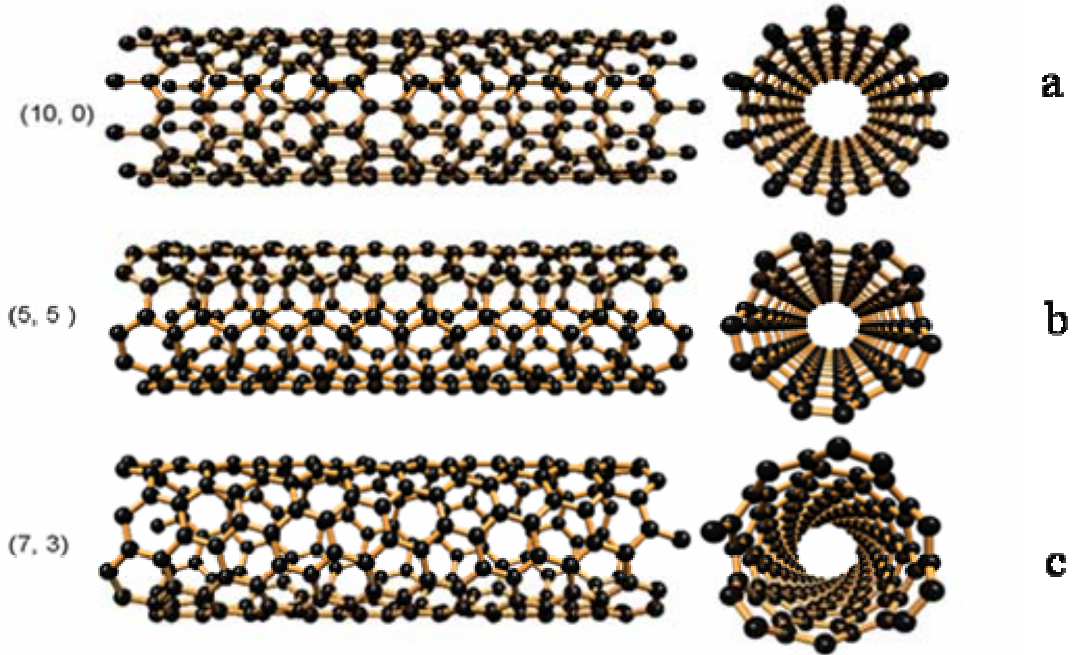


Figure (3.3): Carbon Nanotubes types ;(a) armchair ;(b) zigzag ;(c) chiral.

Three possible types of nanotubes, shown in figures (3.2) and (3.3), result from a different rolling of the graphite sheet. The first type corresponds to $m = 0$, $\theta = 0^\circ$ or $(n, 0)$ and is called “zigzag”; the second one corresponds to $m=n$, $\theta = 30^\circ$ or (n, n) and called “armchair”; and the last type is equivalent to $m \neq n$, $0^\circ < \theta < 30^\circ$ or (n, m) and called “chiral” [1-2].

Graphite sheets can form single wall (SWCNT) or multi wall tubes (MWCNT). The (MWCNT) are made of concentric cylinders placed around a common central hollow, with a spacing between the layers close to that of the interlayer distance in graphite (0.34 nm). This interlayer spacing in MWCNT is slightly larger than the single-crystal graphite value (0.335 nm) since in these tubes there is a severe geometrical constraint when forming the concentric seamless cylinders while maintaining the graphite spacing between them [3-5].

3.2 Physics of Carbon Nanotubes

The electronic properties of solids are to a high degree determined by the so called electronic band structure. This band structure determines whether a material is an insulator or a (semi) conductor. To understand the band structure it is essential to introduce some concepts of solid state physics.

3.2.1 Lattice Structure [6-7]

Any crystalline solid consists of an infinite periodic array of building blocks; each building block, called a basis, consists of an atom, a molecule, or a group of atoms or molecules. This specific periodic array with an arrangement and orientation that appears exactly the same at each lattice point is called a ‘*Bravais lattice*’ and can be defined in terms of three fundamental translational vectors $\vec{a}_1, \vec{a}_2, \vec{a}_3$. An arbitrary translation vector \vec{R} has the form:

$$\vec{R} = n_1\vec{a}_1 + n_2\vec{a}_2 + n_3\vec{a}_3 \quad (3.8)$$

where n_1, n_2 , and n_3 are integers.

3.2.2 Reciprocal Space [6-7]

In addition to the real-space lattice, a reciprocal space lattice with the translation vector \vec{k} can be defined:

$$\vec{k} = k_1\vec{b}_1 + k_2\vec{b}_2 + k_3\vec{b}_3 \quad (3.9)$$

and

$$\vec{b}_j \cdot \vec{a}_i = 2\pi\delta_{ij}, \quad \text{for } i, j = 1, 2, 3 \quad (3.10)$$

where, δ_{ij} is the Kronecker delta function, being 1 when $i=j$ and 0 otherwise, and:

$$\begin{aligned} \vec{b}_1 &= 2\pi \frac{\vec{a}_2 \times \vec{a}_3}{\vec{a}_1 \cdot \vec{a}_2 \times \vec{a}_3} \\ \vec{b}_2 &= 2\pi \frac{\vec{a}_3 \times \vec{a}_1}{\vec{a}_2 \cdot \vec{a}_3 \times \vec{a}_1} \\ \vec{b}_3 &= 2\pi \frac{\vec{a}_1 \times \vec{a}_2}{\vec{a}_3 \cdot \vec{a}_1 \times \vec{a}_2} \end{aligned} \quad (3.11)$$

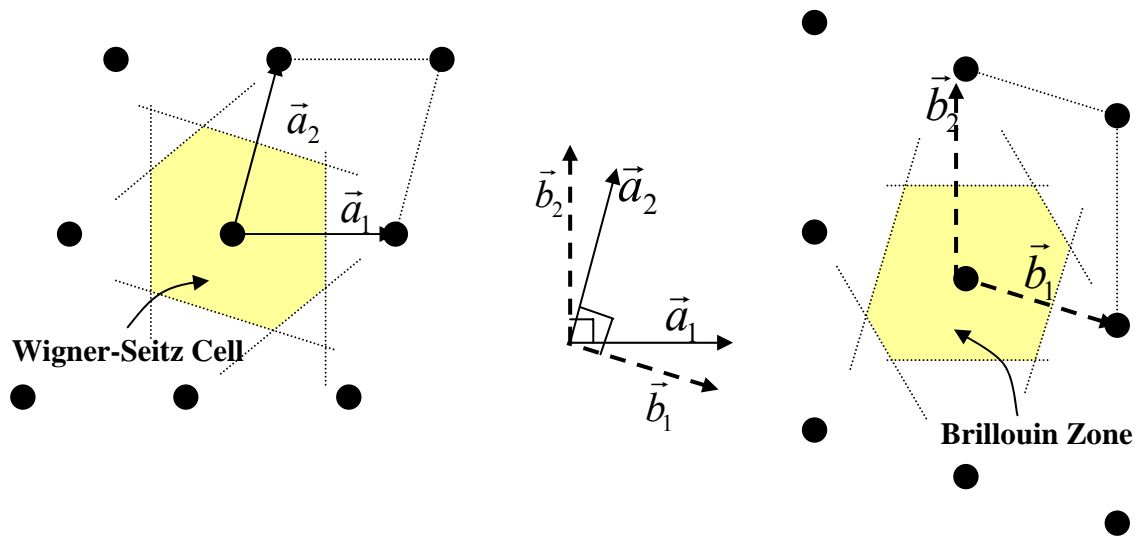


Figure (3.4): Real and reciprocal lattices in two dimensions

3.2.3 Brillouin Zone [6-7]

A Wigner-Seitz cell about a certain lattice point is the region of space that is closer to that point than to any other lattice point. The Wigner-Seitz cell that, when translated through

all vectors in a Bravais lattice, just fills all of space without either overlapping itself or leaving voids, is called a '*primitive cell of the lattice*'. Such cells are also defined in reciprocal space. The first Brillouin zone is the Wigner-Seitz primitive cell of the reciprocal lattice.

3.2.4 Band Structure [6-7]

For the discussion of the electronic band structure of a crystalline solid two starting approaches are possible: either the free electron model or the tight-binding model.

In the free electron model the valence electrons of the atoms constituting the solid in first approximation are considered to be completely free and the electrons have only kinetic energy. The possible valence electron energy levels then form one continuous band of energies. When the interaction of the electrons with a potential field due to the regular array of atoms is taken into account, this continuity in the band is broken and a sequence of electron energy bands, possibly separated by forbidden zones, is produced.

In the other approach, the tight-binding model, the electrons are in first order localized near the individual atoms, which would present the correct situation when the distance between the individual atoms is infinite. By decreasing the distance between the atoms (decreasing the lattice constant) the infinitely narrow atomic energy levels broaden into bands. The tight-binding approximation clearly shows the connection between the number of atoms and the number of states in one band. A band formed from q atoms contains $2q$ states, q bonding and q anti-bonding combination states. If each atom contributes two electrons, the lower half of the band is full and cannot contribute to electrical conductivity, at least when there is no overlap with other bands. Thus the bands formed from the filled electronic orbitals of the atoms normally do not lead to conductivity, unless a band resulting from the overlap of empty atomic orbitals is within kT of the filled band.

The difference in energy between the highest filled valence band and the lowest level of the first empty band (conduction band) is known as the band gap. Three groups of matter can be distinguished with respect to the band gap: Insulators (large band gap, very small

electrical conductivity), metals (band gap approximately zero and high conductivity) and semi-conductors.

The electronic wave functions for the various states in a band can be characterized by the wave vector \vec{k} , representing electron waves carrying momentum $\vec{p} = \hbar\vec{k}$ as in the free electron model. Crucial for the understanding of the electrical properties of carbon nanotubes is the fact that the band gap depends on the k-vector of the electronic states in the bands. By representing the band structure in a three-dimensional space spanned by k_x , k_y , k_z , which is the reciprocal space, it is possible that the band gap varies widely with the value of the k-vector components. The band structure is usually presented in the first Brillouin zone of the reciprocal lattice.

Materials for which the highest occupied valence band state (HOMO) has a different energy at the same point in k-space as the lowest unoccupied conduction state (LUMO) are termed direct-gap materials; those crystalline solids for which the minimum band gap occurs at a different k-value from the conduction-band minimum are called indirect-gap materials (see figure 3.5). The level which divides the filled and vacant levels (at zero Kelvin) is known as the Fermi level with energy E_F .

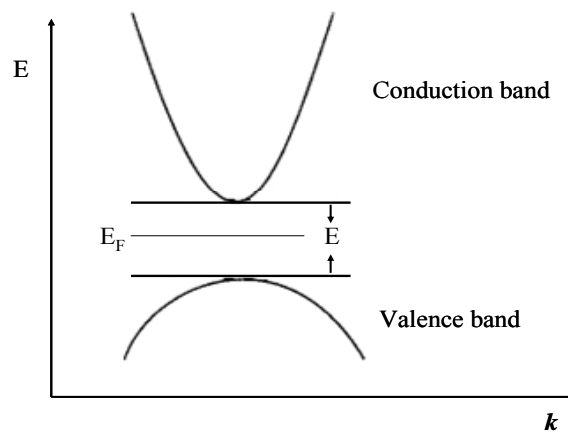


Figure (3.5): The band structure of a direct-gap material.

3.2.5 Lattice Structure of Graphene

As described before, a carbon nanotube can be considered as a seamless cylinder rolled up from a single graphite sheet. In general, the electronic properties of carbon nanotubes

are very sensitive to their geometrical structure, depending on the diameter and helicity of the nanotube. The electronic band structure varies dramatically with the chiral vector, even for tubes with similar diameter and direction of the chiral vector [8]. In order to understand the electronic properties of carbon nanotubes, we first have to understand the electronic property of a graphite sheet (graphene).

The chiral vector of the nanotube and the graphene geometry of the lattice determine the nanotube structural parameters like unit cell, diameter, the number of carbon atoms per unit cell and the size and shape of the *Brillouin zone*.

Figure (3.6 left) shows the hexagonal lattice of graphene in real space with the basis vectors $\vec{a}_1 = (\frac{\sqrt{3}a}{2}, \frac{a}{2})$ and $\vec{a}_2 = (\frac{\sqrt{3}a}{2}, -\frac{a}{2})$, where $a = \sqrt{3} a_{c-c}$ is the graphene lattice constant. Figure (3.6 right) shows the reciprocal lattice and its basis vectors $\vec{b}_1 = (2\pi/\sqrt{3}a, 2\pi/a)$ and $\vec{b}_2 = (2\pi/\sqrt{3}a, -2\pi/a)$. The graphene lattice structure is not a *Bravais lattice* by itself, but can be regarded as an underlying *Bravais lattice* with a two-atom basis (atom 1 and atom 2). The shaded hexagon in figure (3.6 right) shows the first *Brillouin zone* of graphene in the reciprocal lattice.

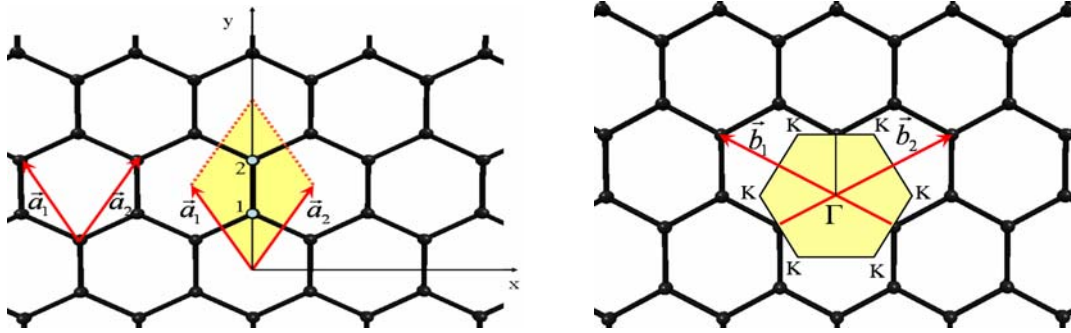


Figure (3.6): Hexagonal lattice of a graphite sheet in real space (left) and at right the corresponding reciprocal space; the first Brillouin zone has been indicated by the shaded hexagon.

3.2.6 Electronic Band Structure of Graphene

To explain the band structure of nanotubes it is logical to start with the band structure of graphene. The band structure can be derived from the tight binding approximation.

Carbon has four valence electrons per atom, three of which are used for the graphite-like structure to form sp^2 bonds with neighboring atoms in σ orbitals. The corresponding energy bands lie far below the Fermi level and do not contribute to the electrical conduction. The transport properties are determined by the remaining π electrons, which occupy the bonding and anti-bonding π and π^* bands resulting from the interaction between the $2p_z$ orbitals [9-14].

The tight binding approximation applied to the $2p_z$ orbitals of carbon in graphene yields the following relationship between the band energy E and the wave vector $\vec{k} = (k_x, k_y)$ for graphene [13, 15],

$$E(k_x, k_y) = \pm \gamma_0 \sqrt{1 + 4 \cos\left(\frac{\sqrt{3}a}{2} k_y\right) \cos\left(\frac{a}{2} k_x\right) + 4 \cos^2\left(\frac{a}{2} k_x\right)} \quad (3.12)$$

where $\gamma_0 \approx -2.5$ eV is the C-C interaction energy or the overlap integral between nearest neighbors [12-13] and $a = \sqrt{3} a_{c-c}$.

From equation (3.12) it can be seen that the valence and conduction bands have the same energy (touch each other at the Fermi level) at those values for k_x and k_y for which:

$$1 + 4 \cos\left(\frac{\sqrt{3}a}{2} k_y\right) \cos\left(\frac{a}{2} k_x\right) + 4 \cos^2\left(\frac{a}{2} k_x\right) = 0 \quad (3.13)$$

with the parallel condition that k_x and k_y lie on the edge of the first Brillouin zone.

The corresponding electronic band structure near the Fermi energy is shown in figures (3.7) and (3.8) [12], where it has been shown that equation (3.13) is fulfilled for six points indicated by K.

At these points, the bonding π bands and the anti-bonding π^* bands touch at the corners of the Brillouin zone and form 'cones' above and below the Fermi level (figure 3.8). For a two-dimensional structure as graphene the fact that the Fermi surface is one-dimensional but the allowed states at E_F are zero-dimensional results in a

vanishing density of states at the Fermi level. This means that although there is no gap at the points K the density of states at these points is zero and the material is still a semi-conductor - a gapless semiconductor [16].

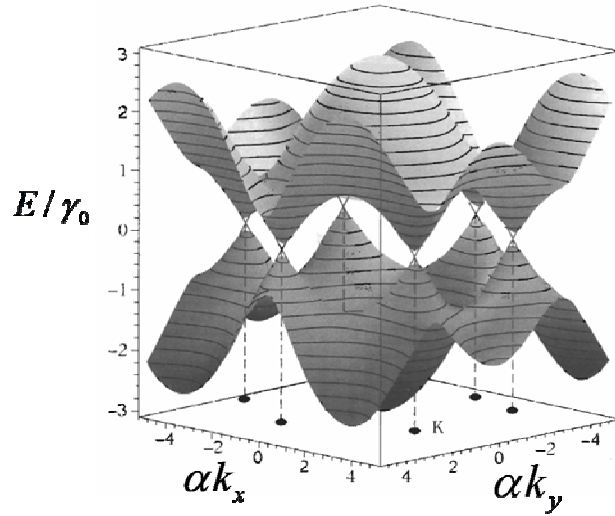


Figure (3.7): The complete electronic band of graphene. The bonding (π) bands and antibonding (π^*) bands touch at K and K' points, calculated by using the tight-binding approximation [modified from 12, 13].

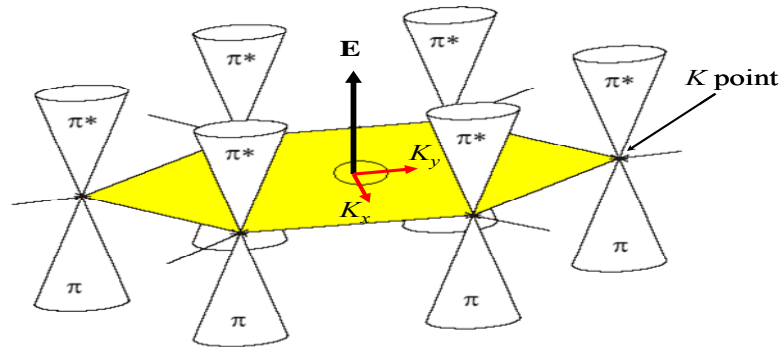


Figure (3.8): Three-dimensional plot of the graphene electron energy band structure near the Fermi energy E_F . The cones represent the low- and high-lying parts of the conduction and valence bands, touching at the K points of the Brillouin zone (modified from [16]).

Due to the bending of the graphene plane when a tube is constructed the electronic band structure of the graphene plane changes. It has been shown [17] that the electronic properties of carbon nanotubes can be either metallic or semi conductor depending on the

tube diameter or its chirality. If the index $n = m$, then the tube is armchair and always metallic. The tubes are metallic when $n=m$ or $n - m = 3i$, where i is an integer. In the other cases, when $n \neq 0$ or $n - m \neq 3i$, the tubes behave as semiconductors with an energy gap of the order of ~ 0.5 eV. It has been estimated that one third of all the nanotubes that result from all possible n and m values are metallic and the remaining two thirds are semiconductor (figure 3.11) [17].

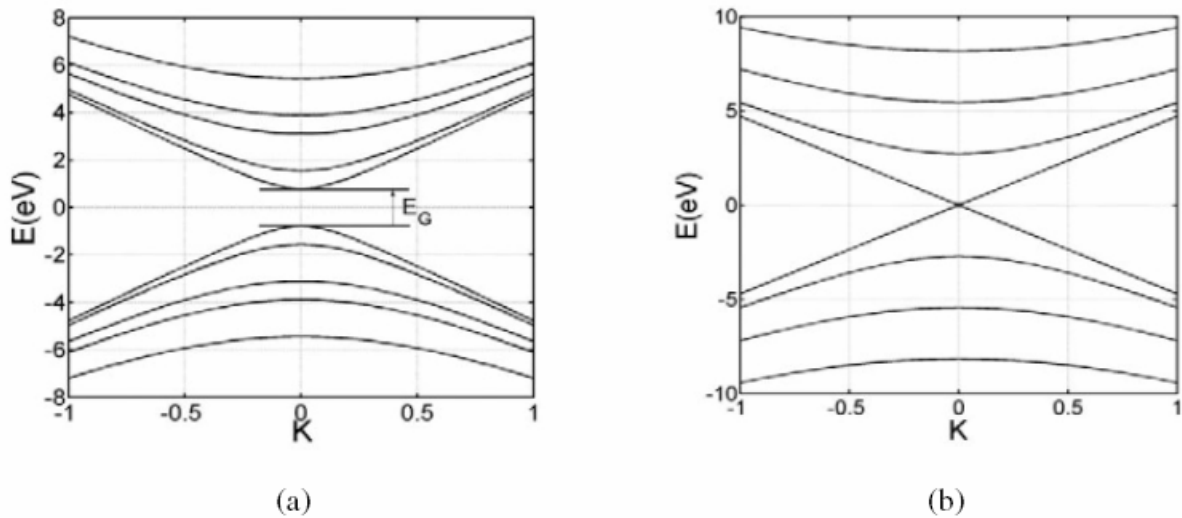


Figure (3.9): (a) *E-k* diagram of a semiconducting carbon nanotube (b) *E-k* diagram of a metallic carbon nanotube [15].

The direct experimental determination of d_{NT} and θ in real space by scanning Tunneling Microscopy leads to knowledge about the chirality of the nanotubes as shown in figure (3.10) and about the electronic properties as semi conducting or conducting.

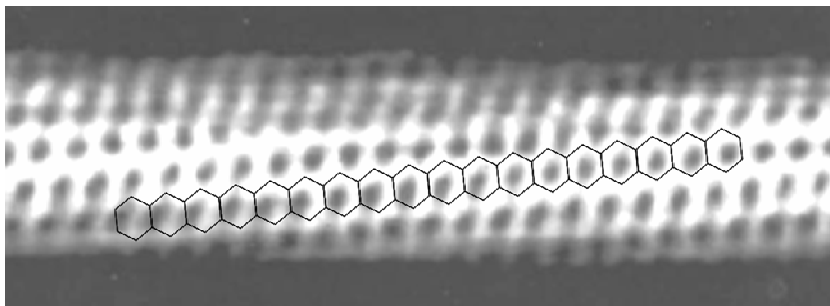


Figure (3.10): STM image of chiral nanotube (semiconductor) showing the hexagonal arrangement of the carbon atoms [12].

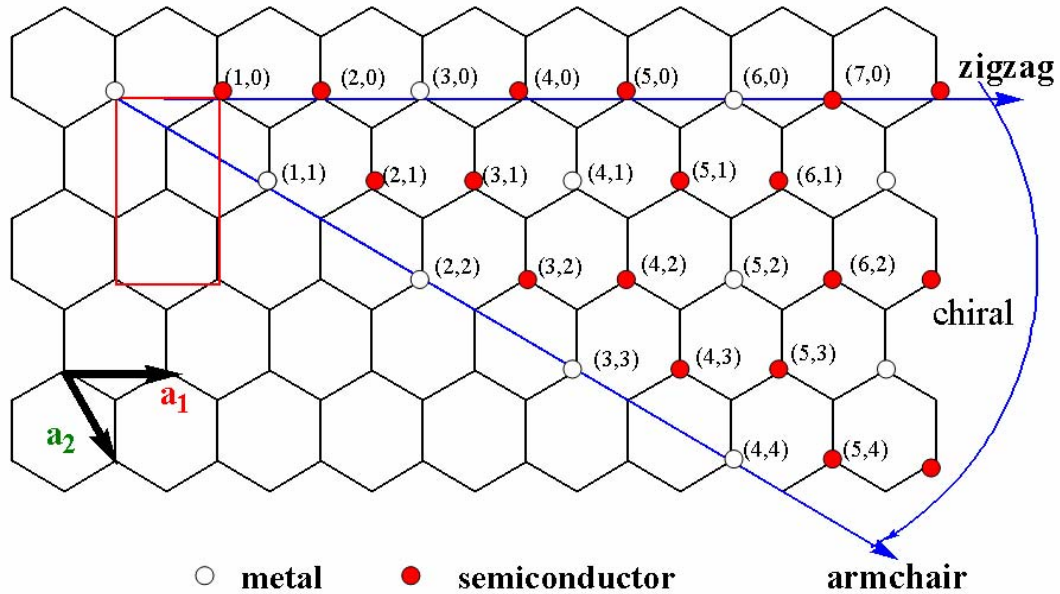


Figure (3.11): Metallic or semiconducting depends on which point the (0, 0) point is rolled to.

If the (0, 0) point is folded to any of the points along the armchair line, we get a metallic nanotube. However if it is folded along the zigzag line or in the chair area, which is the area between the zigzag and armchair, we get either semiconductor or metallic tube, depending on the n, m rules [18].

3.2.7 Hydrophobicity of Carbon Nanotubes

The behavior of liquids in capillaries and pores is an important aspect of the wetting of the surface. The capillarity of nanotubes is directly related to the surface energies of the liquid and the solid surface of the nanotube and therefore it is a problem of wetting behavior. In accordance with the equation of Young-Laplace, a pressure difference Δp across the liquid-vapor interface is related to the surface tension of the liquid γ and the contact angle θ between the liquid and solid: (4.14): [19]

$$\Delta p = 2\gamma \cos \theta / r \tag{3.14}$$

where r is the radius of curvature of the meniscus surface. The contact angle between the liquid and solid surface (see figure 3.12) is a direct indicator of the strength of the interaction between the liquid and the solid surface. If θ is larger than 90° , the contact is said to be non-wetting and Δp will be negative whatever the value of the other terms are in the equation. In other words, pressure will always have to be applied to force a liquid into a capillary if the contact is non-wetting. On the other hand, if θ is smaller than 90° , the liquid wets the tube and will spontaneously be sucked up inside the tube by a capillary force. If the liquid is water, then the surface is referred to the hydrophilic property. The wetting action derives from the fact that the surface tension and the contact angle are related by Young's equation which describes the vector summation of forces at the three-phase intersection point:

$$\gamma_{SV} = \gamma_{SL} + \gamma_{LV} \cos \theta \quad (3.15)$$

where γ_{sv} and γ_{sl} are the solid-vapor and solid-liquid interfacial tensions. Only when the solid-liquid interfacial tension is smaller than that of the solid-vapor will there be wetting $\theta < 90^\circ$. Good wetting is favored when the polarizability of the solid is higher than that of the liquid [19-21].

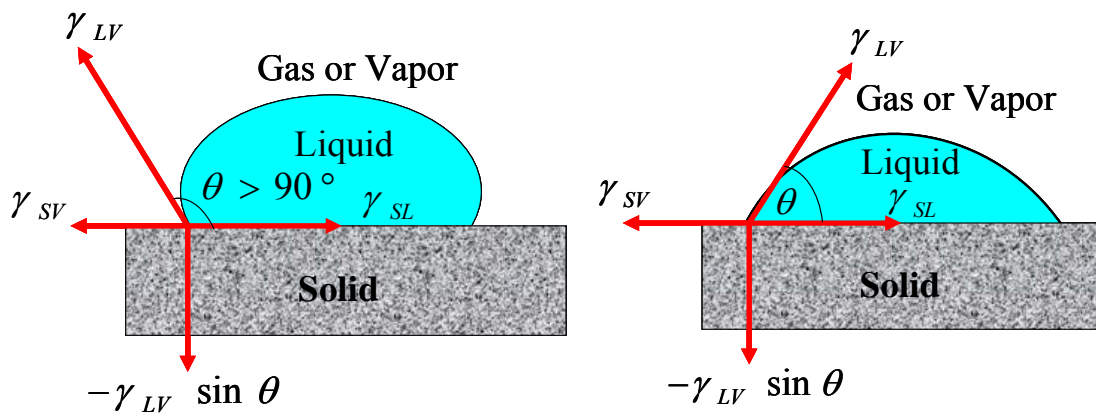


Figure (3.12): Vertical equilibrium for a drop of a liquid on a solid

A liquid will be drawn into a capillary tube only if it has a wetting contact angle with the surfaces. In our case of carbon nanotubes the cut-off surface tension is probably not sharply defined since the sample is composed of a distribution of nanotubes of various diameters and helicities having different electronic properties. Finally it was verified that what holds true for the wetting of the outside surface of the nanotubes also determines whether a liquid will be drawn into the hollow cavity of the tubes. The low surface tension liquids which wet the outside surface should fill open nanotubes by capillarity (i.e. Δp is positive). To achieve this, the nanotubes must preferably be empty from the beginning of the experiment. If nanotubes are filled with a gas such as air, it will oppose the entry of the liquid even if its surface tension is low. Liquids can still enter but the process will be much slower and the gas must have a route for escape such as being dissolved in the liquid. SWCNTs can be wetted by liquids have surface tension less than 200 mN/m therefore, water surface tension ~ 72 mN/m is expected to wet and enter the nanotubes. Many liquids can enter the nanotube, such as methanol ($\gamma = 22$ mN/m), ethanol ($\gamma = 22$ mN/m), bromines ($\gamma = 41$ mN/m) and water ($\gamma = 72$ mN/m) [22].

Ebbesen [23-24] studied the nano-capillary effect of carbon nanotubes by experiments of placing a water droplet on the surface (surface tension ~ 72 mN/m), the water was readily sucked up by capillary forces when it came in contact with the nanotubes channels. Also this is in agreement with the strong capillary effects for water discussed by Perdeson and Broughton [25].

Also in agreement, Ajayan and Iijima [25] showed that mercury and lead, which have a higher surface tension than water (> 400 mN/m), were not imbibed when they came in contact with a CNT.

3.3 References to Chapter Three

- [1] M. S. Dresselhaus, G. Dresselhaus, R. Saito, “*Physics in Carbon Nanotubes*”, M. Endo, S. Iijima, M. S. Dresselhaus, Pergamon, **1996**, 27.
- [2] D. Srivastava, M. Menon, K. Cho, “*Computing in Engineering and Sciences*”, an IEEE and APS publications, (July/Aug) **2001**, 42
- [3] T. W. Ebbesen, “*Carbon Nanotubes*”, CRC Press, Boca Raton, New York, **1997**.
- [4] M.S. Dresselhaus, G. Dresselhaus, P.C. Eklund, “*Science of Fullerenes and Carbon Nanotubes*”, Academic Press, **1996**, Ch. 29.
- [5] R. Saito, M. Fujita, M. S. Dresselhaus, G. Dresselhaus, *Appl. Phys. Lett.* **1992**, 60, 2240.
- [6] N. W. Ashcroft and N. D. Mermin, “*Solid State Physics*”, Holt, Rinhart and Winston **1976**.
- [7] S. Elliott, “*The Physics and Chemistry of Solids*”, Trinity College, Cambridge, UK and Univ. of Cambridge, UK, **1988**.
- [8] A. Charlier, E. Mcrae, M. F. Charlier, A. Spire, S. Forster, *Phys. Rev. B*, **1998**, 57, 6689.
- [9] A. Loiseau, P. Launois, P. Petit, S. Roche, J.-P. Salvetat, *Understanding Carbon Nanotubes: From Basics to Applications (Lecture Notes in Physics)*, Springer, **2006**.
- [10] C. Kittel, “*Introduction to solid state physics*”, John Wiley and Sons, Inc. New York, **1996**.
- [11] R. Saito, M. S. Dresselhaus, G. Dresselhaus, “*Physical Properties of Carbon Nanotubes*”, Imperial College Press, London, **1998**.
- [12] C. Dupas, Ph. Houdy, Marcel Lahmani, “*Nanoscience: Nanotechnologies and Nanophysics*”, Springer-Verlag. Berlin, **2007**.
- [13] G. Cuniberti, G. Fagas, K. Richter, “*Introducing Molecular Electronics (Lecture Notes in Physics)*”, Springer-Verlag. Berlin, **2007**.
- [14] S. Reich, C. Thomsen, J. Maultzsch, “*Carbon Nanotubes: Basic Concepts and Physical Properties*”, Wiley-VCH Verlag. Weinheim, **2004**.

- [15] S. K. Shukla, R. I. Bahar, “*Nano, Quantum and Molecular Computing, Implications to High Level Design and Validation*”, Kluwer academic Publishers, New York, **2004**
- [16] V. Derycke, J. Appenzeller, Carbon Nanotube Electronics in *Fundamentals of Nanoelectronics*, 34th IFF Spring School 2003 Institute of Solid State Research, **2003**.
- [17] A. Charlier, E. Mcrae, M. F. Charlier, A. Spire, S. Forster, *Phys. Rev. B*, **1998**, 57, 6689.
- [18] R. Saito, M. Fujita, G. Dresselhaus, M. S. Dresselhaus, *Appl. Phys. Lett.* **1992**, 60, 2204.
- [19] Thomas W. Ebbesen, *J. Phys. Chem Solids*, **1996**, 157, Nos 6-8. 951.
- [20] de Gennes, P. G., *Rev. Mod. Phys.* **1985**, 57, 827.
- [21] Tsang S. C., Chen Y. K., Harris P. J. F. and Green M. L. H., *Nature*, **1994**, 159, 372.
- [22] *Physics of Continuous Matter Exotic and Everyday*, by Benny Lautrup 2004, IOP. Institute of Physics Publishing, England **2004**
- [23] Dujardin E., Ebbesen T. W., Hiura H. and Tanigaki K., *Science*, **1994**, 265, 1850.
- [24] Ebbesen T. W. *Journal of Phys. Chem. Solids*, **1996**, 57 Nos 6-8, 950.
- [25] Pederson, M. R. & Broughton, J. Q., *Phys. Rev. Lett.* **1992**, 69, 2689.
- [26] Ajayan P. M. and Iijima S., *Nature* **1993**, 361, 333.

4

Chapter Four: Synthesis, Purification and Characterization of Carbon Nanotubes

4.1 *Synthesis of Carbon Nanotubes*

Soon after the discovery of carbon nanotubes, Ebbesen and Ajayan [1] successfully applied a large-scale synthesis which made extensive investigations on this promising material possible. Further optimization of the carbon nanotube growth technique raised the nanotube yields to above 70 %. Nevertheless, nanotube samples of higher purity are strongly needed for many research and application purposes.

There are four main methods to generate carbon nanotubes. Most of them are based on the sublimation of carbon under inert gas. The first method is chemical vapor deposition (CVD) [2], the second one is the catalytic decomposition of carbon monoxide in a high pressure process (HiPCO) [3], third method is the one called '*laser ablation*' (LA) [4] or the solar technique [5 -7] and the fourth method is arc-discharge (AD) [8]. The growth mechanism of nanotubes varies depending on which method is used.

The formation of SWCNTs always needs the presence of rare metals or a transition metal or mixture of them. The catalytic mechanism involves the coordination of metal atoms to the dangling bonds of growing nanotubes, called the scooter mechanism [9]. The transition metal atoms bridging two carbon atoms go scooting around the edge of the nanotube, as it is growing. The common mechanism of growing nanotube is the growth of an individual SWCNT on a metal nanoparticle substrate. The carbon atoms nucleate on the metal catalyst and grow to several micrometers in length, as is schematically illustrated in figure (4.1). When the carbon becomes super saturated in the nanoparticle, it starts to precipitate in form of graphitic sheets. Since the edges of the sheet are unstable, the emergence of pentagon defects leads to the formation of a nanotube cap which closes the tube. Closing the nanotube requires considerable distortion of the hexagon and hence of the sp^2 bonds [10] (figure 4.1; b; c; d and e). After the cap is formed, two processes

can happen: firstly, more carbon atoms can be inserted into the metal-carbon bonds, leading to the elongation of fullerene to form a single wall nanotube. Secondly, the fullerene cap can continue to grow around the nanoparticle, surround it and then preventing any further growth [11].

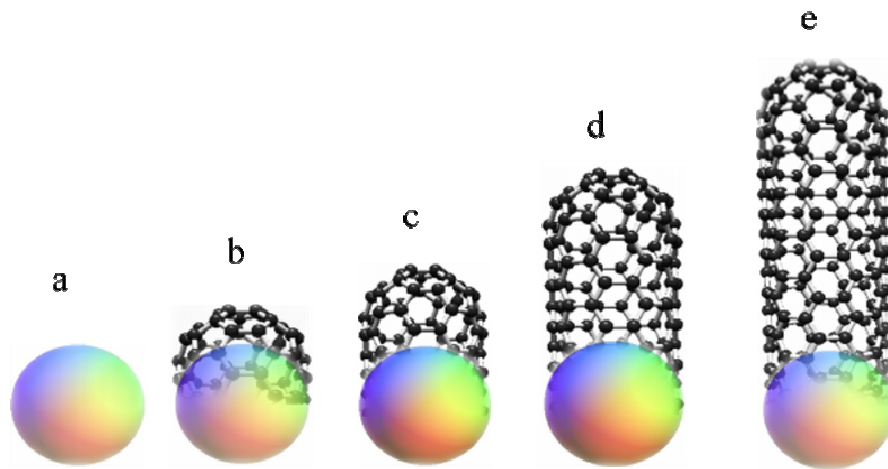


Figure (4.1): Root growth mechanism for formation of a SWCNT

4.1.1 Arc Discharge Technique [8, 12 - 22]

For our experiments, we have used SWCNTs prepared by arc-discharge and purchased from CNI, Houston Texas, USA (HiPCO).

The electric arc discharge process is one of the most common methods for nanotube production. This growth technique of carbon nanotubes has been greatly improved in time. This method was introduced for the synthesis of fullerenes. Iijima in 1991 has discovered MWCNTs by using this method, later he discovered SWCNTs by the same method and the metallic nanoparticles. The method is preferred over other methods in that it has high yields of high quality, low defect carbon nanotubes in large batches. It produces SWCNTs using a relatively low-priced and not complex apparatus.

The Krätschmer generator has been used to generate fullerenes. It consists of two carbon electrodes; the thicker cathode, on which the deposit is separated from the thinner anode by ~1 mm. This technique uses high temperatures (about 4000 K), which is needed to evaporate carbon into plasma. The arc discharge method produces both multi- and single walled carbon nanotubes.

As shown in figure (4.2) a graphitic rod is used as an anode in the reactor for nanotubes. In the rod a hole (3.2 mm diameter, 8.30 mm depth) is drilled, filled with a mix of carbon (65 % by weight) and metal catalyst powder (7% by weight Y and 28% by weight Ni). This rod is loaded into the reactor and acts as the consumed anode for the process. The cathode is a large plate made from high density carbon and is not consumed in the process (see figure 4.2).

The chamber is sealed and evacuated. It should be flushed several times with helium to expel all the air before being finally pressurized at 500 mbar for the run. A direct current (DC) source is connected to provide 100 amperes at a voltage of 60 volts. The arc is initiated by adjusting the distance between the anode and the cathode maintaining the voltage constant (60 V).

A bright discharge occurs and the anode is consumed. The nanotubes start to grow below 1100 °C. The electrode separation of about 1 mm must be maintained by the operator for the duration of the process which can take about six minutes until the electrode is consumed, and the process must be stopped. The chamber is cooled down by filling it with helium up to atmospheric pressure; and finally the reactor is opened slowly.

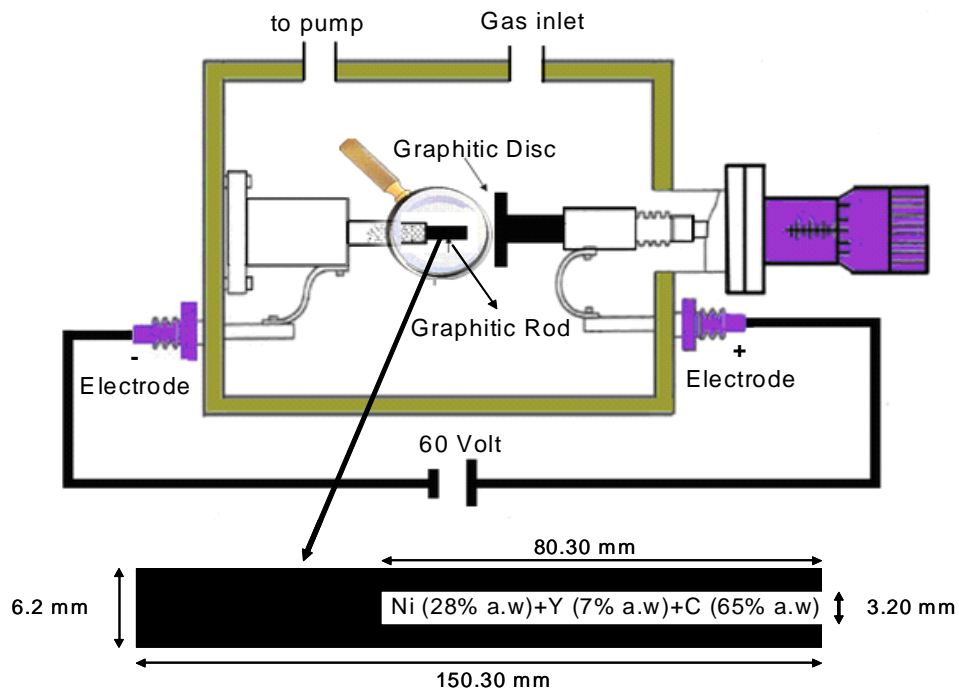


Figure (4.2): Scheme of the SWCNT Krätshmer generator which has been used to produce arc-discharge material and the rod filled with powdered NiY catalysts.

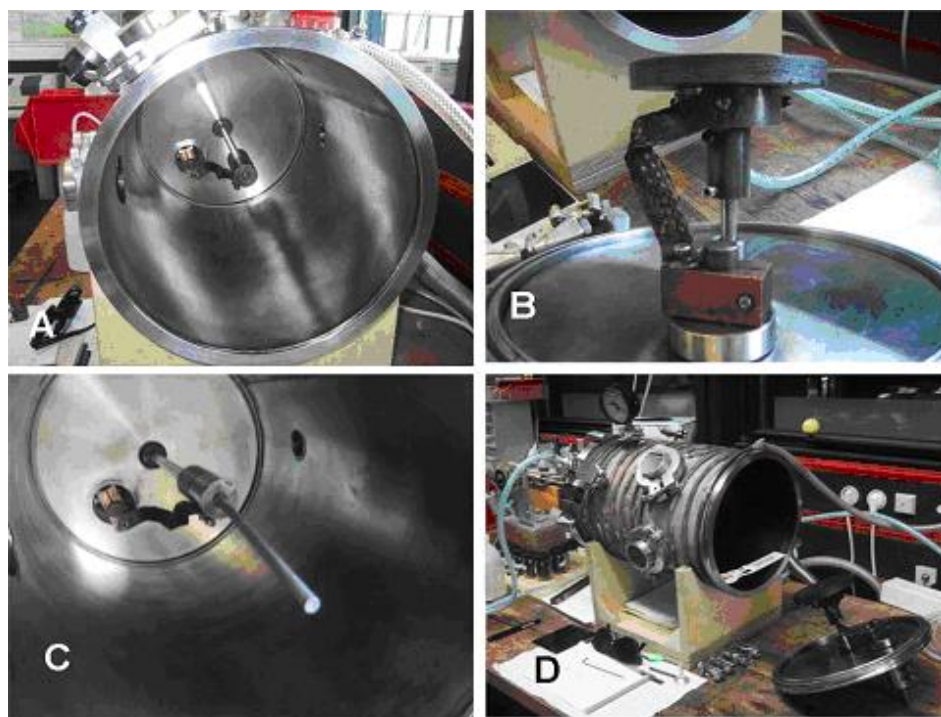


Figure (4.3): Arc-discharge reactor used for synthesis of SWCNTs. The photographs describe the SWCNT reactor; A) Chamber of the reactor, B) graphitic disc-cathode C) graphitic rod-anode

which is filled with catalysts, D) complete view of the reactor.

Table (4.1): Yield and appearance of different deposits in the arc-discharge reactor for nanotubes.

Area	Soot Appearance	Nanotube Yield
Cathode	Thick rubbery solid	High, bundled
Area behind cathode	Web aggregate	High, less bundled
Chamber walls	Powder	Medium
Collar around cathode (collaret) hard deposit	Low density black aggregate	Low
Cathode hard deposit	High density solid	Very low

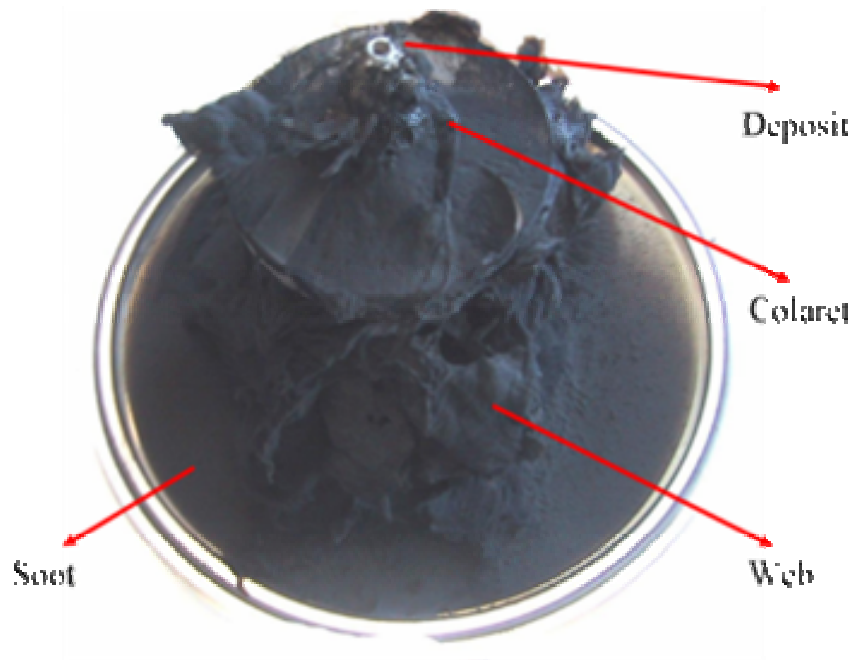


Figure (4.4): The appearance of SWCNTs in different deposits.

From figure (4.4) we can see that the overall carbon content is lowest for the cathode central hard deposit and highest for the outer cathode deposit. After finishing the process, we have to take a raw material (CNT) from the place with the highest and lowest concentration of nanotubes (as known from table 4.1). X-ray diffraction gives an

indication of the success of the production process.

Figure (4.5) shows the energy-dispersive X-ray microanalysis diagram (EDX) of heated SWCNT (350 C° 12 hours) versus the concentration of elements in the sample in counts per second (cps). It demonstrates the content of different elements in the sample (Ni = 4.55, Y = 2.43 weight % from the entire sample).

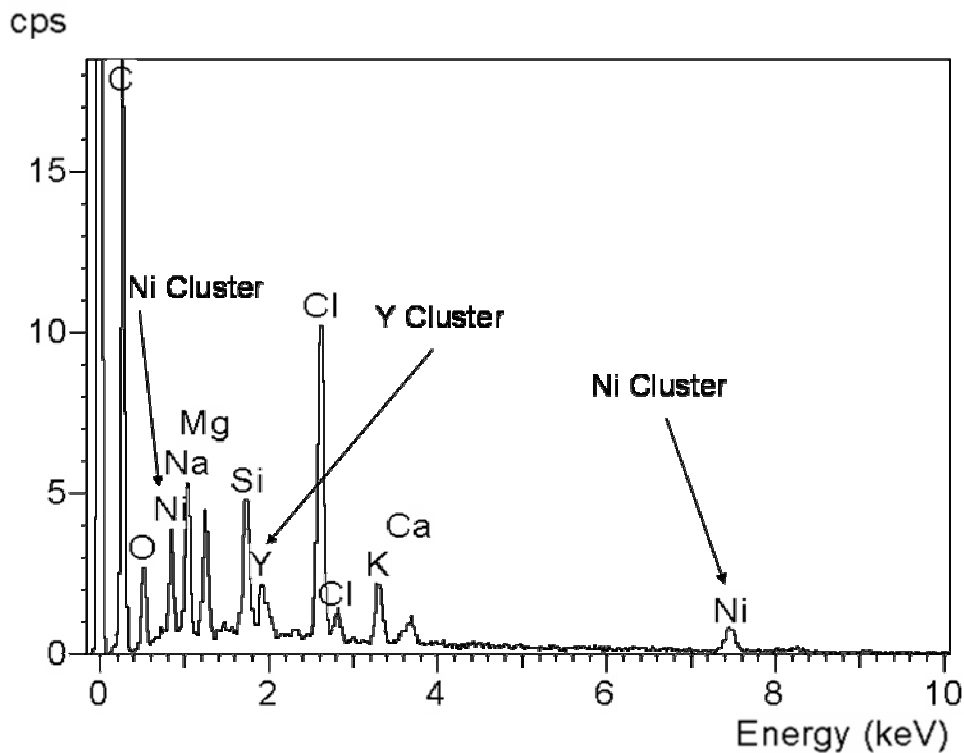


Figure (4.5): The energy-dispersive X-ray (EDX) diagram of cluster metals used in generation of Carbon nanotubes (NiY).

4.1.2 Laser Ablation

In the laser ablation process, intense laser pulses are used to vaporize a graphite target which is placed in an electrical furnace, as illustrated in figure (4.6), heated at 1200°C, and which is doped with small amounts of transition metal such as Fe, Co and Ni acting as catalyst for SWCNTs growth. The mixture is bombarded with laser pulses. This vaporizes the graphite, and the carbon vapor is swept away by the flowing of argon gas.

Upon cooling, the resulting black material meets a cold metal collector rod downstream in the oven.

Flowing argon gas (~500 mbar) sweeps the nanotubes from the high temperature zone to the water-cooled copper collector outside the furnace [23- 25]. If a pure graphite (without metal) target is used, MWCNT are produced [24]. Most of the individual single wall nanotubes that are generated in this method have diameters around 1-1.4 nm with a random distribution of chirality. They are produced in the form of ropes with tens of individual nanotubes closely packed via van der Waals interactions [26, 10].

The average nanotube diameter and the diameter distribution can be controlled by varying the synthesis temperature and the composition of the catalyst [27]. The diameters of the SWCNT have strongly peaked distributions.

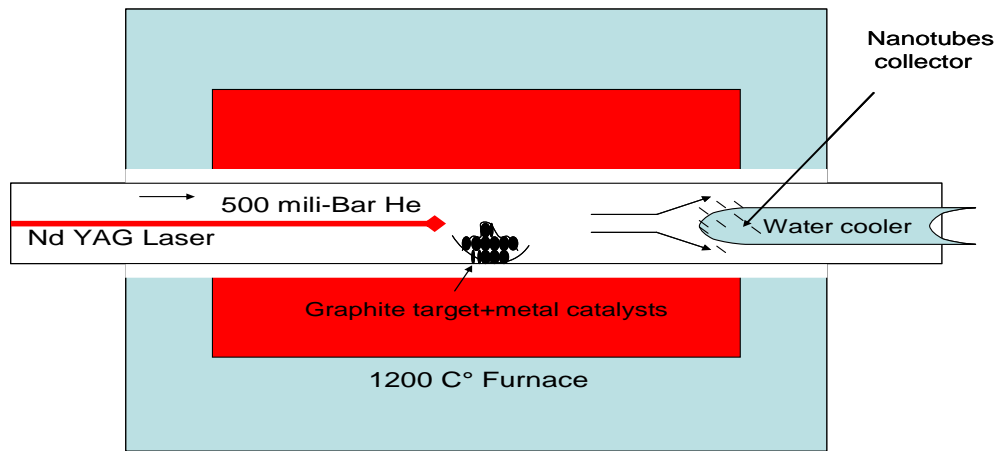


Figure (4.6): Illustration of a laser ablation apparatus.

4.1.3 Chemical Vapor Deposition (CVD)

The SWCNTs, which are generated by chemical vapor deposition (CVD) are not formed from solid graphite but from hydrocarbon gas by catalytic decomposition at a growth temperature between 500-1000 °C (figure 4.7). The most commonly used gaseous carbon sources include methane, carbon monoxide, and acetylene [28, 10].

Energy is imparted to the carbon species in the gas phase by using an energy source, such as plasma or a resistively heated coil. Gaseous carbon flows through the quartz tube where it is heated to a high temperature. The dissociation of the hydrocarbons breaks the hydrogen-carbon bond to produce pure carbon molecules. At high temperatures carbon nanotubes are formed. The metallic catalyst is usually re-deposited on a substrate (Al_2O_3 or SiO_2). Metal catalyst (Co, Fe or Ni) is sputtered onto the substrate by using either a chemical etching or thermal annealing to nucleate the catalyst particles [2, 28-34].

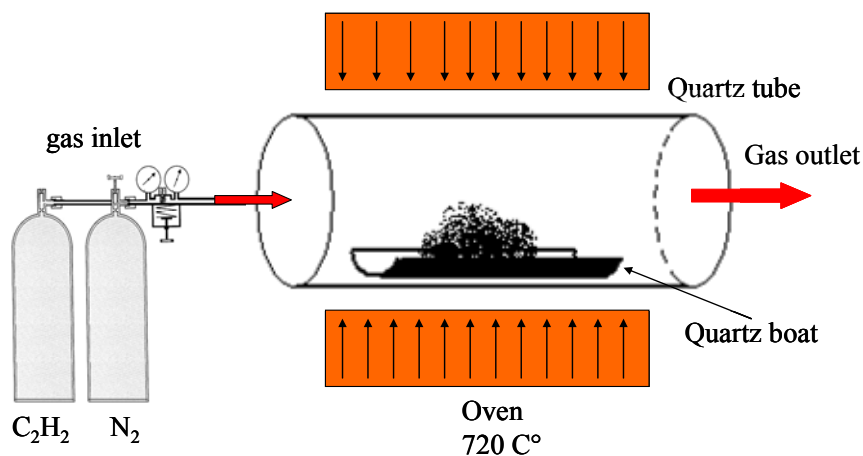


Figure (4.7): Basic schematic of the CVD apparatus used to grow nanotubes.

4.1.4 Decomposition of CO over Fe Catalyst

The high pressure catalytic decomposition of carbon monoxide CO (HiPCO) process is a technique for the high-scale production of high quality SWCNTs in a flow of gas by using CO as the carbon feedstock and $\text{Fe}(\text{CO})_5$ as an iron-containing catalyst precursor. HiPCO is a new gas-phase process for SWCNTs production discovered at Rice University in early 1998 as a special case of CVD synthesis [35]. The high-pressure (30-50 atm) decomposition of pentacarbonyl under a flow of carbon monoxide is an alternative method to the production of nanotubes for several reasons. It is a gas-phase process, which does not use pre-made catalyst particles, like other CVD methods. It is a continuous rather than a batch process, and the current HiPCO apparatus is able to run continuously for up to 2 weeks at a time, limited by the capacity of the nanotube collector. Nanotubes produced by HiPCO have a significant amount of Fe impurity, but

Fe nanoparticles are not encased in heavy graphitic shells as in arc or laser production but are relatively easy to remove [36, 28, 37, 10].

4.2 Purification

The purification of the carbon nanotubes is essential to our studies. As we will see later, especially the magnetic metal clusters hinder the NMR investigations. It is necessary to remove as many clusters as possible. Also, in order to study the water absorption by the SWCNTs, it is necessary to open the tubes, which are normally closed directly after the synthesis.

There are many purification techniques; each of them has its own advantages and limitations. Chemical oxidation treatments are conveniently used in large batch production, but they strongly destroy carbon nanotubes layers [15]. Non-destructive methods, such as micro-filtration or size exclusion chromatography purification methods are not practical for a large quantity of SWCNTs [12, 13, 15, 38-40].

The SWCNT samples that are used in this study were prepared by the HiPCO process in Houston and purified in Max-Planck-Institute for Solid State Research in Stuttgart, Germany.

To purify our samples we have used four purification treatments:

- a. Oxidation in air at 350°C to remove amorphous carbon;
- b. Sonication to fracture the metal clusters;
- c. Centrifugation to separate the metal clusters from the carbon nanotubes;
- d. Acidic treatment, also to remove the metal clusters.

4.2.1 Oxidation in Air

The different types of the batch are put in the oven in air by 350°C for three hours or until 25% weight loss. Most of the amorphous carbon will be removed by converting carbon into carbon oxides.

4.2.2 Sonication of Carbon Nanotubes

After the treatment in the oven the material is dispersed (1% weight) in a SDS solution (sodium dodecylsulfate) as a surfactant. The surfactant molecules are surface-active agents, which can modify the particle-suspending medium-interface and prevent the aggregation of particles for a long time. The dispersion is prepared with an ultrasonic probe (Finger ultrasonic generator Up 200S) with 50 Watt at full cycle for one minute. Too long sonication times should be avoided to prevent destruction of nanotubes. The ultrasonic treatment decomposes the metal nanoparticles.

4.2.3 Centrifugation

Centrifugation is another technique to purify carbon nanotubes. When a container with a suspension of carbon nanotubes is rotated at high speed in a centrifuge (Eppendorf centrifuge 5804), all suspended particles, including the dispersed nanotubes, will be accelerated towards the bottom of the container due to the centrifugal force. However, since different particles in the suspension may have different masses and may sense also different cohesive forces from the solvent, their acceleration is expected to be quite different. For instance, hard particles such as clusters of catalysts should move to the bottom faster than the long, thin carbon nanotube structures, which are subjected to larger cohesive forces and move along more complicated trajectories. Therefore, with appropriate control of the rotation speed and duration, one may expect that the final suspension will contain more carbon nanotubes than the original suspension. The purity of carbon nanotubes in this way is improved. The procedure is repeated three times with increasing speed and running time (3600 rpm for 1-2 minutes, 5000 rpm for 3 minutes and 15000 rpm for 3 minutes. After each run the precipitate is removed from the container).

4.2.4 Acidic Treatments of SWCNTs

An oxidation procedure is used to remove from the sample the metal impurities and other graphitized carbon structures. The carbon tube structures, in which the metal clusters are encapsulated, have to be opened. Most purification methods employ acid treatment to dissolve the metal particles, whereas air oxidation is applied to remove the amorphous carbon. [12, 13, 39-41]. For the oxidation process, agents such as HNO₃ and H₂SO₄ [41-

42] are used. The chemical oxidation methods are easily used in large batch production, but they strongly destroy carbon nanotubes layers and are inapplicable to SWCNTs [15].

In my work an efficient purification procedure which combines centrifugation and precipitation has been used. The process includes three main steps: First, the raw soot is treated in 65 % nitric acid for three hours. During this time a weight loss of about 20% occurs. After the black solution is centrifuged, black sediment remains at the bottom of the centrifuge tube. The clear brownish-yellow supernatant acid is decanted off. The sediment still contains substantial amounts of trapped acid, which is removed by repeated re-suspension of the sediment in distilled water. Thereafter the supernatant liquid has to be centrifuged and decanted. After these successive washing-centrifugation cycles, the liquid phase becomes less acidic. The remaining solution, suspended with the remaining components, is left behind after the mixture is centrifuged (supernatant) and becomes first colorless and then increasingly dark. The remaining sediment is dispersed in de-ionized water by treating it with ultrasonic pulses for one minute. After finishing the acidic treatment, high temperature (350°C for one hour) is used to remove the chemical functional groups, created on the nanotube surface by the acid treatment [42-44]. Otherwise the chemical functional groups which have protons would disturb the water NMR spectra.

4.3 Characterization

4.3.1 Electron Microscopy

By using transmission electron microscopy (TEM) or scanning electron microscope (SEM), it is possible to see that the carbon nanotubes are cylinders of graphene sheet with different structural symmetry. Scanning electron microscopy (SEM) was conducted on a LEO 1530 VP field emission scanning electron microscope equipped with a Phoenix EDX system. Transmission electron microscopy (TEM) analysis was carried out on a Philips CM 200 electron microscope (point resolution of 0.2 nm and acceleration voltage of 120 kV (in MPI Stuttgart)).

4.3.1.1 Microscopy of SWCNTs

Figure (4.8) shows a scanning electron microscopy (SEM) image of a raw material containing bundles of nanotubes, amorphous carbon and clusters of NiY. Figure (4.9) shows at a higher resolution an electron microscopy picture of a sample with 20 wt % Fe clusters. Here nicely the carbon nanotube bundles and the metal clusters can be observed. Figures (4.10)-(4.18) show SWCNT material at different purification steps. The purification causes a decrease in bundle size and shortens the tube length.

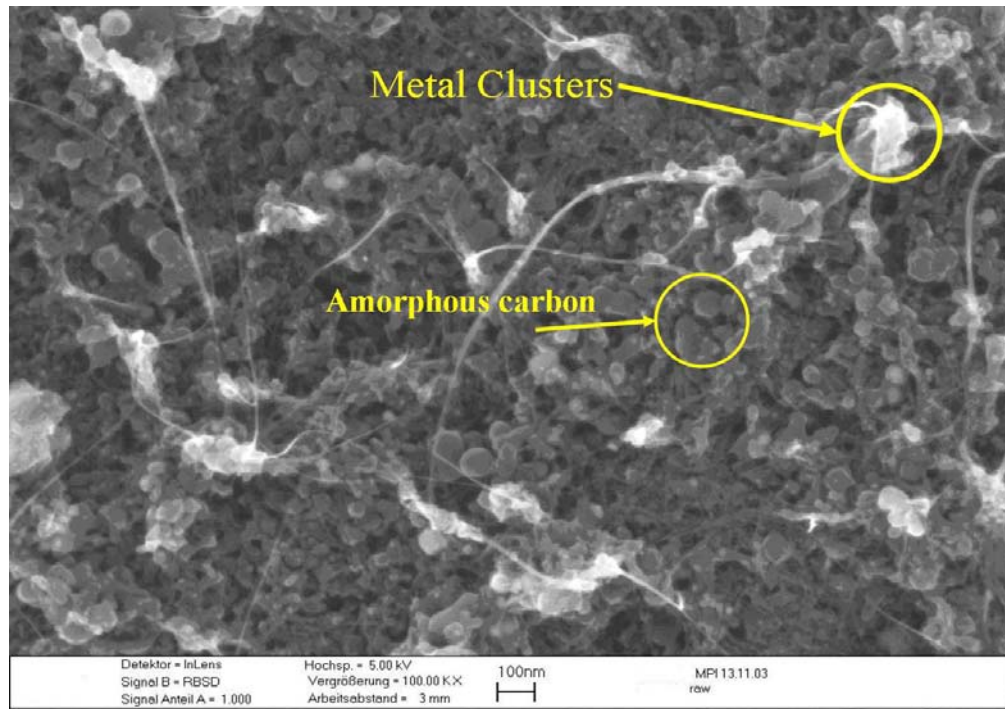


Figure (4.8): SEM micrograph of raw SWCNT (NiY).

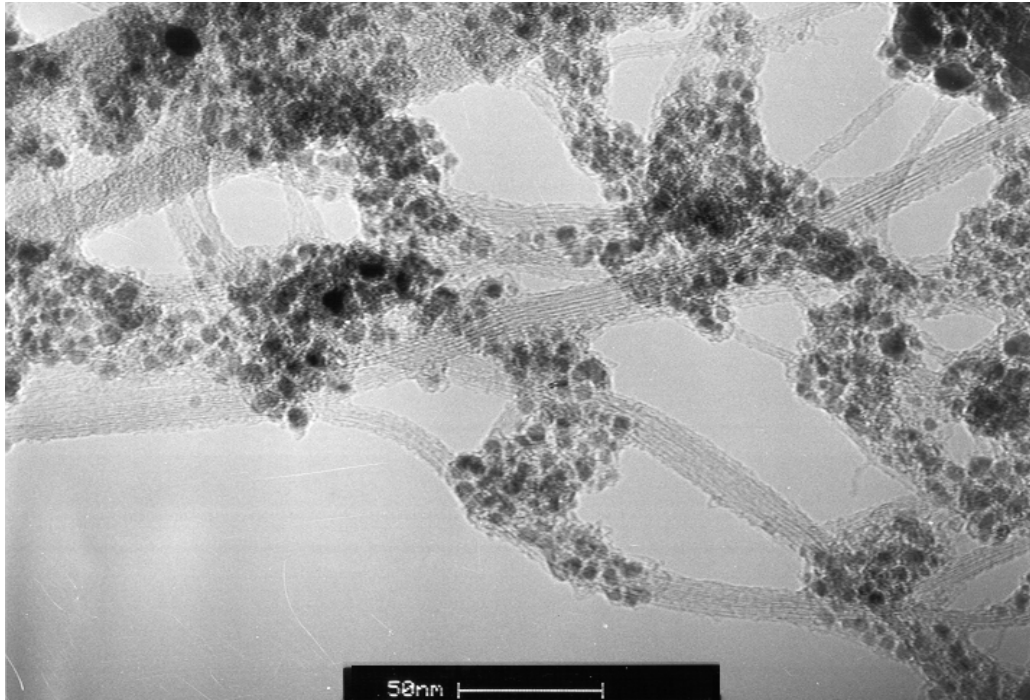


Figure (4.9): TEM picture of a raw SWCNT (Fe HiPCO) with 20% wt Fe impurity.

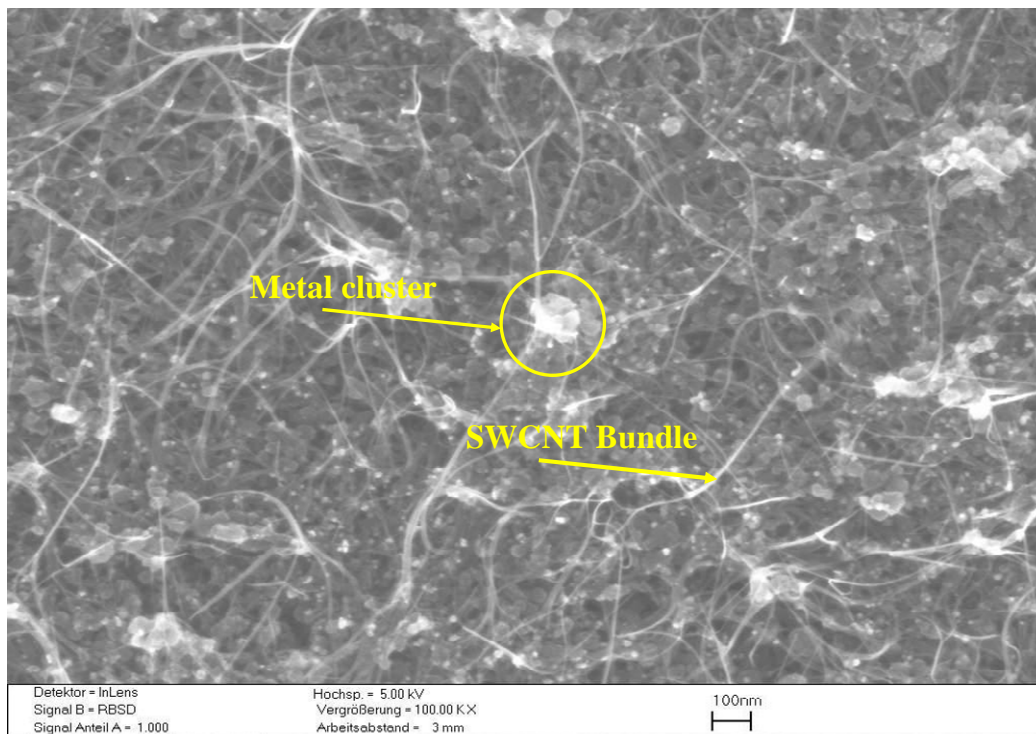


Figure (4.10): SEM picture of the samples with 13wt % NiY impurity (raw sample).

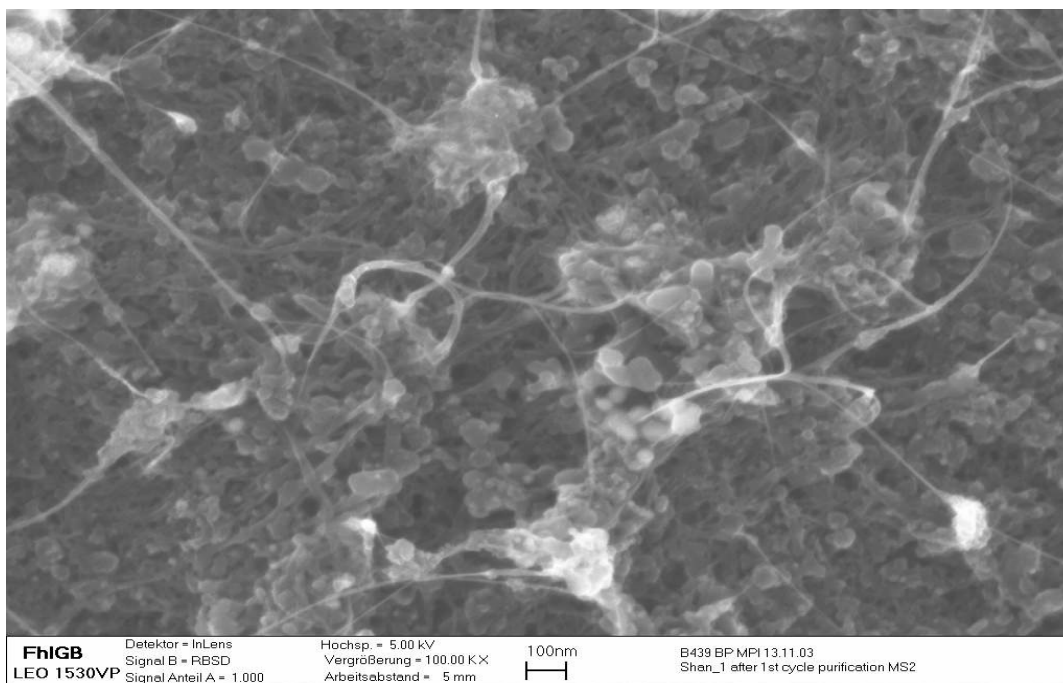


Figure (4.11): SEM micrograph of SWCNT (NiY) after first cycle of purification.

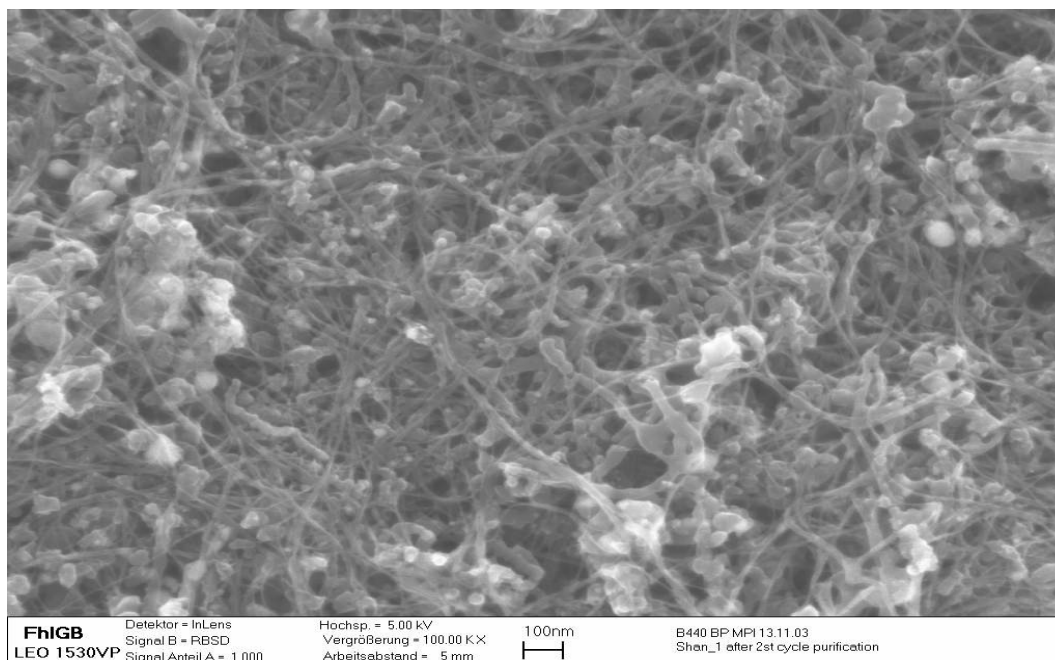


Figure (4.12): SEM micrograph of SWCNT (NiY) after second cycle of purification.

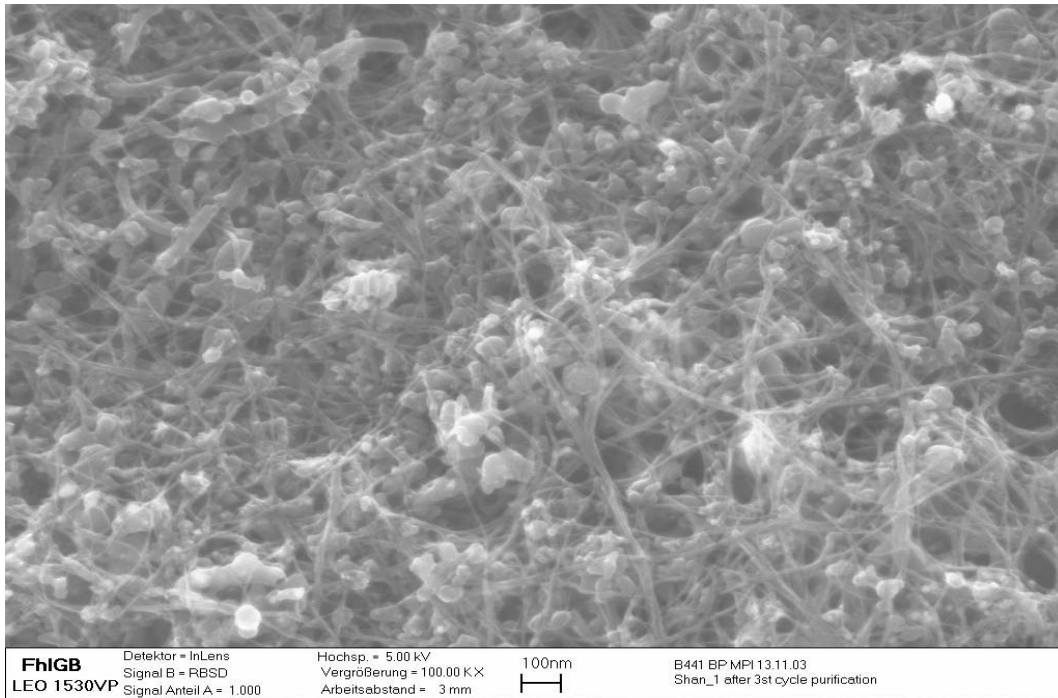


Figure (4.13): SEM micrograph of SWCNTs (NiY) after the third cycle of purification.

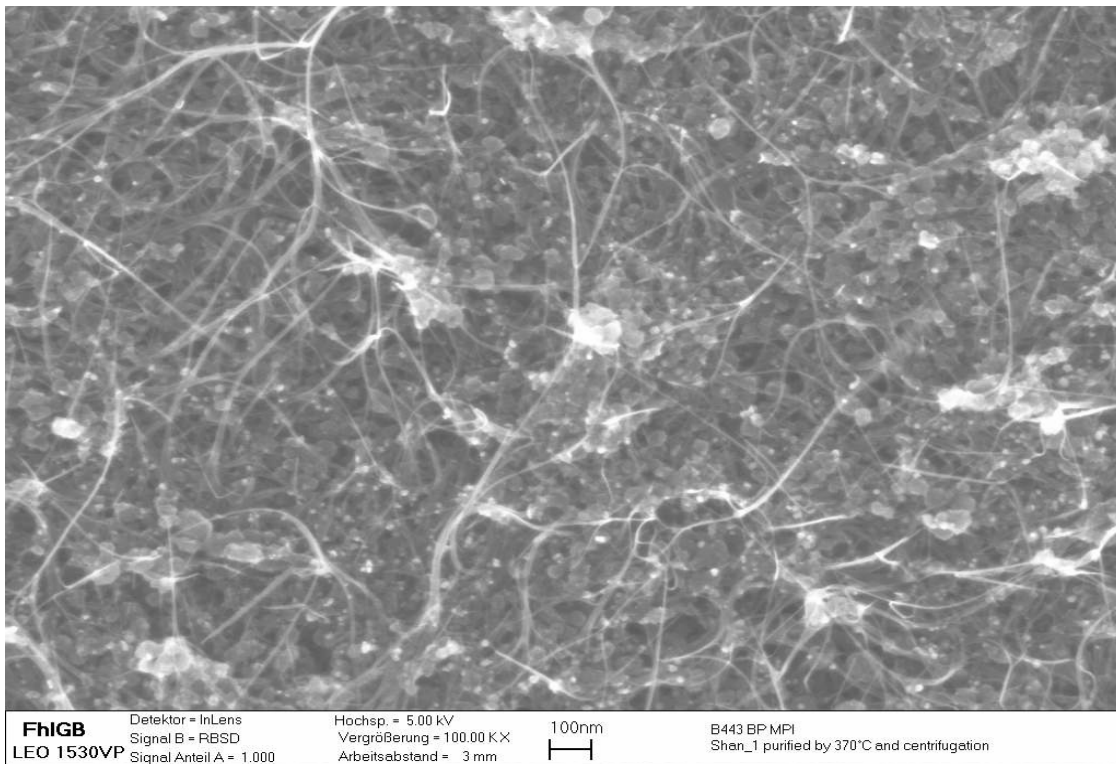


Figure (4.14): SEM micrograph of SWCNTs (NiY) after heat treatment at 370 °C and centrifugation without any cycle of purification

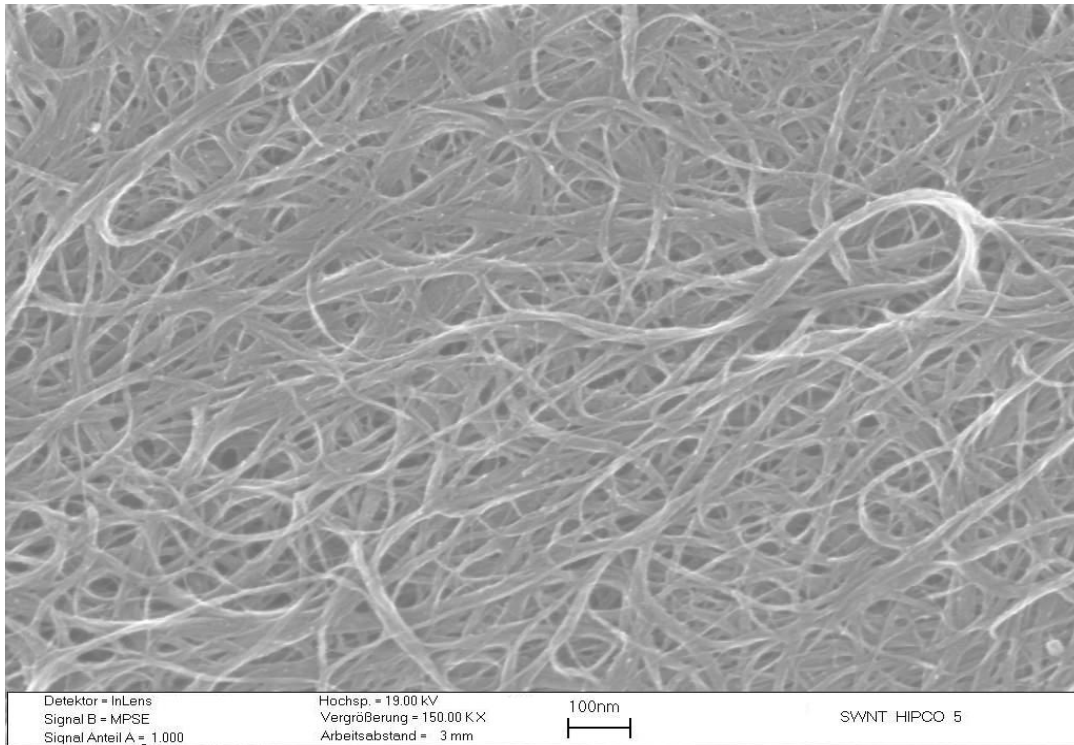


Figure (4.15): SEM micrograph of SWCNTs (Fe pure) after treatment at 370 °C and centrifugation without acidic treatment

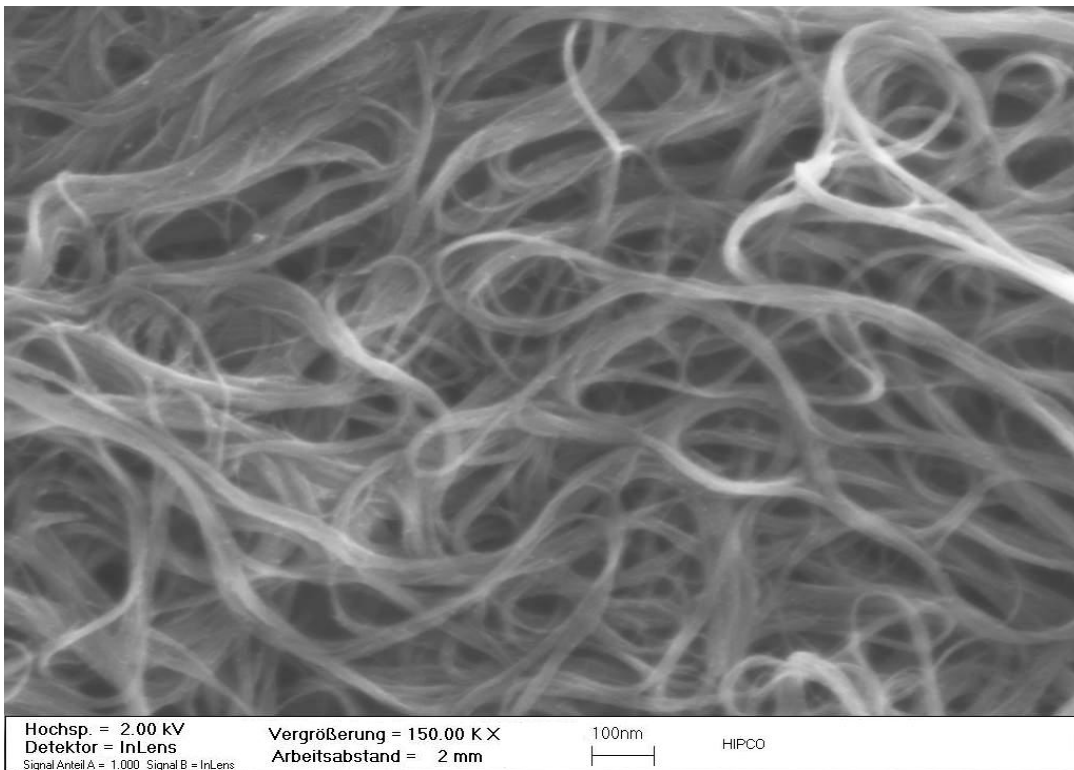


Figure (4.16): SEM micrograph of SWCNTs (Fe pure) after treatment at 370 °C and centrifugation without acidic treatment

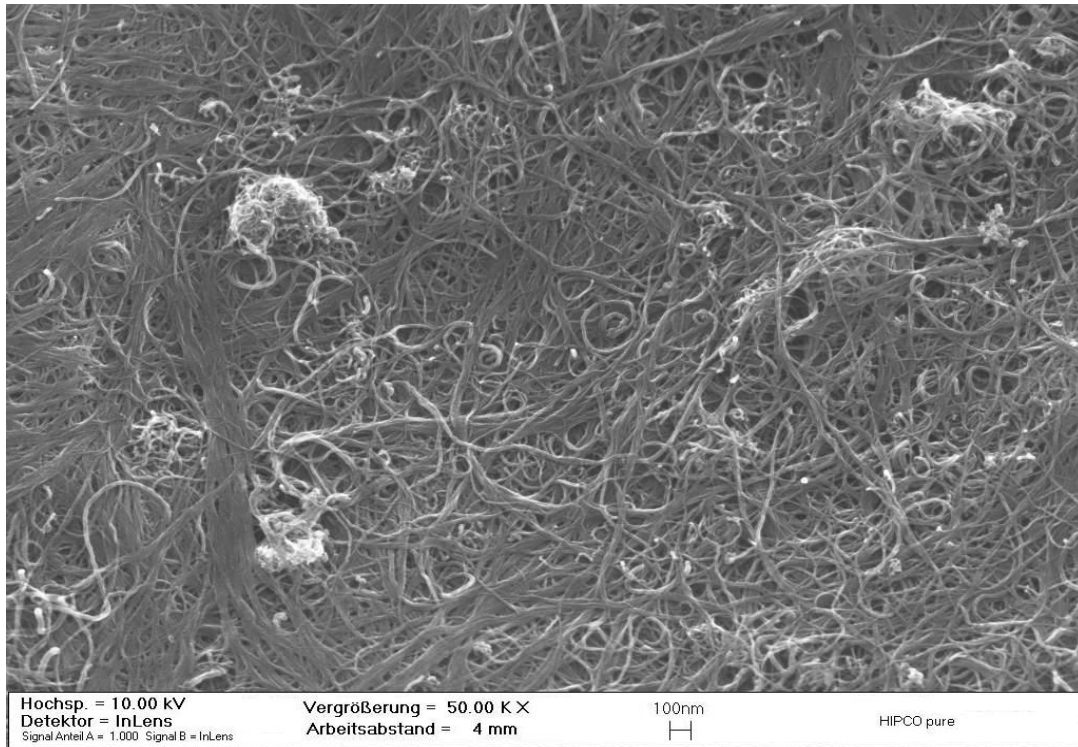


Figure (4.17): SEM micrograph of SWCNTs (Fe pure) after treatment at 370 °C centrifugation

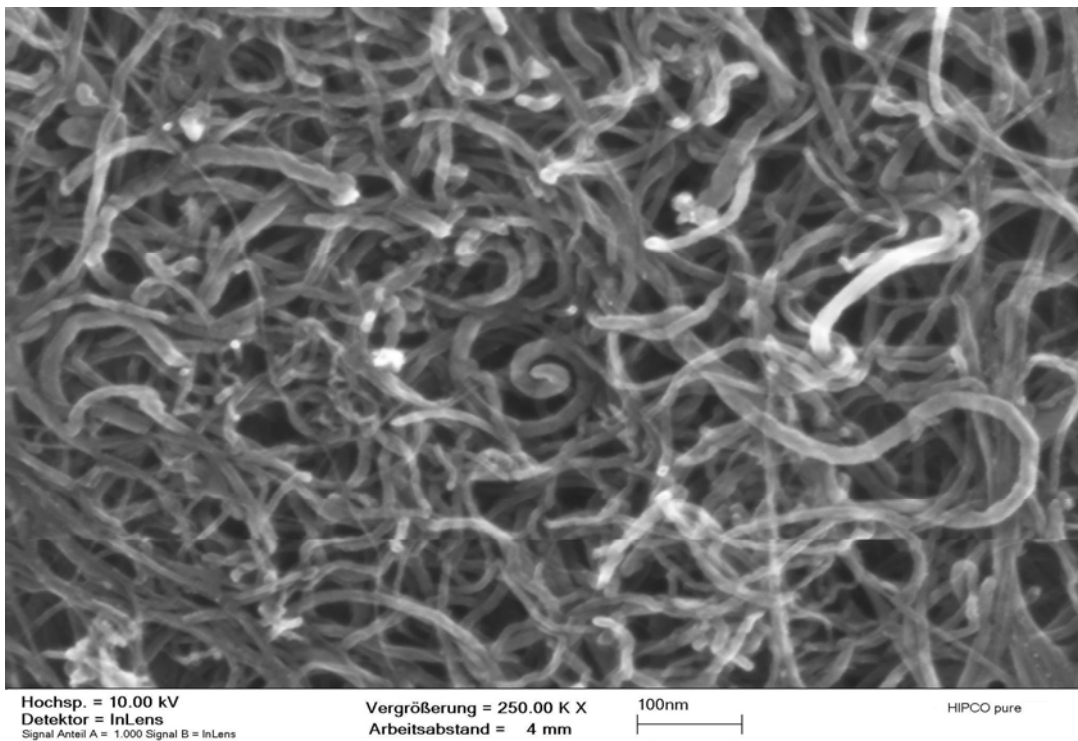


Figure (4.18): SEM micrograph of SWCNTs (Fe pure) after treatment at 370 °C centrifugation and many acidic treatments to make the tube shorter.

4.3.2 Differential Scanning Calorimetry (DSC) [45]

Differential Scanning Calorimetry (DSC) is a widely used thermal analysis technique to provide qualitative and quantitative information about physical and chemical changes that involve endothermic or exothermic processes and changes in heat capacity using minimal amounts of a sample. DSC is capable of isolating the temperature dependent thermal events for a given chemical process; it also allows a quantitative measurement of the heat associated with the process. A DSC calorimeter has two pans as shown in figure (4.19). In the left pan, the sample pan, we put the sample. The other one is the reference pan. We leave it empty. Each pan sits on top of a heater.

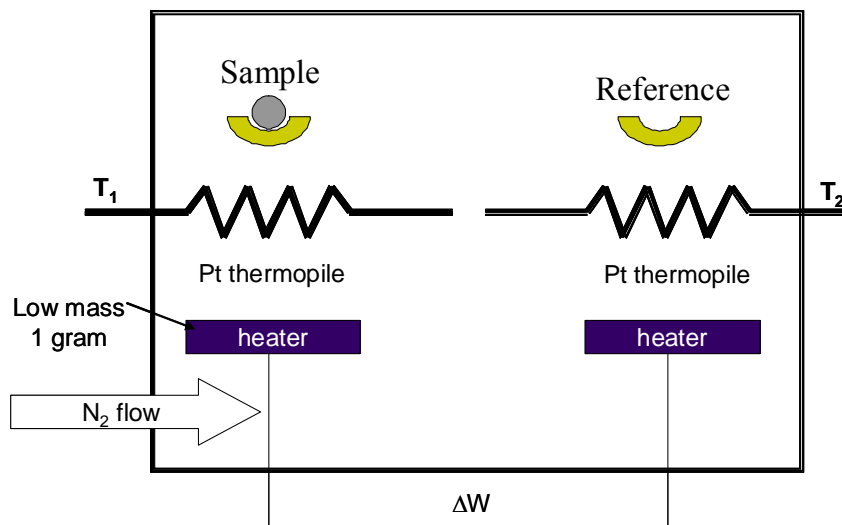


Figure (4.19): Scheme of DSC Instrument.

In the particular case of carbon nanotubes, the weight change in air atmosphere is typically a superposition of the weight loss of water from outside and inside of the tubes. DSC measurements have been recorded by using the DSC (204) Phoenix thermal analyzer (NETZSCH GmbH) in dry nitrogen atmosphere with a temperature scanning rate of 5 °C/minute. DSC is used to characterize the behavior of water and the thermal properties of opened SWCNT as reported in chapter four.

4.3.2.1 Differential Scanning Calorimetry of SWCNTs

The thermal behavior and stability of the SWCNT-water system have been investigated by Differential Scanning Calorimetry (DSC).

Figure (4.20) shows the DSC curve for opened SWCNTs loaded with 100 wt % of water. The first peak appears at 103.6°C and the second at 132.1 °C. All water is gone at a temperature below 160°C. This result is very important for the NMR measurements, because it shows that we can empty the tubes completely from water by heating the sample at 160°C for 20 minutes which is the time it takes to run the curve in figure (4.20).

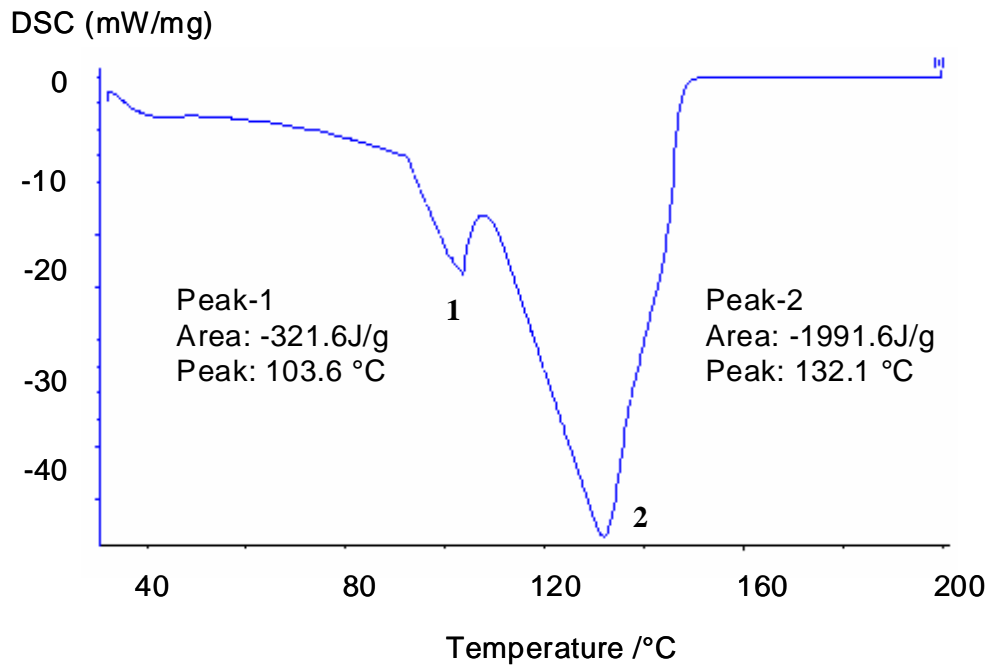


Figure (4.20): The thermal behavior of opened SWCNT (Fe pure).

The first peak, close to the normal boiling temperature of water, represents only 6.7 % of the total area, whereas the second one represents 93.3%. This means that the greatest part of the water is not bulk water but behaves as bound water that is removed at 132.1°C.

The results of the thermal analysis indicate that SWCNT material has two types of absorbed water, possibly bulk water outside and bound water inside the tubes.

4.3.3 Thermogravimetry (TGA) [45]

Thermogravimetry is a technique for measuring the change in weight of a substance as a function of temperature or time. The sample is usually heated at a constant rate and has a constant weight until it begins to decompose at a certain temperature. The difference in the weight and the slope of the decomposition steps are characteristic for the decomposition process and can be used for quantitative calculations of compositional changes. Approximately 20 mg samples were placed in a platinum crucible on the pan of balance. The sample heated from 20 to 900 °C at heating rate of 5 °C/min while being purged with N₂ at rate flow rate of 100 ml/min. TGA is also used effectively to be sure that the SWCNT are opened.

4.3.3.1 Thermogravimetric Analysis of SWCNTs

In this section three TGA curves are shown. Figure (4.21) shows the TGA curve of the raw SWCNTs. The raw soot includes closed SWCNT, amorphous carbon, and metal clusters. There are three stepwise weight loss peaks starting at 363.12 °C, at 431.52 °C, and at 472.82 °C. A considerable weight loss starts at 363.12°C due to oxidation of the Fe metals.

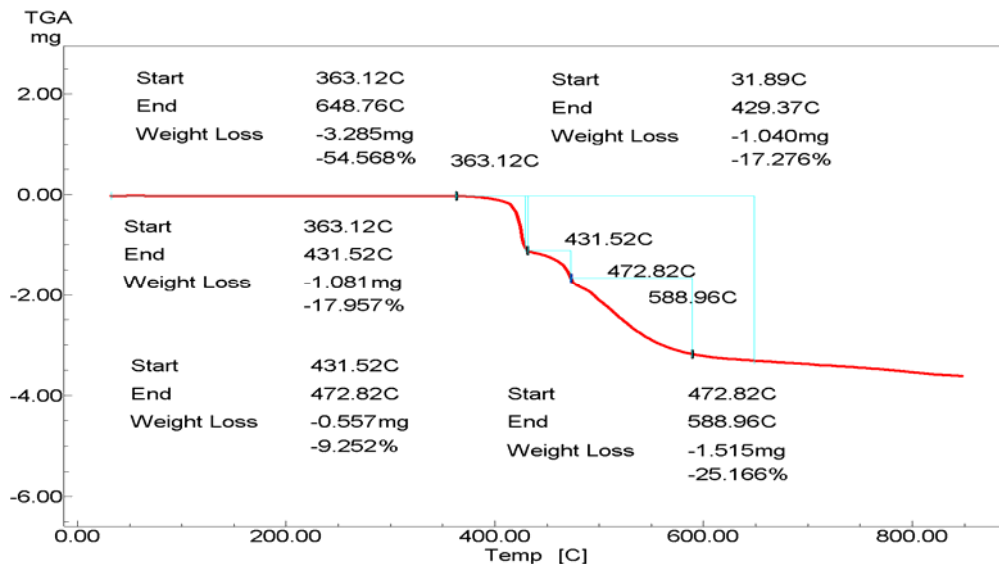


Figure (4.21): The thermogravimetric analysis of raw SWCNTs (Fe) by using nitrogen gas as a sample bath.

The corresponding weight loss of 17.9 % is explained by the loss of molecules (CO_2 , H_2O , NH_3) [46] existing inside the carbon nanotube often opening one side or both sides of the tube. This opening can be explained by comparing the strength of the chemical bonds in the carbon nanotube. The bond strength of hexagons is stronger than the bonds in a heptagon. Therefore, the body of the nanotube structure which contains only hexagons, resists the heating longer than the caps, which consist of heptagons and hexagons. Thus the cap will be opened to release the trapped molecules causing the large weight loss.

The second peak (weight loss 9.252%) and third peak (weight loss 25.166%) probably occur as a result of the loss of carbon species such as amorphous carbon.

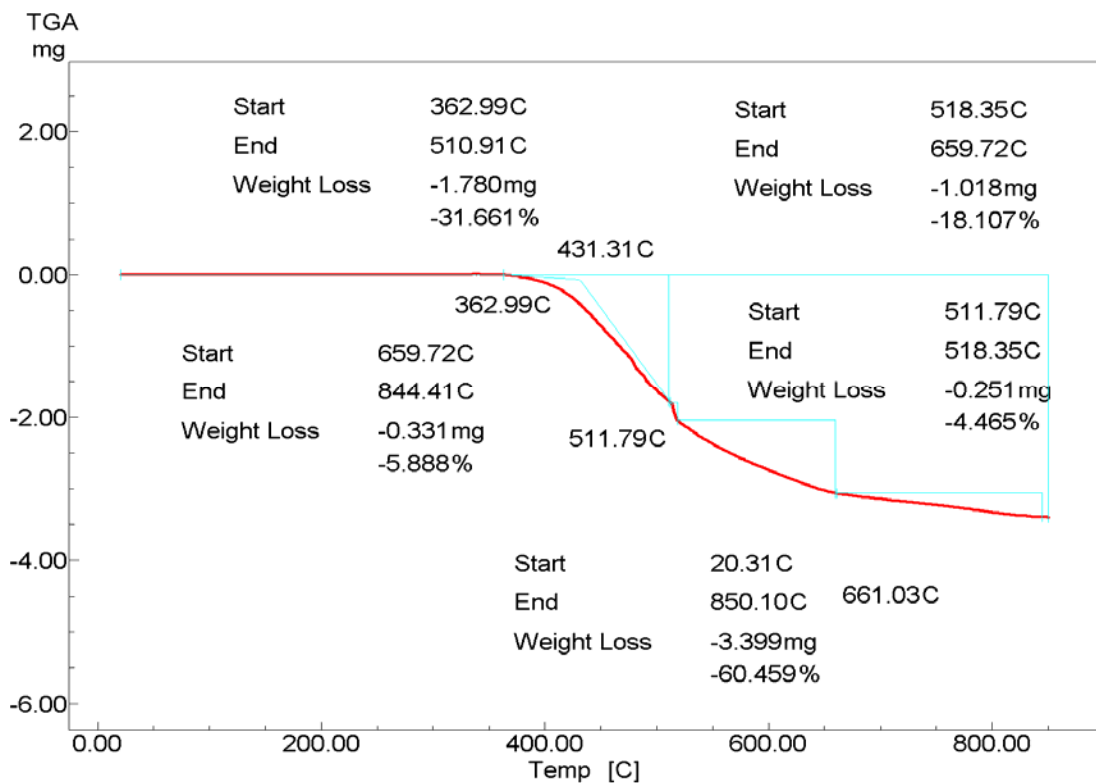


Figure (4.22): The thermogravimetric analysis of SWCNTs (Fe) oxidized at 350 C° determined in H_2 flowing gas.

In the case of oxidized SWNT material (figure 4.22) there are three stepwise weight loss peaks at 362.99 °C, 511.79 °C and 518.35°C. The first weight loss with 31.66 %, which

can be attributed to loss of amorphous carbon by the oxidation process. The second weight loss with 5.89 % and the third with 4.46 % probably refer to the loss of the rest of the encapsulating parts or of other types of amorphous carbon inside the nanotube.

For the purified HiPCO SWNT the sample starts to lose weight at 424.77°C, as shown in figure (4.23).

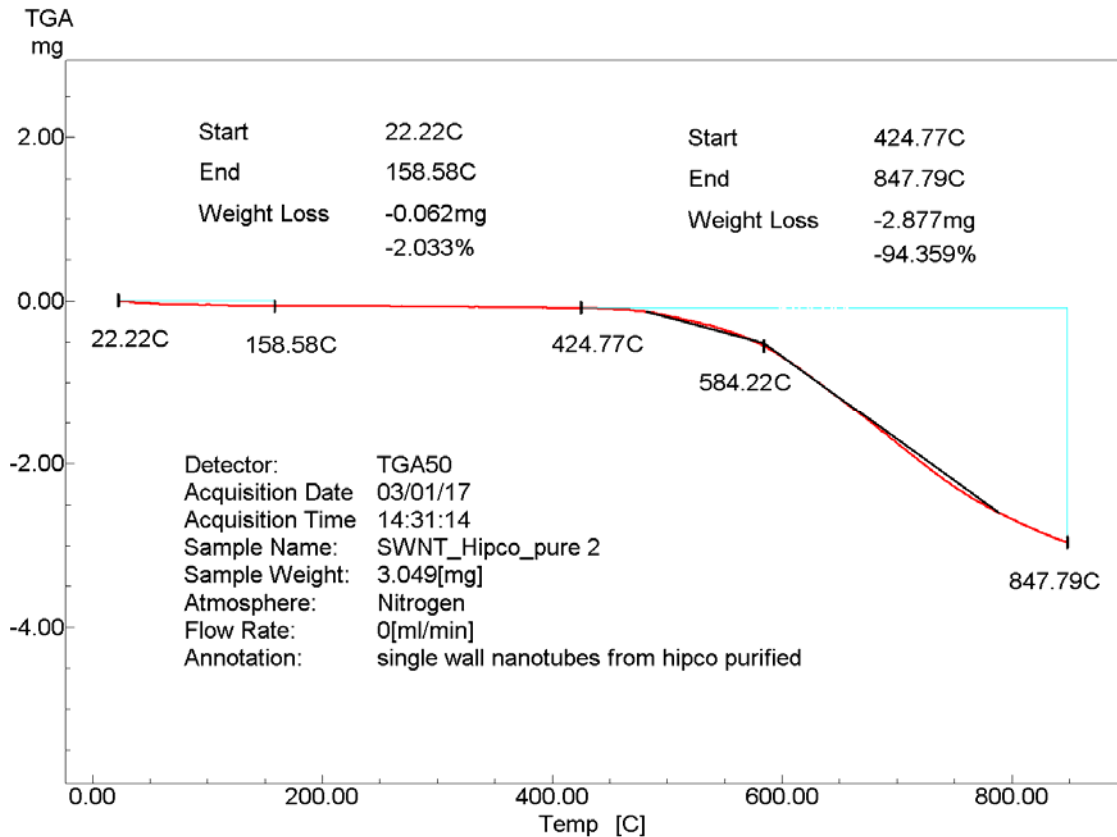


Figure (4.23): The thermogravimetric analysis of pure open HiPCO SWCNTs (Fe) under bath of nitrogen gas.

In comparison to previous experiments the burning of SWCNT begins very slowly at a higher temperature, higher than 400°C, whereas the amorphous carbon has begun to remove effectively at about 350°C. Therefore, 365°C is an appropriate temperature to burn out amorphous carbon. There are no sharp steps because the purified nanotubes are free from amorphous carbon and entrapped molecules.

4.3.4 Raman Spectroscopy

When a molecule is excited by a photon, it usually emits another photon of the same energy and relaxes to its previous state. This process is called Rayleigh scattering. The scattering can be considered as elastic because the emitted photon is equal in energy to the exciting photon, in a similar way to Compton's scattering of x-rays. Also inelastic scattering of light can occur, when the emitted photon has a lower or higher energy than the Rayleigh photon. This is called Raman scattering. The lower energy photons are observed as Stokes lines, whereas the higher energy photons lead to anti-Stokes lines.

Raman scattering has been extensively used to study the characteristics of (n, m) carbon nanotubes and to characterize their geometric structure [38]. Particular attention has been given to the radial breathing mode of carbon nanotubes (RBM) [38, 47, 48]. The unique properties of RBM can be used for the structural characterization of carbon nanotubes.

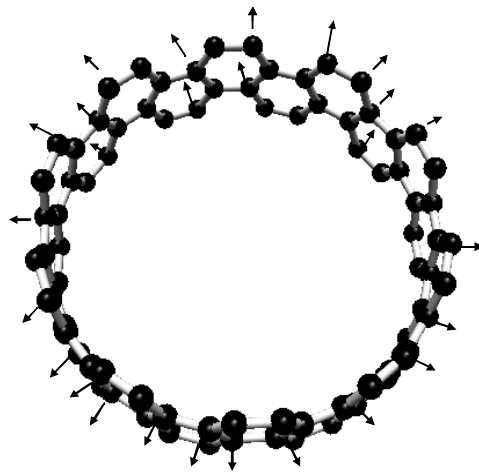


Figure (4.24): The radial breathing mode (RBM) of SWCNT

Raman spectra were measured using a Jobin Yvon Lab Raman spectrometer. The laser excitation wavelength was 632 nm with a spectral resolution of 4 cm^{-1} . Raman spectroscopy is used to determine the diameter of SWCNT as used in this work.

4.3.4.1 Raman Spectroscopy of SWCNTs

Figure (4.25) gives a general view of Raman spectra from various SWCNT samples. The Raman spectrum of SWCNTs has two important regions. The first one is a high-

frequency band around 1560 cm^{-1} and related to the tangential Raman mode in graphite which is called the G-band (tangential G-band from graphite as in the plane mode). It originates from the stretching of the double bonds in the graphitic structure. The second region is dominated by a low-frequency band ranging from 173 to 214 cm^{-1} that originates from a radial breathing mode (RBM) and is unique for SWCNTs. Its position and shape depends strongly on the exciting laser wave length as demonstrated for the first time by Rao et al. [38].

Further, one observes the D-band (1300 cm^{-1}) which comes from the graphite defects, and a G* band at about 2700 cm^{-1} which is the second order harmonic of the D-band.

Table (4.2): The distribution frequencies of SWCNTs in the sample.

Notation	Frequency (cm^{-1})	Type of mode
Radius Breathing Mode (RBM)	~248	Radius Breathing mode of SWCNT
G-Band	~1300-1600	Graphite mode
G* Band	~2700	Overtone of D-band

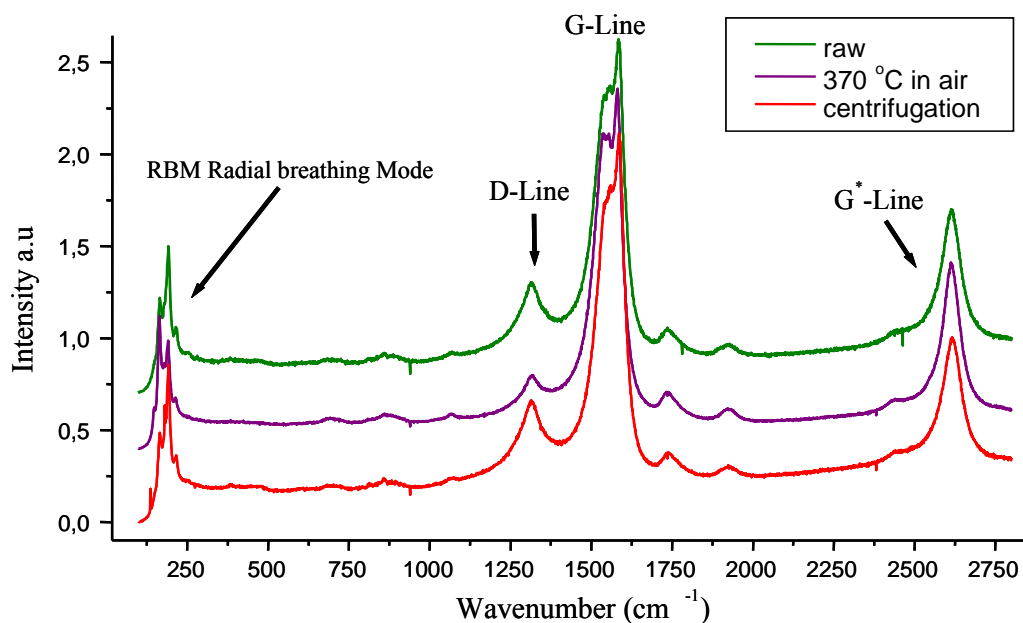


Figure (4.25): Raman spectrum of three SWCNT samples measured at laser wave line $\lambda = 632$ nm, showing the radial breathing mode (RBM), the D-band, the G-band, and the G^{*}-band.

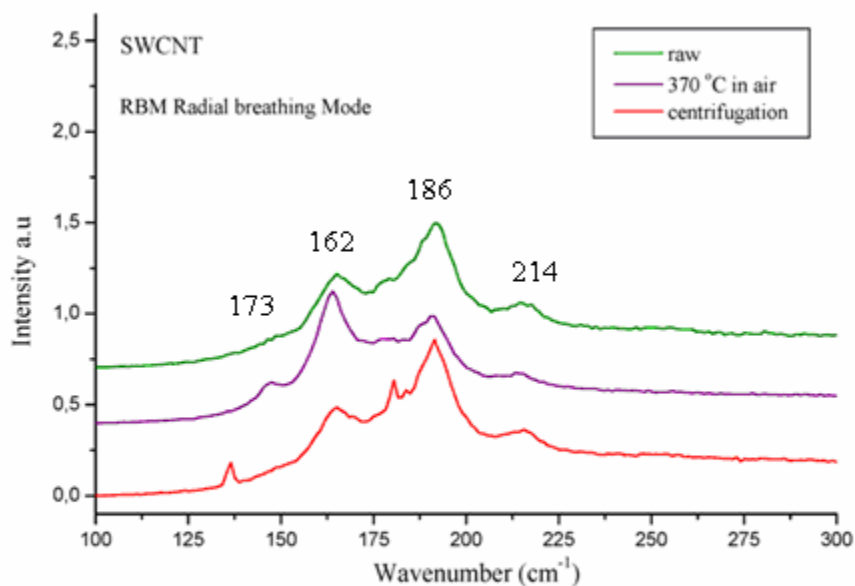


Figure (4.26): Distributions of SWCNTs Radial breathing mode (RBM)

Figure (4.26) shows the radial breathing modes frequencies for the samples typically used in these studies (SWCNT with Fe Catalyst). In this figure there are four peaks at 173, 162, 186 and 214 cm^{-1} , from which we can calculate the distribution of the diameters d of single wall carbon nanotubes from the relation $\omega^{RBM} = C/d$ [47-48] with $C = 218 \text{ cm}^{-1} \text{ nm}$. This leads to $d = 0.79 \text{ nm}$, 0.83 nm , 0.89 nm and 1.03 nm . Different groups have used different values for the constant $C = 218$ [49], 223.75 [48], 234 [50], 232 [51], 248 [52], and 223.5 [53], all in $\text{cm}^{-1} \text{ nm}$.

4.3.5 X-Ray Diffraction (XRD)

The regular periodic array of atoms in a crystal line solid scatters X-rays coherently, leading to a constructive interference at specific angles (i.e. diffraction in analogy to optics). The first description of the diffraction of X-rays by crystals was developed by Max von Laue [54]. According to Bragg law, diffraction phenomena in crystals occur as shown in figure (4.27). X-rays reflect from crystallographic planes, which are identified by the values of θ_{hkl} of a three-dimensional crystal. The scattered X-rays of each lattice plane make a constructive interference with each other if the path difference Δl between the waves is a multiple integer n of the wavelength λ . This will produce strong diffraction peaks when the angle between the beam and surface satisfies the Bragg condition which is given as a difference in the optical path length:

$$\Delta l = 2d_{hkl} \sin 2\theta_{hkl} = n\lambda \quad (4.1)$$

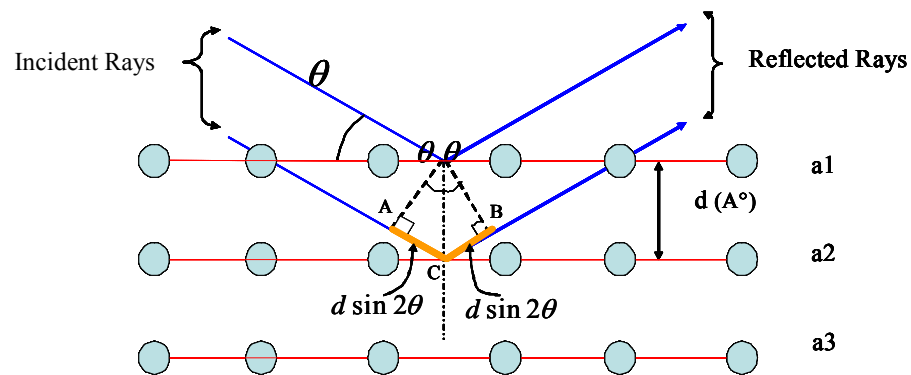


Figure (4.27): The basic principle of X-ray diffraction (XRD)

This relates the spacing between the crystal planes, hkl , to the particular Bragg angle, θ_{hkl} , at which reflections from these parallel planes a_1 , a_2 and a_3 occur. In figure (4.27) the path difference between the waves scattered by atoms from adjacent lattice planes of spacing hkl (Miller Indices) is given by the sum of AC and CB.

A finely grounded crystalline powder contains a very large number of small crystallites, which are oriented randomly to one another. If such a sample is placed in the path of a monochromatic X-ray beam, diffraction will occur from planes in those crystallites which happen to be oriented at the correct angle to fulfill the Bragg condition. The diffracted beams make an angle of 2θ with the incident beam. In practice, the sample is rotated to bring as many planes as possible into the diffracting condition. Powder X-ray patterns were recorded in 2 theta geometry using STOE diffraction system equipped with a Cu target (wavelength 1.54 \AA).

4.3.5.1 X-Ray Diffraction (XRD) Measurements

In Figure (4.28) we see XRD diffractograms of SWCNTs at different purification stages. The green curve belongs to raw SWCNTs, the violet to SWCNTs heat-treated by 370°C and the red to four time centrifuged samples.

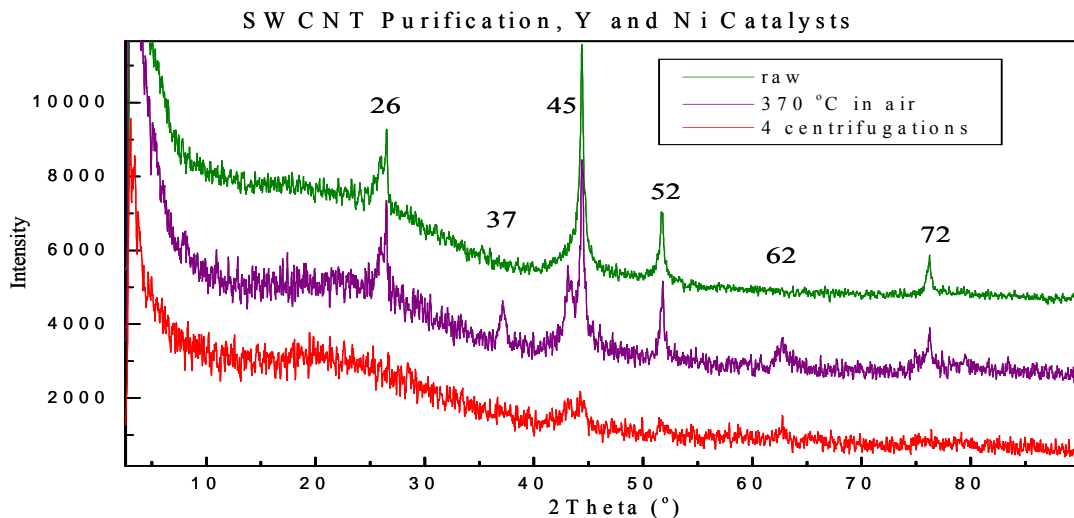


Figure (4.28): XRD diffractograms of SWCNT characterized at each stage by powder X-ray diffraction.

The XRD spectra of the synthesized single-walled carbon nanotubes show that Fe and NiY particles are not quickly released in the acidic purification process of the first cycle (figure 4.28). The reason probably is that NiY particles are enclosed in the hollow channel of the nanotubes or they are encapsulated in other carbon material. The diffraction peaks of which the lines are indicated (26° , 37° , 45° , 52° , 62° and 76°), correspond to the three most intense peaks of NiY carbide. The carbide peaks are more intense for higher iron ratios in the precursor powder. The peak at $\sim 43^\circ$ corresponds to the diffraction peak of graphite and is also present in nanotubes. The more intense carbide peaks at high iron ratios could be due to carbide inside SWNT whose diameter is bigger for high iron ratios.

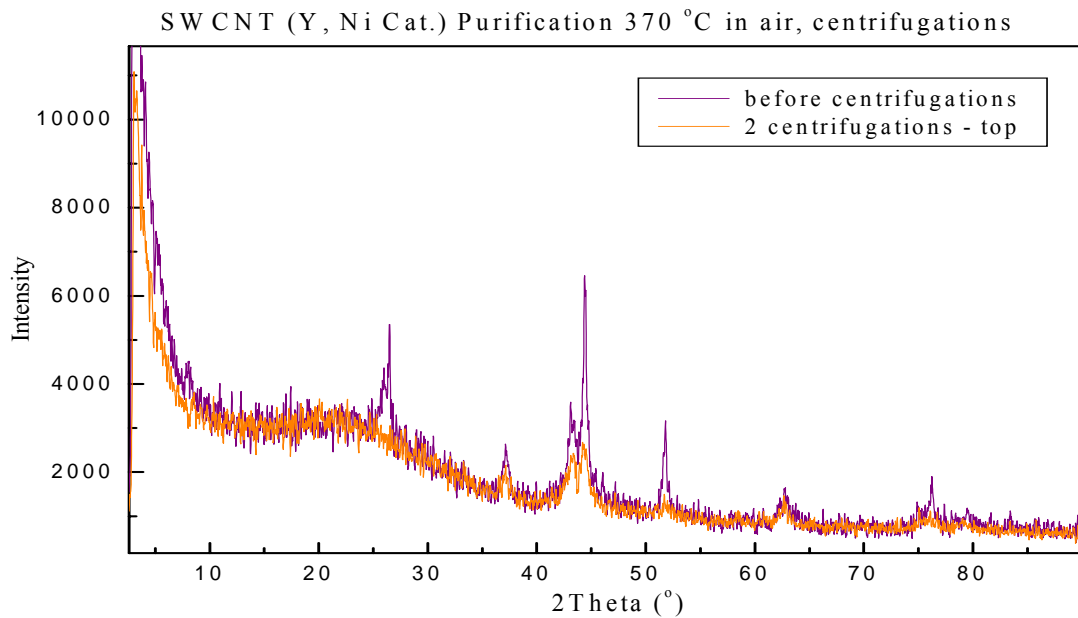


Figure (4.29): The effect of centrifugation: X-ray diffraction patterns of the SWCNTs are heat-treated in air at 370 °C

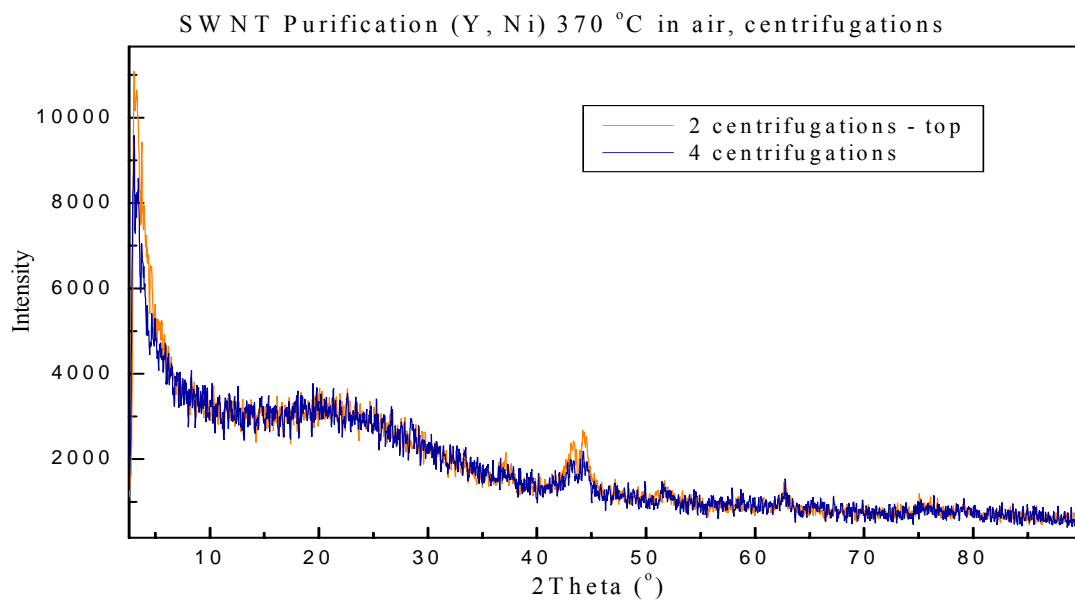


Figure (4.30): *The effect of centrifugation: X-ray diffraction patterns of the SWCNTs heat-treated at 370 °C and more centrifugation.*

4.4 References to Chapter Four

- [1] S. Saito, *Science* **1997**, 278, 77.
- [2] H. Dai, A. G. Rinzler, P. Nikolaev, A. Thess, D. T. Colbert, R. E. Smalley, *Chem. Phys. Lett.* 1996, 260, 471.
- [3] M.S. Dresselhaus, G. Dresselhaus, P.C. Eklund, “*Science of Fullerenes and Carbon Nanotubes*”, Academic Press, **1996**, Ch. 29.
- [4] T. Guo, R. E. Smalley, *Proc. Electro. Chem. Soc.* **1995**, 95 (10), 636.
- [5] L. P. F. Chibante, A. Thess, J. M. Alford, M. D. Diener, R. E. Smalley, *J Phys. Chem.* 1993, 97, 8696.
- [6] C. L. Fields, J. R. Pitts, M. J. Hale, C. Bingham, A. Lewandowski, D. E. King, *J Phys. Chem.* 1993, 97, 8701.
- [7] P. Bemier, D. Laplace, J. Auriol, L. Barbedette, G. Flammant, M. Lebrun, A. Brunelle, S. Della-Negro, *Synth. Met.* 1995, 70, 1455.
- [8] C. Journet, W. K. Maser, P. Bemier, A. Loiseau, M. Lamy de la Chapelle, S. Leftant, P. Deniard, R. Lee, J. E. Fischer, *Nature (London)* **1997**, 388, 756.
- [9] J. C. Charlier, S. Iijima, *Topics Appl. Phys.* **1992**, 80, 55, **2001**.
- [10] G. Cuniberti, G. Fagas, K. Richter, “*Introducing Molecular Electronics (Lecture Notes in Physics)*”, Springer-Verlag. Berlin, **2007**.
- [11] Appenzeller, E. Joselevich.; W. Hoenlein, Carbon Nanotubes for Data Processing. Chapter 19 in *Nanoelectronics and Information Technology*; Waser, R., Ed.; Wiley-VCH: Weinheim, 473, **2003**.
- [12] A. G. Rinzler, J. Liu, H. Dai, P. Nikolaev, C.B. Huffman, F. J. Rodriguezmacias, P. J. Boul, A. H. Lu, D. Heymann, D. T. Colbert, R. S. Lee, J. E. Fischer, A. M. Rao, P. C. Eklund, R. E. Smalley, *Appl. Phys. A*, **1998**, 67, 29.
- [13] Y. Saito, M. Inagaki, *Jpn. J. Appl. Phys.* **1993**, 32, 1954.
- [14] S. Iijima, *Nature* **1991**, 354, 56.
- [15] T. W. Ebbesen, P. M. Ajayan, *Nature (London)* **1992**, 358, 220.
- [16] R. Bacon, *J. Appl. Phys.* **1960**, 31, 283.
- [17] W. Krätschmer, L. D. Lamb, K. Fostiropoulos, D. R. Huffman, *Nature* **1990**, 37, 354.
- [18] P. A. Ajayan, S. Iijima, *Nature* **1992**, 358, 23.

- [19] V. P. Dravid, X. Lin, Y. Wang, X. K. Wang, A. Yee, J. B. Ketterson, R. P. H. Chang, *Science* **1993**, 259, 1601.
- [20] S. Iijima, *Mater. Sci. Eng. B* **1993**, 19, 172.
- [21] S. Iijima, H. Takikawa, M. Ikeda, K. Hirahara, Y. Hibi, Y. Tao, P. A. Ruiz, Jr, T. Sakakibara, S. Itoh. *Physica B: Condensed Matter*, **2002**, 323, Issue 1, 277.
- [22] Y. L. Li, Y. D. Yu, Y. Liang, *J. Mater. Res.* **1997**, 12, 1678.
- [23] D. T. Colbert, J. Zhang, S. M. McClure, P. Nikolaev, Z. Chen, J. H. Hafner, D. W. Owens, P. G Kotula, C. B. Carter, J. H. Weaver, A. G. Rinzler, R. E. Smalley. *Science* 1994, 266, 1218.
- [24] T. Guo, P. Nikolaev, A. G. Rinzler, D. Tomanek, D. T. Colbert, R. E. Smalley, *J. Phys. Chem.* **1995**, 99, 10694.
- [25] A. Thess, R. Lee, P. Nikolaev, H. Dai, P. Petit, J. Robert, C. Xu, Y.H. Lee, S.G. Kim, A.G. Rinzler, D.T. Colbert, G.E. Scuseria, D. Tomanek, J.E. Fischer, R.E. Smalley, *Science* **1996**, 273, 483.
- [26] I. Wirth, S. Eisebitt, G. Kann, W. Eberhardt, *Phys. Rev. B* **2000**, 61, 5719.
- [27] H. Kataura, Y. Kumazawa, Y. Maniwa, I. Umezue, S. Suzuki, Y. Ohtsuka and Y. Achiba, *Synthetic Metals*, **1999**, 103, 2555
- [28] J. Kong, H. T. Soh, A. M. Cassell, C. F. Quate, H. Dai, *Nature* **1998**, 395, 878.
- [29] V. Ivanov, A. Fonseca, I. B. Nagy, A. Lucas, P. Lambin, D. Bemaerts, X. B. Zhang, *Carbon* **1995**, 33, 1727.
- [30] M. Yudasaka, R. Kikuchi, T. Matsui, Y. Ohki, S. Yoshimura, E. Ota, *Appl. Phys. Lett.* **1995**, 67, 17.
- [31] Z. F. Ren, Z. P. Huang, D. Z. Wang, J. G. Wen, J. W. Xu, J. H. Wang et al., *Appl. Phys. Lett.* **1999**, 75, 8.
- [32] M. Yukasaka, R. Kikuchi, Y. Ohki, E. Ota, S. Yoshimura, *Appl. Phys. Lett.* **1997**, 70, 14.
- [33] Z. F. Ren, Z. P. Huang, J. W. Xu, J. H. Wang et al., *Science* **1998**, 282, 1105.
- [34] Y. C. Choi, Y. M. Shin, B. S. Lee, et al., *Appl. Phys. Lett.* **2000**, 76, 16.
- [35] M. J. Bronikowski, P. A. Willis, D. T. Colbert, K. A. Smith, R. E. Smalley, *J Vac. Sci. Technol, A* **2001**, 19, 1800

- [36] A. Loiseau, P. Launois, P. Petit, S. Roche, J.-P. Salvetat, *Understanding Carbon Nanotubes: From Basics to Applications (Lecture Notes in Physics)*, Springer, **2006**.
- [37] P. Nikolaev, M. J. Bronikowski, R. K. Bradley, F. Rohmund, D. T. Colbert, K. A. Smith, R. E. Smalley, *Chem. Phys. Lett.* **1999**, 91, 313.
- [38] A. M. Rao, E. Richter, S. Bandow, B. Chase, P. C. Eklund, K.W. Williams, M. Menon, K. R. Subbaswamy, A. Thess, R. E. Smalley, G. Dresselhaus, and M. S. Dresselhaus, *Science* **1997**, 275, 187.
- [39] K.B. Shelimov, R.O. Rinat, A.G. Rinzler, C.B. Huffman, R.E. Smalley, *Chem. Phys. Lett.* **1998**, 282, 429.
- [40] G.S. Duesberg, W. Blau, H.S. Byrne, S. Muster, M. Burghard, S. Roth: *Synth. Met.* **1999**, 103, 2484.
- [41] J L. Zimmerman, R. K. Bradley, C. B. Huffman, R. H. Hauge and J. L. Margrave *Chem. Mater.* **2000**, 12, 1361.
- [42] I. W. Chiang, B. E. Brinson, R. E. Smalley J. L. Margrave and R. H. Hauge *J. Phys. Chem.* **2001**, B105, 1157.
- [43] K. Koga, G. T. Gao, H. Tanaka, X. C. Zeng, *Nature* **2001**, 412, 802.
- [44] C. N. R. Rao B. C. Satishkumar A. Govindaraj and M. Nath *Chem. Phys. Chem.* **2001**, 2, 78.
- [45] T.R. Crompton, *Polymer Reference Book*, Rapra, **2006**.
- [46] Y. Gogotsi, J. A. Libera, A. G. Yazicioglu, C. M. Megaridis, *Appl. Phys. Lett.* **2001**, 79, 1021.
- [47] R. Saito, M. S. Dresselhaus, G. Dresselhaus, “*Physical Properties of Carbon Nanotubes*”, Imperial College Press, London, **1998**.
- [48] S. Bandow, S. Asaka, Y. Saito, A. M. Rao, L. Grigorian, E. Richter, and P. C. Eklund, *Phys. Rev. Lett.* **1998**, 80, 3779.
- [49] R. A. Jishi, L. Venkataraman, M. S. Dresselhaus, G. Dresselhaus, *Chem. Phys. Lett.* **1993**, 209, 77.
- [50] J. Kurti, G. Kresse, H. Kuzmany, *Phys. Rev.* **1998**, B 58, 8869.
- [51] D. Sanchez-Portal, E. Artacho, J. M. Soler, A. Rubio, P. Ordejón, *Phys. Rev. B* **1999**, 59, 12678.

- [52] A. Jorio, R. Saito, J. H. Hafner, C. M. Lieber, M. Hunter, T. McClure, G. Dresselhaus, M. S. Dresselhaus, *Phys. Rev. Lett.* **2001**, 86 1118.
- [53] S. M. Bachilo, M. S. Strano, C. Kittrell, R. H. Hauge, R. E. Smalley, R. B. Weisman, *Science*. **2002**, 298, 2361.
- [54] C. Kittel, “*Introduction to solid state physics*”, John Wiley and Sons, Inc. New York, **1996**.

5

Chapter Five:

Proton Nuclear Magnetic Resonance Spectroscopy

5.1 Introduction

This chapter introduces the basics of Nuclear Magnetic Resonance (NMR). A few fundamental concepts in both classical and quantum mechanics will be described.

In 1945 the nuclear magnetic resonance phenomenon in bulk matter was found by two groups. Purcell et al. [1] observed weak radio frequency signals in a lump of paraffin wax while Bloch et al. [2] observed radio frequency signals from the protons in water. Over the last few decades, NMR spectroscopy has grown into a crucial tool for chemical analysis, structure determination and the study of dynamics in inorganic, organic and biological systems [3-10]. It encompasses such diverse areas as cells, bones, protein folding, liquid crystals, laser-polarized gases, superconductors, zeolites, blood flow, quantum geometric phases, polymers, geology, colloids, catalysis, metals, quantum exchange, phase transitions, ionic conductors, quantum computing and many other applications [11]. In addition, the NMR technique has evolved into one of the most important imaging techniques in medicine.

The importance of NMR for chemistry is based on the discovery that the resonance frequency of a magnetic atomic nucleus in a magnetic field depends on the chemical environment of that atom or the molecular structure.

NMR is a spectroscopic technique which uses photons in the radio frequency range of the electromagnetic spectrum. The typical wavelength is around 1 m (300 MHz) [11]. Figure (5.1) shows the radio frequencies at the low end of the electromagnetic spectrum.

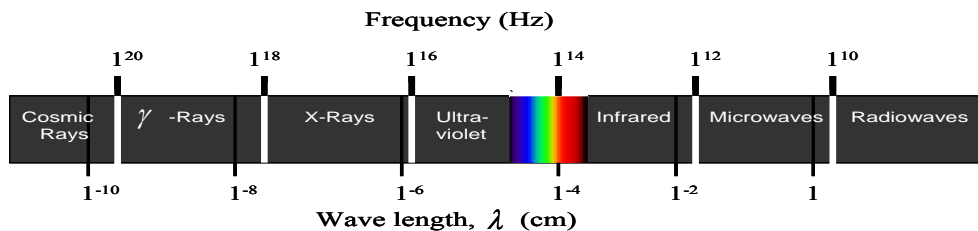


Figure (5.1): The range of radio frequencies in the electromagnetic spectrum

As the popularity and development of liquid-state NMR grew for chemists, solid-state NMR was used mainly by physicists. This is due to the fact that for solids the spectral resolution is low, resulting from several line-broadening effects that are not present in liquids. By the development of new techniques, the spectral resolution of solid state spectra has been improved so that solid state NMR has also become important for chemists [12]. One of the first techniques is Magic-Angle Spinning (MAS), developed in 1959 by Andrew [13] and Lowe [14]. It was shown that in principle MAS could eliminate most of the line broadening effects.

In addition, the works of Stejskal et al. [15] and Pines et al. [16] in the 1970s have contributed to further improvements of solid state NMR. Both reported that MAS narrowed ^{13}C spectra. Further developments involved the technique of spin decoupling and Cross Polarization (CP). CP increases the sensitivity of nuclei with low gyromagnetic ratio and low abundance (e.g. ^{13}C) by transferring polarization from a spin species that has a high gyromagnetic ratio and high abundance, e.g. ^1H [16].

5.2 Physics of Nuclear Magnetic Resonance Spectroscopy

There are three common techniques to study the structure of molecules and solids.

The first technique is X-ray diffraction which has provided the experimental basis of the knowledge on molecules. For locating atoms in a structure at high resolution, very well ordered single crystals are required [17-19].

The second technique is neutron diffraction which locates the lighter atoms. However, the application of neutron diffraction is limited due to its cost and the requirement of large quantity of sample [20-21].

NMR is the third technique for which a few milligrams of powdered sample is enough to run the experiment. Here this spectroscopy will be the main tool to retrieve the information we are looking for.

Although diffraction methods are very good at determining the molecular structure, they are mostly limited to crystalline materials and give very little information on the dynamics of the system. NMR spectroscopy can be used to get around this limitation. The information provided

by NMR is related to the physical state of the system and by the mobility of the molecules under investigation.

5.2.1 The Nucleus

Not every kind of nucleus will give a NMR signal, only those nuclei that have spin angular momentum $J \neq 0$ and magnetic dipole moment μ . Most nuclei have at least one isotope with a non-zero spin angular momentum, making it magnetically active and detectable by NMR. Table (5.1) shows the common NMR observable nuclei.

The nuclear spin angular momentum $J = \hbar I$ ($\hbar = \frac{h}{2\pi}$) is a quantum mechanical operator. The operator I^2 has eigenvalues $I(I+1)$ where the spin quantum number I has one of the following discrete values $0, \frac{1}{2}, 1, \dots$. The nuclei that have $I = 0$ possess no angular momentum, this class of nuclei includes all those that have both an even atomic number and an even mass number (see table 5.1). Therefore, they cannot experience any magnetic resonance effect under any circumstance. When either the atomic number or atomic mass is odd or both are odd, the nucleus has a spin (I not equal zero) and makes that nucleus visible in NMR.

The nuclei with a spherical nuclear charge distribution have a spin $I = \frac{1}{2}$. The nuclei with a non-spherical or ellipsoidal nuclear charge distribution have an electric quadrupole moment and a spin I of one or more (figure 5.2). My present concern is with ^1H which has $I = \frac{1}{2}$.

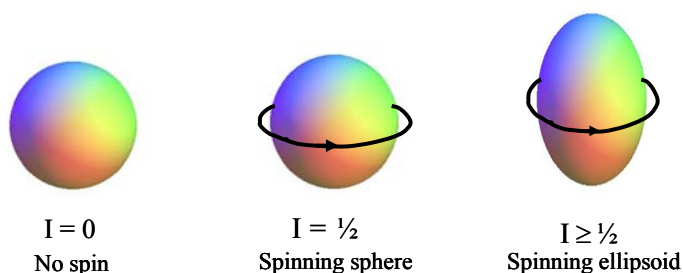


Figure (5.2): The classes of nuclear charge distribution

Table (5.1): The properties of some common nuclei.

Nucleus	$\gamma/10^7\text{T}^{-1}\text{rad s}^{-1}$	ν/MHz (at 9.4 T)	abundance	receptivity (relative to ^1H)	
^1H	$\frac{1}{2}$	26.752	400.00	99.99 %	1.00
^{13}C	$\frac{1}{2}$	6.728	100.58	1.1 %	$1.76 \cdot 10^{-4}$
^{14}N	1	1.934	28.89	99.6 %	$1.01 \cdot 10^{-3}$
^{15}N	$\frac{1}{2}$	-2.713	40.53	0.37 %	$3.85 \cdot 10^{-6}$
^{17}O	$\frac{5}{2}$	-3.628	54.23	0.04 %	$1.08 \cdot 10^{-5}$
^{19}F	$\frac{1}{2}$	25.182	376.31	100 %	0.83
^{27}Al	$\frac{5}{2}$	6.976	104.23	100 %	0.21
^{29}Si	$\frac{1}{2}$	-5.319	79.46	4.7 %	$3.69 \cdot 10^{-4}$
^{31}P	$\frac{1}{2}$	10.839	161.92	100 %	$6.63 \cdot 10^{-2}$

The coefficient γ is characteristic for each nuclear species and is called the gyromagnetic ratio; for protons $\gamma = 26.75 \times 10^7 \text{ rad s}^{-1} \text{ T}^{-1}$ ($\gamma/2\pi = 42.58 \text{ MHz T}^{-1}$) [22].

5.2.2 Theoretical Description of the Interaction of a Spin with a Magnetic Field

The general theory of NMR can usually be developed from two different viewpoints: quantum mechanical and classical; each of these perspectives has advantages and disadvantages. The quantum mechanical description is based on discrete energy levels, with transitions between them, whereas the classical description is based on magnetic moment vectors precessing around a magnetic field vector.

As we will see in the next subsections, a different theoretical framework will be used in explaining various aspects of NMR phenomena to give simple explanations.

5.2.2.1 Quantum Mechanical Description

In the Quantum Mechanical picture the total angular momentum of any isolated particle such as a proton is not free to assume any arbitrary value but may only take certain discrete values. The proton possesses a nuclear angular momentum J and spin quantum number $I = \frac{1}{2}$.

Due to quantum mechanical restrictions only one of three Cartesian components of \mathbf{J} can be specified. The z component of the angular momentum J_z is given by:

$$J_z = \hbar m_l \quad (5.1)$$

Equation (5.1) shows that the projection of nuclear angular momentum on the z axis is quantized and has a total of $2I+1$ possible values, the magnetic quantum number m_l takes the possible values of $I, I-1, I-2, \dots, -I+1, -I$. The magnetic quantum number m_l defines the orientations or the allowed values of nuclear angular momentum in space. The allowed energies and wave functions for molecules and atoms are found by solving the Schrödinger equation.

Nuclei that have spin angular momentum possess a nuclear magnetic dipole moment. The magnetic dipole moment μ is proportional to its angular momentum \mathbf{J} . It can be defined by:

$$\mu = \gamma \mathbf{J} \quad (5.2)$$

By combination of equation (5.1) and (5.2) we obtain the relationship between the magnetic moment and the angular momentum quantum number I :

$$|\mu| = \gamma \hbar \sqrt{I(I+1)} \quad (5.3)$$

$$\mu_z = \gamma \hbar m_l \quad (5.4)$$

In a magnetic field the nuclear magnetic moment μ can only have $(2I+1)$ orientations in the field, thus there are $(2I+1)$ allowed energy levels, each energy level of the particle may be specified by the quantum numbers I, m_l and a stationary-state wave function (eigenfunction). The proton, with spin quantum number $I = 1/2$, has two possible values for m_l , either aligned with (spin up) or against the applied field (spin down). The nuclear magnetic moment itself cannot be aligned exactly along the applied field, since this would violate the uncertainty principle, but precesses around the field $B_0 \parallel z$. So there are two energy states which correspond to low and high energy. The precession is represented by two cones as shown in figure (5.3) below.

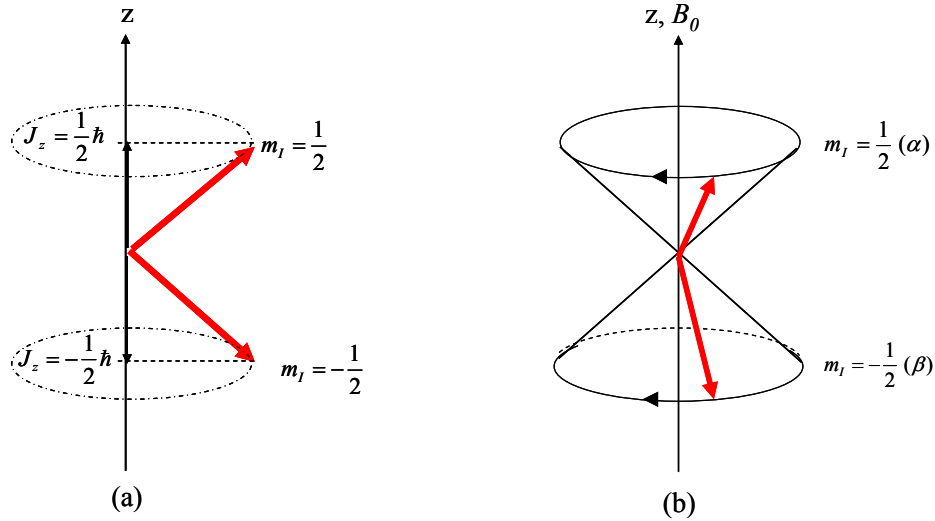


Figure (5.3): (a): Orientation of angular momentum \mathbf{J} in the magnetic field for proton with $I = 1/2$: **(b):** Precession of the nuclear dipole of a proton around a cone and energy states with α spin and β spin

Figure (5.3) shows that the spin (proton) with the m_l value $1/2$ is called α spin and that with $-1/2$ is called β spin; it is noteworthy that the energy of β spin is higher than the energy of α spin. Therefore, the energy is lowest when the magnetic moment is aligned with the magnetic field and highest when it is in the opposite direction to the field.

Equation (5.5) shows the energy difference of these two possible orientations, ΔE which is linearly dependent on the strength of the magnetic field \mathbf{B}_0 :

$$\Delta E = \gamma \hbar B_0 \quad (5.5)$$

The transitions between the two states can be induced by applying electromagnetic energy at a frequency ω_0 , this frequency is represented by equation (5.6).

$$\omega_0 = \Delta E / \hbar = \gamma B_0 \quad (5.6)$$

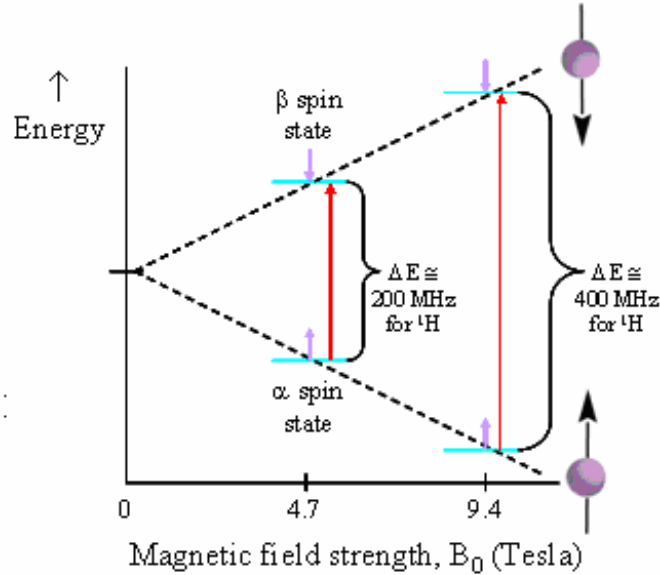


Figure (5.4): Energy levels of a nuclear spin with $I = \frac{1}{2}$ as a function of the magnetic field B_0 .

This is called the resonance condition, and the resonance frequency is directly proportional to the applied magnetic field strength B_0 .

5.2.2.2 Classical Mechanical Description

It is usually easier, however, to visualize NMR experiments by using Classical Mechanics, as the number of nuclei is large for which all possible orientations of the spin in a magnetic field are allowed. For $I = \frac{1}{2}$, the predictions of the classical model for a macroscopic system agree with those of the quantum theory.

In classical mechanics, angular momentum is employed when considering the rotation of a point particle of mass m , whose position with respect to given origin is r and whose momentum is $p = mv$, where v is its velocity. The angular momentum of this particle is given by:

$$\mathbf{J} = \mathbf{r} \times \mathbf{p} \quad (5.7)$$

The effect of the static field on the magnetic moment $\boldsymbol{\mu}$ can be described in the classical description. Spins in a magnetic field will experience a torque $\boldsymbol{\tau}$ perpendicular to the magnetic moment $\boldsymbol{\mu}$ and causes the spins to trace a circular path in a plane perpendicular to the applied

magnetic field \mathbf{B}_0 :

$$\boldsymbol{\tau} = \boldsymbol{\mu} \times \mathbf{B}_0 \quad (5.8)$$

This motion is called precession or more specifically *Larmor precession* of the nucleus, the precession frequency is proportional to the static field.

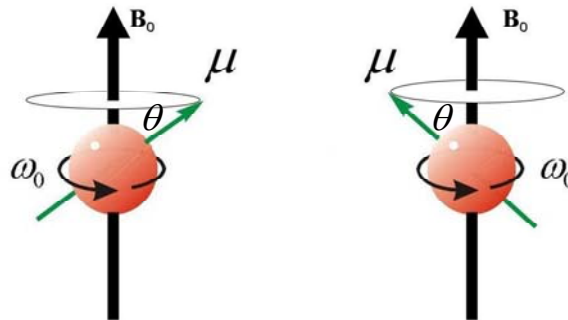


Figure (5.5): A static magnetic field applied to the nucleus causes it to precess at a rate dependent on the field strength and the gyromagnetic ratio

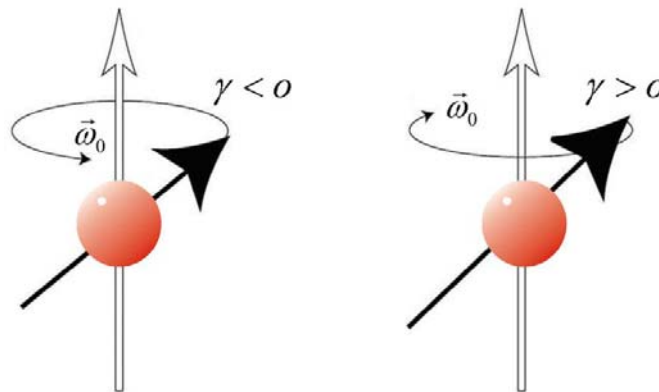


Figure (5.6): The positive precession for nuclei with negative gyromagnetic ratio (left), and negative precession for nuclei with positive gyromagnetic ratio (right)

When $\boldsymbol{\mu}$ interacts with \mathbf{B}_0 , the potential energy of this system is given by

$$E = -\boldsymbol{\mu} \cdot \mathbf{B} = -\mu B_0 \cos\theta \quad (5.9)$$

Classically, \mathbf{J} and θ can have any value and no restrictions on the allowed energy values exist in the classical picture as in the quantum model.

When the angular momentum \mathbf{J} precesses about \mathbf{B}_0 the rotational analogue of Newton's Second Law tells that the time derivative of angular momentum is given by:

$$\frac{d\mathbf{J}}{dt} = \boldsymbol{\tau} = \boldsymbol{\mu} \times \mathbf{B}_0 \quad (5.10)$$

which, combined with Equation (5.2), yields

$$\frac{d}{dt}\boldsymbol{\mu} = \boldsymbol{\mu} \times \gamma \mathbf{B}_0 \quad (5.11)$$

$$\frac{d}{dt}\boldsymbol{\mu} = \boldsymbol{\omega}_0 \times \boldsymbol{\mu} \quad (5.12)$$

where

$$\boldsymbol{\omega}_0 = -\gamma \mathbf{B}_0 \text{ in rad/s} \quad (5.13)$$

Equations (5.12) and (5.13) show that the nucleus precesses about the direction of the applied field at $\boldsymbol{\omega}_0$ rad/s, the minus sign gives the direction of precession.

Sofar we considered a single spin. In practical cases we have to deal with an enormous number of identical nuclei. When these nuclei are placed in the static magnetic field their spins orient either parallel or anti-parallel to the field. The orientation parallel to the static field has slightly lower energy (α) than the anti-parallel orientation (β). Therefore, at equilibrium, there is only a small excess of spins in α state which is defined by Boltzmann distribution:

$$N_\beta = N_\alpha e^{\left(\frac{-\Delta E}{k_B T}\right)} \quad (5.14)$$

where N_i is the population of the energy level i , ΔE is the energy difference between the two levels, k_B is the Boltzmann constant, and T is the absolute temperature.

The NMR signal arises from a collection of spins distributed randomly about the precessional cones of Fig. (5.3b). The vector that results from an ensemble of a large number of identical nuclear magnetic moments μ_i is called the bulk magnetization vector M and is aligned along the z-axis at equilibrium:

$$M = \sum \mu_i \quad (5.15)$$

5.2.3 The Rotating Frame of Reference

The description of NMR and its pictorial representations can often be simplified by transforming to a coordinate system that rotates with respect to the laboratory frame (figure 5.7).

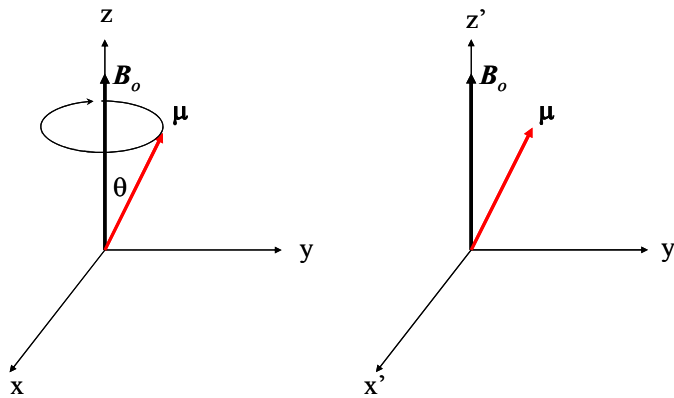


Figure (5.7): (Left): The nuclear magnetic moment μ rotates about the z axis of an applied magnetic field in the laboratory frame. (Right): The nuclear magnetic moment μ under the influence of an applied magnetic field appears stationary in the rotating frame of reference.

In a system of rectangular coordinate axes with unit vectors \mathbf{i} , \mathbf{j} , \mathbf{k} the magnetic moment can be expanded as:

$$\mu = \mu_x \mathbf{i} + \mu_y \mathbf{j} + \mu_z \mathbf{k} \quad (5.16)$$

Normally \mathbf{i} , \mathbf{j} , \mathbf{k} are constant in time but now we want to be more general. Then the time-derivative of μ is:

$$\frac{d\boldsymbol{\mu}}{dt} = \frac{d\mu_x}{dt} \mathbf{i} + \mu_x \frac{d\mathbf{i}}{dt} + \frac{d\mu_y}{dt} \mathbf{j} + \mu_y \frac{d\mathbf{j}}{dt} + \frac{d\mu_z}{dt} \mathbf{k} + \mu_z \frac{d\mathbf{k}}{dt}$$

or:

$$\begin{aligned} \frac{d\boldsymbol{\mu}}{dt} &= \left(\frac{d\mu_x}{dt} \mathbf{i} + \frac{d\mu_y}{dt} \mathbf{j} + \frac{d\mu_z}{dt} \mathbf{k} \right) + \left(\mu_x \frac{d\mathbf{i}}{dt} + \mu_y \frac{d\mathbf{j}}{dt} + \mu_z \frac{d\mathbf{k}}{dt} \right) \\ &= \frac{\partial \boldsymbol{\mu}}{\partial t} + \left(\mu_x \frac{d\mathbf{i}}{dt} + \mu_y \frac{d\mathbf{j}}{dt} + \mu_z \frac{d\mathbf{k}}{dt} \right) \end{aligned} \quad (5.17)$$

where $\frac{\partial \boldsymbol{\mu}}{\partial t}$ represents the motion of the magnetic moment in the coordinate system $\mathbf{i}, \mathbf{j}, \mathbf{k}$.

Since the lengths of the unit vectors \mathbf{i}, \mathbf{j} and \mathbf{k} are constant, they can only rotate. The rotation of the rotating frame relative to a fixed frame of reference is then described by:

$$\frac{d\mathbf{i}}{dt} = \boldsymbol{\omega} \times \mathbf{i} \quad \frac{d\mathbf{j}}{dt} = \boldsymbol{\omega} \times \mathbf{j} \quad \frac{d\mathbf{k}}{dt} = \boldsymbol{\omega} \times \mathbf{k} \quad (5.18)$$

Then:

$$\left(\frac{d\boldsymbol{\mu}}{dt} \right)_{lab} = \left(\frac{\partial \boldsymbol{\mu}}{\partial t} \right)_{rot} + \boldsymbol{\omega} \times \boldsymbol{\mu} \quad (5.19)$$

Equation (5.19) shows that in order to describe the motion of $\boldsymbol{\mu}$ relative to the coordinate system which rotates with angular frequency $\boldsymbol{\omega}$ an additional term $\boldsymbol{\omega} \times \boldsymbol{\mu}$ shows up. This is the analog of the Coriolis force. If we substitute equation (5.11) $\left(\frac{d\boldsymbol{\mu}}{dt} \right) = \boldsymbol{\mu} \times \gamma \mathbf{B}_0$ in equation (5.19):

$$\boldsymbol{\mu} \times \gamma \mathbf{B} = \left(\frac{\partial \boldsymbol{\mu}}{\partial t} \right)_{rot} + \boldsymbol{\omega} \times \boldsymbol{\mu} \quad \text{and rearrange we find:}$$

$$\left(\frac{\partial \boldsymbol{\mu}}{\partial t} \right)_{rot} = \boldsymbol{\mu} \times (\gamma \mathbf{B} + \boldsymbol{\omega}) = \boldsymbol{\mu} \times \gamma \left(\mathbf{B} + \frac{\boldsymbol{\omega}}{\gamma} \right) \quad (5.20)$$

By comparing equation (5.11) and (5.20) we conclude that in the rotating frame of reference, there is apparently an additional term to the magnetic field. We can define an ‘effective’ magnetic field \mathbf{B}_{eff} about which $\boldsymbol{\mu}$ rotates in the rotating frame. Thus equation (5.20) can be rearranged as

$$\left(\frac{\partial \boldsymbol{\mu}}{\partial t} \right)_{\text{rot}} = \boldsymbol{\mu} \times \gamma \mathbf{B}_{\text{eff}} \quad (5.21)$$

where

$$\mathbf{B}_{\text{eff}} = \mathbf{B}_0 + \frac{\boldsymbol{\omega}}{\gamma} \quad (5.22)$$

The term $\boldsymbol{\omega} / \gamma$ represents a “fictitious” field, which arises from the rotation of the $\mathbf{i}, \mathbf{j}, \mathbf{k}$ frame of reference.

For the bulk magnetization \mathbf{M} we find the similar equation:

$$\left(\frac{\partial \mathbf{M}}{\partial t} \right)_{\text{rot}} = \mathbf{M} \times \gamma \mathbf{B}_{\text{eff}} \quad (5.23)$$

When the angular frequency $\boldsymbol{\omega}$ of the rotating frame coincides with the Larmor frequency, $\boldsymbol{\omega}_0 = -\gamma \mathbf{B}_0$,

$$\boldsymbol{\omega} = \boldsymbol{\omega}_0 = -\gamma \mathbf{B}_0 \quad (5.24)$$

If we substitute this value of $\boldsymbol{\omega}$ in equation (5.22), then we see that \mathbf{B}_{eff} and $\frac{\partial \boldsymbol{\mu}}{\partial t}$ become zero.

This means that in the coordinate system with the unit vectors $\mathbf{i}, \mathbf{j}, \mathbf{k}$ which rotates with $\boldsymbol{\omega}_0$ around the direction of \mathbf{B}_0 , the vector of the magnetic moment $\boldsymbol{\mu}$ is static. This is exactly equivalent to the vector $\boldsymbol{\mu}$ precessing with the Larmor frequency in the laboratory frame of reference. The magnetic moment $\boldsymbol{\mu}$ is time independent in the rotating frame.

5.2.4 Radio-Frequency Pulses

Next we introduce the magnetic field \mathbf{B}_1 , a time dependent magnetic field in the laboratory frame. The \mathbf{B}_1 field is generated by applying a voltage, oscillating at ω , to the terminals of a suitable RF coil surrounding the sample. The coil axis is perpendicular to the \mathbf{B}_0 field. Often \mathbf{B}_1 is referred to as the radiofrequency (RF) field because $\omega/2\pi$ normally lies between 1MHz and 500 MHz.

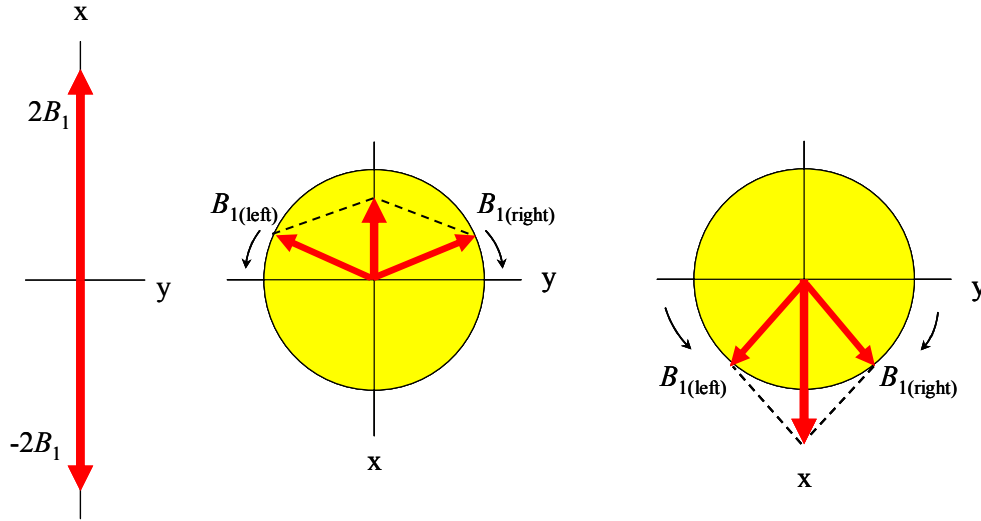


Figure (5.8): Representation of a linearly alternating field as the sum of two rotating fields ($B_{1(right)}$ clockwise) and $B_{1(left)}$ anticlockwise)

This generates a linearly oscillating field in the x-y plane perpendicular to the static magnetic field, which can be decomposed into two counter-rotating fields (figure 5.8):

$$\mathbf{B}_1 = (B_x \cos \omega t - B_y \sin \omega t) \mathbf{m} + (B_x \cos \omega t + B_y \sin \omega t) \mathbf{n} \quad (5.24)$$

where B_x and B_y are the components of \mathbf{B}_1 in the laboratory frame. Only the counter rotating component which rotates in the same direction as the precessing spins needs to be considered. The other component of \mathbf{B}_1 which appears in the rotating frame to precess at approximately twice the Larmor frequency can usually be ignored (see figure 5.9).

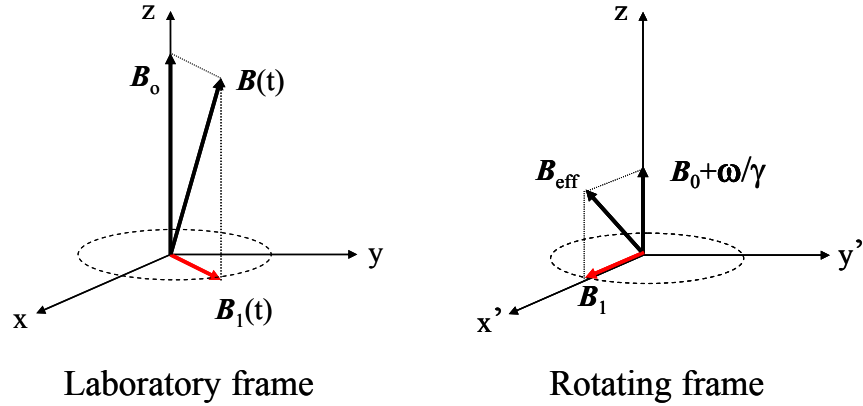


Figure (5.9): Magnetic fields in (a) the laboratory frame and (b) the rotating frame of reference

In the presence of the \mathbf{B}_1 field the effective field in the rotating frame changes to:

$$\mathbf{B}_{eff} = \mathbf{B}_0 + \frac{\boldsymbol{\omega}}{\gamma} + \mathbf{B}_1 \quad (5.25)$$

When the radio frequency coincides with the angular frequency of the rotating frame, \mathbf{B}_1 remains stationary relative to the unit vectors \mathbf{i} , \mathbf{j} and \mathbf{k} . The equation of motion (5.23) described the magnetic moment vector without \mathbf{B}_1 ; this equation will be rewritten with \mathbf{B}_1 field:

$$\left(\frac{\partial \mathbf{M}}{\partial t} \right)_{rot} = \mathbf{M} \times [(\gamma B_0 + \omega)\mathbf{k} + (\gamma B_1)\mathbf{i}] \quad (5.26)$$

When we substitute $\omega = -\gamma B_0$ in equation (5.26), the resonance condition, we have:

$$\left(\frac{\partial \mathbf{M}}{\partial t} \right)_{rot} = \mathbf{M} \times \gamma \mathbf{B}_1 \quad (5.27)$$

In the rotating frame, the magnetic moment \mathbf{M} sees only \mathbf{B}_1 and it precesses in the (y', z') plane about the direction of \mathbf{B}_1 .

When the B_1 -field is applied as a pulse (figure 5.10) the magnetization rotates over a certain angle θ . The flip angle θ will be dependent on the amplitude and duration of the pulse:

$$\theta = \gamma B_1 t_p \quad (5.28)$$

where t_p is the duration of the B_1 field pulse. Thus, it is possible to find the appropriate experimental condition for flipping M through any specified angle. The B_1 pulse length can be determined so that M will be flipped through 90° and this is called a 90° or $\pi/2$ pulse. Alternatively, if M is tipped right over onto the $-B_0$ direction, this is called a 180° , π or inversion pulse (figure 5.10).

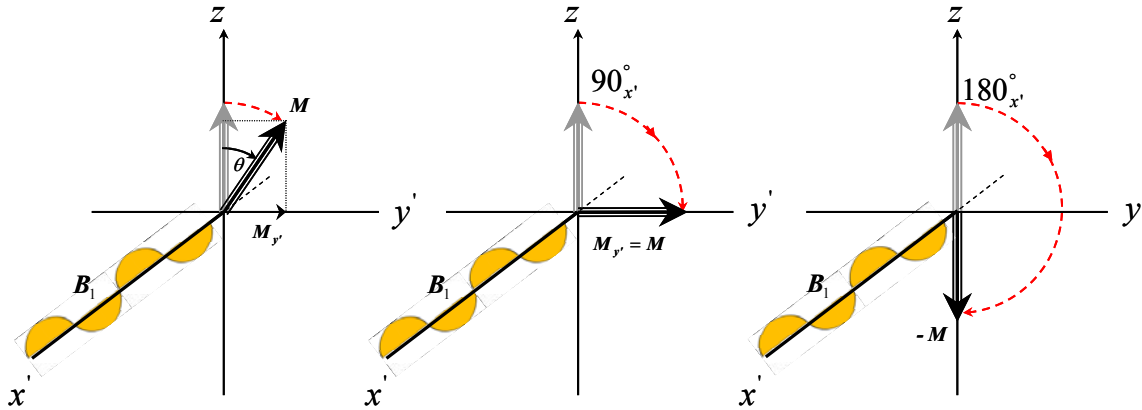


Figure (5.10): The effect of (a) a pulse of arbitrary angle θ ; b) after $90^\circ_{x'}$ pulse; c) after $180^\circ_{x'}$, all pulses are in the rotating frame of reference.

5.2.5 Relaxation Process

Spin relaxation is a process that occurs after the nuclear spins become excited by the radio frequency pulse. The rf pulse causes that the bulk magnetization vector M is no longer parallel to B_0 . Spin relaxation occurs via two separate processes: the first is longitudinal relaxation which describes the return of the magnetization M along the z-axis towards its initial equilibrium value. The second is transverse relaxation which describes the dephasing of M components in the x, y plane.

5.2.5.1 Spin-lattice or longitudinal relaxation (T_1)

Figure (5.11) shows the distribution of the spin populations of both energy levels (a) at equilibrium and (b) after excitation by a 90° pulse. The shaded spheres in (b) represent spins that have absorbed energy and changed their orientation with respect to the external field.

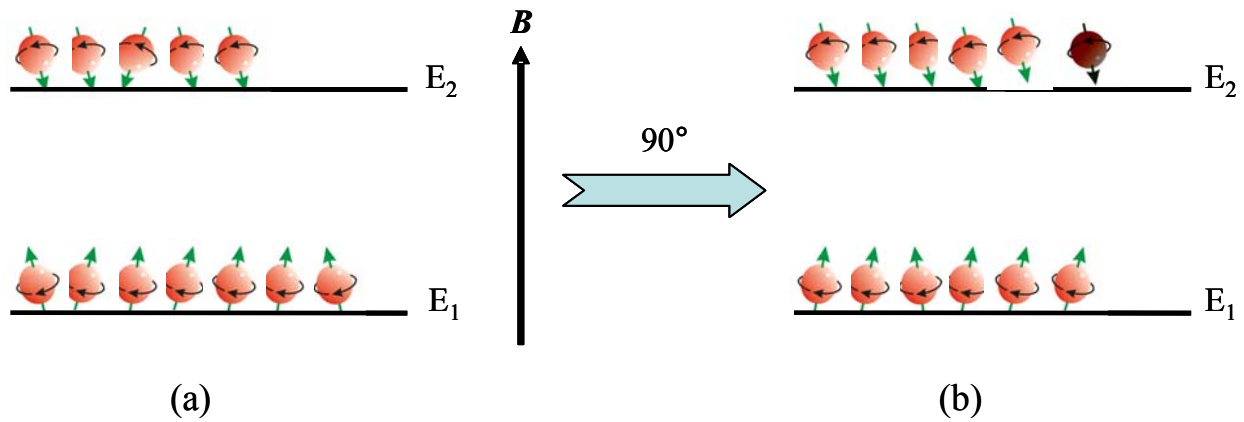


Figure (5.11): Distribution of the spin population **(a)** at equilibrium and **(b)** after excitation by a 90° pulse.

The spins are energetically coupled to a thermal reservoir, which is called the lattice. During spin-lattice relaxation the nuclei lose energy which is provided by the degrees of freedom of the surroundings (the lattice). Therefore, the spin-lattice relaxation is responsible for the re-establishment of thermal equilibrium between two spin energy states.

The net distribution of the magnetic moments along the external magnetic field is called the longitudinal magnetization, as shown in figure (5.12). During a 90° pulse M_z goes from its maximum value at equilibrium to zero and then recovers exponentially to the equilibrium state (figure 5.12). The recovery of M_z versus time after the 90 degree pulse is expressed as follows:

$$M_z(t) = M_0(1 - e^{-t/T_1}) \quad (5.29)$$

The duration T_1 , describes the re-establishment of thermal equilibrium after some perturbation is applied, it is called the longitudinal relaxation time or the spin-lattice relaxation time constant T_1 . It is the time needed to recover 63% of M_z after applying a 90° pulse [22].

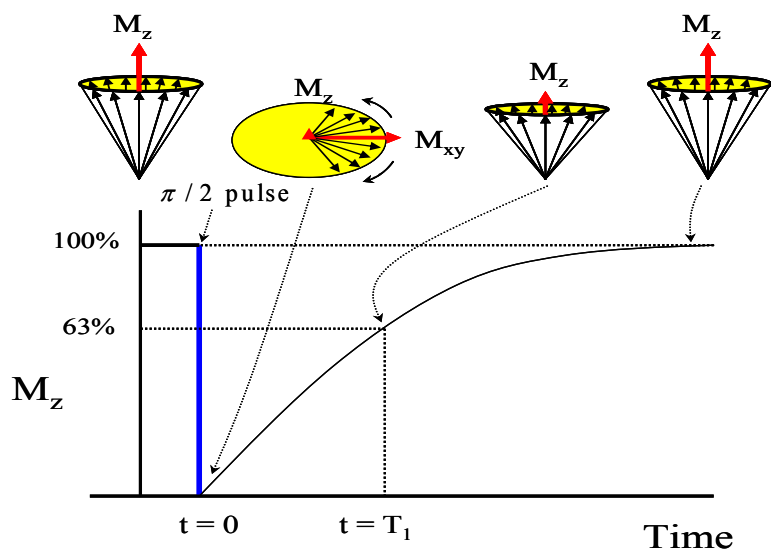


Figure (5.12): The longitudinal relaxation process.

5.2.5.2 Spin-spin or transverse relaxation (T_2)

Transverse or spin-spin relaxation is a process by which the magnetization vectors in the transverse plane lose their coherence. NMR spectroscopy detects only the magnetization, which is perpendicular to the field and cannot detect the parallel magnetization.

When a 90° pulse is applied to the equilibrium magnetization \mathbf{M} it will perturb the system. Directly after the pulse there is a bulk magnetization perpendicular to the main field in the xy plane. From the view of the individual spins this pulse produces phase coherence between the individual spins. After the pulse the spins and the bulk magnetization continue their precession with the Larmor frequency, ω_0 . Due to a loss of phase coherence between the spins the transverse bulk magnetization slowly decays. The decay is due to the gradual loss of synchronization between the precessing spins (figure 5.13).

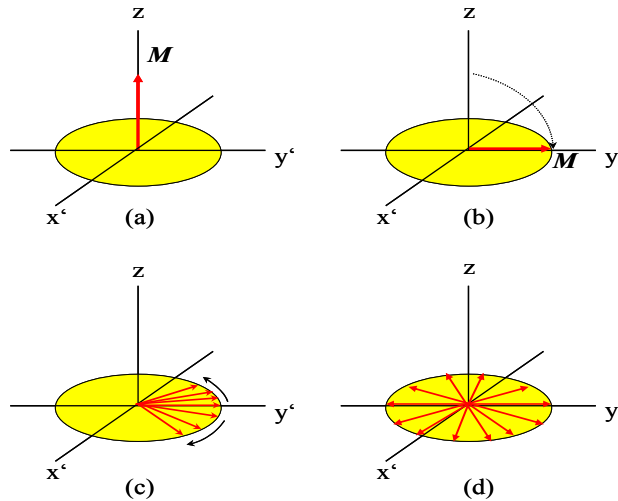


Figure (5.13): The transverse relaxation process (a) magnetization lies along the z axis; (b) magnetization is tipped into $x'y'$ plane; (c) spins begin to dephase; (d) spins are completely dephased.

The loss of M_{xy} phase coherence causes an exponential decay of the transverse magnetization with a time constant T_2 , the transverse or spin-spin relaxation time [22]. T_2 is the time in which the signal decays to 37% of the maximal transverse magnetization, as shown in figure (5.14).

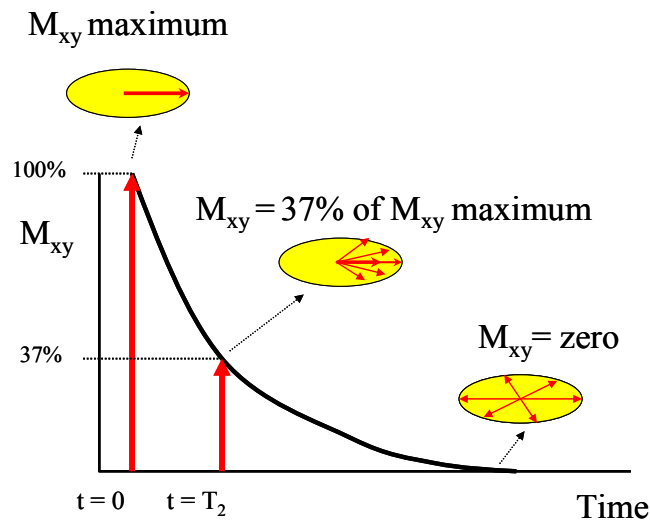


Figure (5.14): The transverse relaxation process.

5.3 Solid State Nuclear Magnetic Resonance

The anisotropic nuclear interactions are interesting phenomena in solid-state NMR spectroscopy.

The main problems of solid state NMR are caused by line-broadening effects. Therefore, solid state NMR spectra often are difficult to interpret due to the broad featureless line shapes.

5.3.1 Nuclear Spin Interactions in Solids [23-26]

The interactions that influence NMR spectroscopy are complex but they can be divided into categories. Each category is represented by a Hamilton operator. In general, the total solid state NMR Hamiltonian \hat{H} of a nuclear spin system can be written as

$$\hat{H} = \hat{H}_{ext} + \hat{H}_{int} \quad (5.30)$$

where \hat{H}_{ext} represents the external Hamiltonian and \hat{H}_{int} the internal Hamiltonian. The external Hamiltonian consists of two parts: the Zeeman Hamiltonian \hat{H}_Z , which pertains to the strong Zeeman interaction due to the external magnetic field \mathbf{B}_0 , and the interaction of spins with the radiofrequency field \mathbf{B}_1 . The external part of the spin Hamiltonian is:

$$\hat{H}_{ext} = \hat{H}_Z + \hat{H}_{rf} \quad (5.31)$$

The internal Hamiltonian consists of many terms:

$$\hat{H}_{int} = \hat{H}_D + \hat{H}_{CS} + \hat{H}_Q + \hat{H}_J \quad (5.32)$$

\hat{H}_{int} includes the intrinsic effects of magnetic and electric fields originating from the sample, \hat{H}_D is the coupling of nuclear spins with each other through the dipole-dipole interaction. \hat{H}_{CS} is the coupling with the induced magnetic field generated by the surrounding electrons which is called the chemical shift or magnetic shielding. \hat{H}_Q is the coupling of spins with electric field gradients. It occurs for nuclei with spin larger than one half and is called the quadrupolar interaction. \hat{H}_J comes from the coupling of spins with each other via electron spins, which is called the J coupling.

5.3.1.1 The Chemical Shift Interaction

In the electron cloud surrounding the nucleus the external magnetic field induces a magnetic moment which has a shielding effect on the nucleus. This interaction causes a shift in

the resonance frequency of that nucleus, the chemical shift, which is proportional to \mathbf{B}_0 . The magnetic field at the nucleus is therefore generally less than the applied field by a fraction σ given by:

$$\mathbf{B}_{eff} = \mathbf{B}_0(1 - \sigma), \quad (5.33)$$

where σ , the nuclear magnetic shielding, is expressed in part per million (ppm). Therefore the resonance condition becomes

$$\nu_0 = \gamma \mathbf{B}_0(1 - \sigma) / 2\pi \quad (5.34)$$

The chemical shift position in a spectrum δ is commonly measured relative to a standard substance, such as liquid tetramethylsilane (TMS), defined as

$$\delta \text{ (ppm)} \equiv \frac{\nu - \nu_{Ref}}{\nu_{Ref}} 10^6, \quad (5.35)$$

where ν is the resonance frequency of the measured nucleus and ν_{Ref} the frequency of the reference substance.

Because the electron distribution is not spherical, the chemical shift interaction depends on the orientation of the molecules with respect to the direction of \mathbf{B}_0 , i.e. the z direction. The anisotropy of the shift causes a broadening of the signal in the solid state, but disappears in solutions where the rapid, random molecular motions average out the anisotropy, leaving an isotropic value of the shielding. This shift is described by a Hamiltonian of the following form

$$\hat{H}_{CS} = \gamma \hbar \mathbf{I} \cdot \hat{\boldsymbol{\sigma}} \cdot \mathbf{B}_0 \quad (5.36)$$

where $\hat{\boldsymbol{\sigma}}$ is the chemical shielding tensor. The tensor $\hat{\boldsymbol{\sigma}}$ describes the effect of the electron distribution about the nuclear spin. It can be represented in a Cartesian space by a 3×3 matrix defined by six independent elements:

$$\hat{\boldsymbol{\sigma}} = \begin{pmatrix} \sigma_{xx} & \sigma_{xy} & \sigma_{xz} \\ \sigma_{yx} & \sigma_{yy} & \sigma_{yz} \\ \sigma_{zx} & \sigma_{zy} & \sigma_{zz} \end{pmatrix} \quad (5.37)$$

Under the influence of the external field \mathbf{B}_0 which points along z direction, equation (5.36) develops as:

$$\begin{aligned}\hat{H}_{CS} &= \gamma \hbar (I_x, I_y, I_z) \begin{pmatrix} \sigma_{xx} & \sigma_{xy} & \sigma_{xz} \\ \sigma_{yx} & \sigma_{yy} & \sigma_{yz} \\ \sigma_{zx} & \sigma_{zy} & \sigma_{zz} \end{pmatrix} \begin{pmatrix} 0 \\ 0 \\ B_0 \end{pmatrix} \\ &= \gamma \hbar B_0 (\sigma_{xz} I_x + \sigma_{yz} I_y + \sigma_{zz} I_z)\end{aligned}\tag{5.38}$$

Since only the I_z term commutes with the Zeeman Hamiltonian, in first order the chemical shift Hamiltonian reduces to:

$$\hat{H}_{CS} = \gamma \hbar I_z \sigma_{zz} B_0\tag{5.39}$$

Equation (5.39) reflects the fact that the chemical shift interaction scales linearly with the external magnetic field \mathbf{B}_0 , and that it depends on the zz component of the shielding tensor. σ_{zz} does not have a fixed value but depends on the orientation of the molecule with respect to the magnetic field.

The NMR interaction tensor can also be written with respect to the Cartesian axis system of the molecule. These tensors can be diagonalized to yield tensors which describe the interaction in its own Principal Axis System (PAS, see figure 5.15)

$$\hat{\sigma} = \begin{pmatrix} \sigma_{11}^{PAS} & 0 & 0 \\ 0 & \sigma_{22}^{PAS} & 0 \\ 0 & 0 & \sigma_{33}^{PAS} \end{pmatrix}\tag{5.40},$$

where the three elements on the diagonal, σ_{11}^{PAS} , σ_{22}^{PAS} and σ_{33}^{PAS} , are called the ‘‘principal components’’ along three mutually orthogonal coordinates in the molecule and will characterize completely the shielding of a particular nucleus. The normal convention is to take

$$\sigma_{11}^{PAS} \leq \sigma_{22}^{PAS} \leq \sigma_{33}^{PAS}\tag{5.41}.$$

The principal component σ_{11}^{PAS} corresponds to the direction of the least shielding, with the highest frequency, while σ_{33}^{PAS} corresponds to the direction of the highest shielding of the chemical shift tensor. For a linear molecule only two of the three principal components are independent. The electronic circulation induced in such a molecule will be different if it is perpendicular or parallel

to the magnetic field. Thus in that case there are two independent quantities, σ_{\perp} and σ_{\parallel} , which characterize the nuclear shielding. The isotropic value of the shielding, σ_{iso}^{PAS} , is the average of the three principal components, and corresponds to the center of the line shape. In solutions, only the isotropic average is observed:

$$\sigma_{iso} = \frac{1}{3}(\sigma_{11}^{PAS} + \sigma_{22}^{PAS} + \sigma_{33}^{PAS}) \quad (5.42)$$

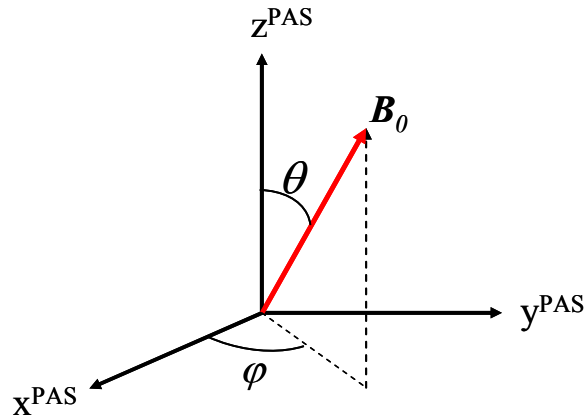


Figure (5.15): Schematic representation of \mathbf{B}_0 field in PAS. Its orientation is defined by polar angles θ and φ .

σ_{zz} of equation (5.39) can be expressed in σ_{11} , σ_{22} and σ_{33} by:

$$\sigma_{zz} = (\sigma_{11}^{PAS} (\cos \varphi \sin \theta)^2 + \sigma_{22}^{PAS} (\sin \varphi \sin \theta)^2 + \sigma_{33}^{PAS} (\cos \theta)^2) \quad (5.42a)$$

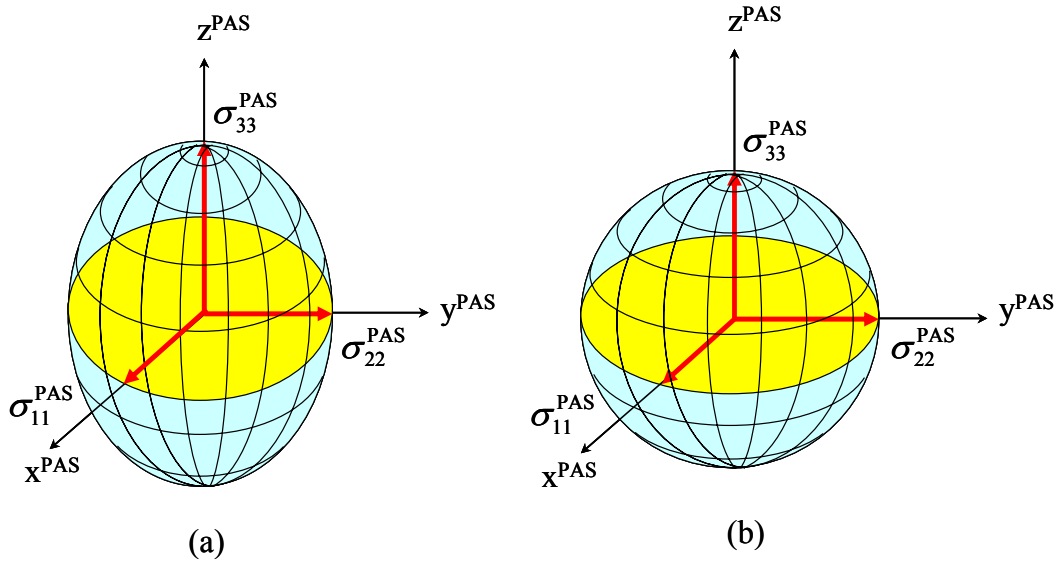


Figure (5.16): Schematic representations of the chemical shift in the principal axis system PAS **(a)** as an ellipsoid where $\sigma_{11}^{PAS} = \sigma_{22}^{PAS} \neq \sigma_{33}^{PAS}$ (axial symmetry) and **(b)** as a spherical shape for the isotropic case where $\sigma_{11}^{PAS} = \sigma_{22}^{PAS} = \sigma_{33}^{PAS}$ (spherical symmetry).

The chemical shift resonance frequency can then be written as [26]

$$\omega_{CS}(\varphi, \theta) = \gamma \hbar B_0 \sigma_{zz} = \gamma \hbar B_0 \left[\sigma_{11}^{PAS} (\cos \varphi \sin \theta)^2 + \sigma_{22}^{PAS} (\sin \varphi \sin \theta)^2 + \sigma_{33}^{PAS} (\cos \theta)^2 \right] \quad (5.43)$$

Equation (5.43) shows that when all possible orientations of the principal axes with respect to the external magnetic field are sampled this results in a broad line with a typical powder pattern.

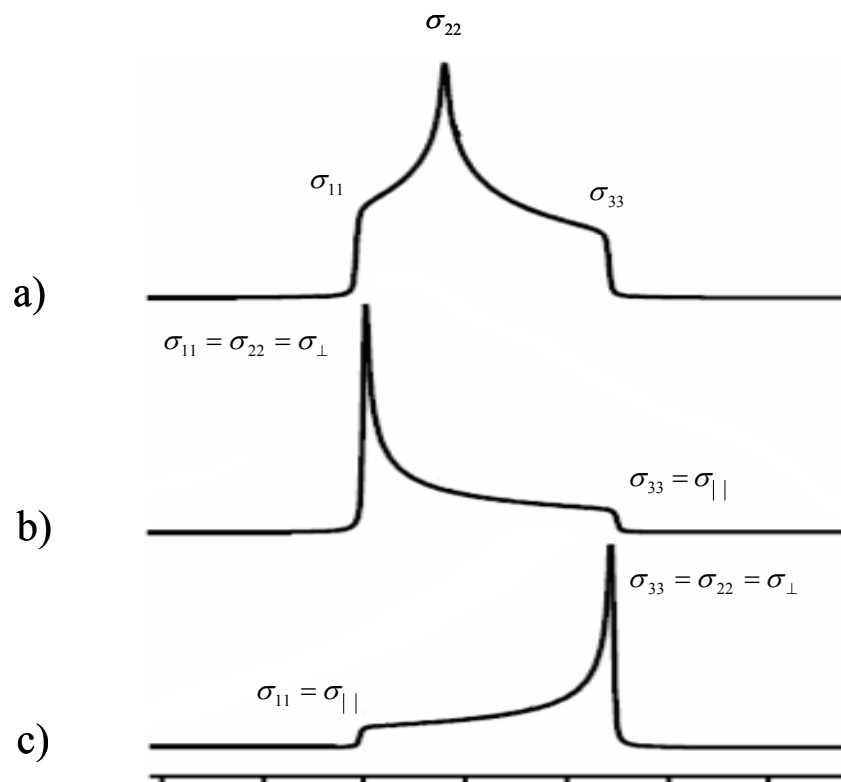


Figure (5.17): Schematic representation of the typical powder patterns for various chemical shift tensors (a) Asymmetrical pattern for $\sigma_{11} \neq \sigma_{22} \neq \sigma_{33}$; (b) Powder spectrum for a chemical shift tensor with axial symmetry, where $\sigma_{11} = \sigma_{22} = \sigma_{\perp}$; (c) Powder spectrum for chemical shift tensor with axial symmetry, where $\sigma_{33} = \sigma_{22} = \sigma_{\perp}$.

Much of the chemical information in solid state NMR spectra arises from the chemical shift. It yields a variety of possible NMR shapes. Molecular motions can narrow the chemical shift powder pattern, by averaging, and the resulting powder spectra will contain useful dynamic information about the molecules under study. In a fluid, the rapid motion of the molecule averages the shielding tensor to its isotropic value σ_{iso} .

The chemical shift tensor powder pattern contributes significantly to the line broadening of a solid state NMR spectrum, which often obscures the structural information available from the isotropic chemical shifts. This line broadening of the resonances in the solid state can be eliminated by spinning the sample about an axis oriented at an angle called the magic angle with respect to the external field (see later). Thus, magic angle spinning (MAS) averages the anisotropic part of the

chemical shift anisotropy to its isotropic average.

5.3.1.2 The Dipolar Interaction [23-26]

The dipolar coupling arises from the space interaction between the nuclear magnetic moments of two nuclei, which we will assign by i and j . The magnitude of the dipolar coupling depends on the distance between the two spins and the angle between the internuclear axis with respect to the applied field. The magnetic field of a nuclear spin i affects the local magnetic field of its neighbor j , resulting in an increase or decrease of the local magnetic field \mathbf{B}_{loc} at both nuclei.

$$\mathbf{B}_{loc} = \frac{\boldsymbol{\mu}_i}{r^3} (3 \cos^2 \theta_{ij} - 1), \quad (5.44)$$

where $\boldsymbol{\mu}_i$ is the magnetic moment of nucleus i and r is the internuclear distance. The angle θ describes the orientation of the internuclear vector with respect to the direction of the external magnetic field (figure 5.18). Classically, the energy of interaction between two magnetic dipoles $\boldsymbol{\mu}_i$ and $\boldsymbol{\mu}_j$ is given by the following equation which represents the full dipolar Hamiltonian:

$$U = \frac{\mu_0}{4\pi} \left(\frac{\boldsymbol{\mu}_i \cdot \boldsymbol{\mu}_j}{r^3} - 3 \frac{(\boldsymbol{\mu}_i \cdot \mathbf{r})(\boldsymbol{\mu}_j \cdot \mathbf{r})}{r^5} \right) \quad (5.45)$$

The appropriate quantum mechanical expression is obtained by substituting $\boldsymbol{\mu} = \gamma \hbar \mathbf{I}$ in equation (5.45), then we get

$$\hat{H}_D = \frac{\mu_0 \gamma_i \gamma_j \hbar}{4\pi} \left(\frac{\mathbf{I}_i \cdot \mathbf{I}_j}{r^3} - 3 \frac{(\mathbf{I}_i \cdot \mathbf{r})(\mathbf{I}_j \cdot \mathbf{r})}{r^5} \right) \quad (5.46)$$

Here γ_i and γ_j are the gyromagnetic ratios of spins i and j , μ_0 is the permeability of free space,

$d = \frac{\mu_0 \gamma_i \gamma_j \hbar}{4\pi r^3}$ is the dipolar constant (in units of rad s^{-1}) and r is the internuclear distance.

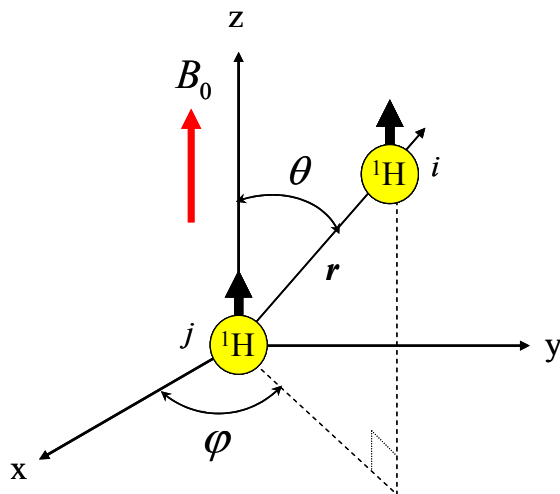


Figure (5.18): The polar angles θ and φ specifying the coupled spin pair in a magnetic field \mathbf{B}_0 .

In a Cartesian coordinate system x, y, z the dipolar Hamiltonian between two nuclei can be written as

$$\hat{H}_D = d \begin{bmatrix} I_{xi}, I_{yi}, I_{zi} \\ \left[\begin{array}{ccc} 1 - 3x^2/r^2 & -3xy/r^2 & -3xz/r^2 \\ -3xy/r^2 & 1 - 3x^2/r^2 & 1 - 3yz/r^2 \\ -3xz/r^2 & -3yz/r^2 & 1 - 3z^2/r^2 \end{array} \right] \end{bmatrix} \begin{bmatrix} I_{xj} \\ I_{yj} \\ I_{zj} \end{bmatrix} \quad (5.47)$$

$$= \mathbf{I}_i \cdot \hat{\mathbf{D}} \cdot \mathbf{I}_j \quad (5.48)$$

$\hat{\mathbf{D}}$ is known as the dipolar coupling tensor, which is an axially symmetric and traceless tensor ($\text{Tr} [\hat{\mathbf{D}}] = 0$), for this reason the dipolar coupling in a liquid is averaged to zero.

By transforming the expression of the vector \mathbf{r}_{ij} to spherical polar coordinates (r, θ, φ) , $\mathbf{r} = (r_x, r_y, r_z) = (r \sin \theta \cos \varphi, r \sin \theta \sin \varphi, r \cos \theta)$ where z is chosen as the polarization axis and by expressing \hat{I}_x and \hat{I}_y in terms of raising and lowering operators which are defined as

$$\hat{I}_+ = \hat{I}_x + i\hat{I}_y \text{ (here } i = \sqrt{-1}) \text{ and } \hat{I}_- = \hat{I}_x - i\hat{I}_y, \text{ such that } \hat{I}_x = \frac{1}{2}(\hat{I}_+ + \hat{I}_-), \hat{I}_y = -\frac{i}{2}(\hat{I}_+ - \hat{I}_-),$$

equation (5.47) can be rewritten in terms of polar coordinates. After some considerable rearrangements we get a convenient “*dipolar alphabet*”:

$$\hat{H}_D = \frac{\mu_0}{4\pi} \frac{\gamma_i \gamma_j \hbar}{r^3} [\hat{A} + \hat{B} + \hat{C} + \hat{D} + \hat{E} + \hat{F}] \quad (5.49)$$

$$\begin{aligned} \hat{A} &= (1 - 3 \cos^2 \theta) \hat{I}_{iz} \hat{I}_{jz} \\ \hat{B} &= -\frac{1}{4} (1 - 3 \cos^2 \theta) [\hat{I}_{i+} \hat{I}_{j-} + \hat{I}_{i-} \hat{I}_{j+}] \\ \hat{C} &= -\frac{3}{2} \sin \theta \cos \theta e^{-i\phi} [\hat{I}_{iz} \hat{I}_{j+} + \hat{I}_{i+} \hat{I}_{jz}] \\ \hat{D} &= -\frac{3}{2} \sin \theta \cos \theta e^{i\phi} [\hat{I}_{iz} \hat{I}_{j-} + \hat{I}_{i-} \hat{I}_{jz}] \end{aligned}$$

where

$$\begin{aligned} \hat{E} &= -\frac{3}{4} \sin^2 \theta e^{-i2\phi} [\hat{I}_{i+} \hat{I}_{j+}] \\ \hat{F} &= -\frac{3}{4} \sin^2 \theta e^{i2\phi} [\hat{I}_{i-} \hat{I}_{j-}] \end{aligned} \quad (5.50)$$

In the case of homonuclear coupling or like spins, the A and B terms commute with the \hat{I}_z operator of the Zeeman interaction. \hat{A} and \hat{B} form the secular part of the Hamiltonian. The line shape due to dipolar coupling is then governed by the A and B terms. Only the terms A and B lead to broadening and shifting of NMR resonance lines, therefore, they will be taken into account. In the case of unlike spins only the term A commutes with the \hat{I}_z operator of the Zeeman term. The remaining terms of the dipolar Hamiltonian B, C, D, E and F then form the non-secular part. In first order they do not affect the broadening and the shifting of NMR resonance lines.

Thus the homonuclear dipolar Hamiltonian may be truncated to

$$\hat{H}_D = -\left(\frac{\mu_0}{4\pi}\right) \frac{\hbar \gamma^2}{r^3} (3 \cos^2 \theta_{ij} - 1) \left[\hat{I}_{iz} \hat{I}_{jz} - \frac{1}{2} (\hat{I}_{i+} \hat{I}_{j-} + \hat{I}_{i-} \hat{I}_{j+}) \right] \quad (5.51)$$

The equation (5.51) is often written more succinctly as

$$\hat{H}_D = -d (3 \cos^2 \theta_{ij} - 1) \left[3 \hat{I}_{iz} \hat{I}_{jz} - (\hat{I}_{i+} \hat{I}_{j-}) \right] \quad (5.52)$$

where we have used the fact that $\hat{\mathbf{I}}_i \cdot \hat{\mathbf{I}}_j = \hat{I}_{ix} \hat{I}_{jx} + \hat{I}_{iy} \hat{I}_{jy} + \hat{I}_{iz} \hat{I}_{jz}$, $\hat{I}_+ = \hat{I}_x + i\hat{I}_y$ and $\hat{I}_- = \hat{I}_x - i\hat{I}_y$; $(3 \cos^2 \theta_{ij} - 1)$ denotes the orientational part of the Hamiltonian. The first part $\hat{I}_{iz} \hat{I}_{jz}$ in equation (5.52) describes the interaction of one spin with the z-component of the local field produced by the other spin. In a powder, where the crystallites are oriented in all possible directions, each spin feels a superposition of many local magnetic fields due to the coupling to many neighbors, and each local field gives a contribution to the resonance frequency of the observed spin. Since the size and direction of the local field varies from spin to spin due to the distance and angle dependence, the dipolar coupling can lead to very broad lines up to 70 kHz for protons.

The second part in equation (5.51) ($\hat{I}_{i+} \hat{I}_{j-} + \hat{I}_{i-} \hat{I}_{j+}$) is called the “flip-flop term” which is responsible for the polarization exchange between two like spins i and j .

For a heteronuclear interaction, only the term A commutes with the \hat{I}_z operator of the Zeeman Hamiltonian, the flip-flop term can be neglected. Then the Hamiltonian can be reduced to

$$\hat{H}_{D,ij} = \frac{\mu_0}{4\pi} \frac{\gamma_i \gamma_j \hbar}{r^3} (3 \cos^2 \theta_{ij} - 1) \hat{I}_{iz} \hat{I}_{jz} \quad (5.53)$$

In general, motion reduces the dipolar couplings. The rapid reorientation of a molecule in liquids on a timescale much faster than the dipolar coupling evolves, causes the $(1 - 3 \cos^2 \theta)$ term of the dipolar coupling Hamiltonian to average to zero. However, in a solid comprised of randomly oriented crystallites, the direction of the internuclear vectors remains fixed and the frequency shift produced by each crystallite will depend on its orientation with respect to the external field. The degree of mobility of the molecules can be extracted from the dipole-broadened spectra. This effect will be explained in more detail in the next section when the magic angle spinning is discussed.

5.3.2 Magic Angle Spinning [27-30]

Magic angle spinning (MAS) is one of the most striking techniques of solid state nuclear magnetic resonance. It is used to average out the effects of anisotropic interactions that can be described by a second-rank tensor and in this way, to enhance the resolution of NMR spectra of solids.

5.3.2.1 Magic Angle Spinning and Line Broadening

This technique focuses on the geometric part of the Hamiltonian, namely the term $(3 \cos^2 \theta - 1)$. It describes how the interaction tensor fixed in a molecule within the sample, varies with time as the molecule rotates with the sample. In order to see what effect the orientation has on a local field, we have to go back to equation (5.44)

$$\mathbf{B}_{loc} = \frac{\mu_i}{r^3} (3 \cos^2 \theta_{ij} - 1) \quad (5.54)$$

From the above equation (5.54), it is clear that only at one particular angle, the local magnetic field \mathbf{B}_{loc} will vanish. This is the angle for which $(3 \cos^2 \theta - 1)$ is zero or $\theta = 54.7^\circ$, the magic angle.

With the magic angle spinning technique the sample is packed in a rotor that rotates around an axis which makes the magic angle with the static magnetic field \mathbf{B}_0 (figure. 5.19). Then the angle each internuclear vector r_{ij} makes with the magnetic field becomes time-dependent, but the average value for all internuclear orientations becomes equal to 54.7° , the magic angle. The average value of all dipolar interactions is therefore also zero and in principle the broadening by the dipolar interactions is eliminated. The time-dependence of the dipolar interaction caused by the magic angle spinning causes the appearance of spinning sidebands.

Figure (5.19) illustrates a rotor spinning along the magic angle spinning. Although the vectors between nuclei 1 and 2 are at a different angle to the field than for nuclei 3 and 4, spinning causes the time-averaged direction of these internuclear vectors to lie along the spinning axis.

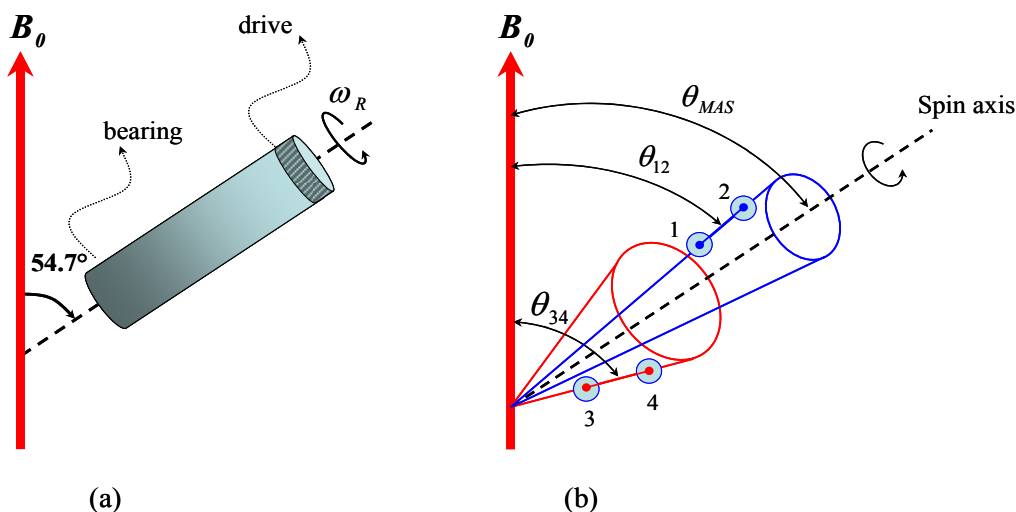


Figure (5.19): The magic angle spinning technique.

When spinning the sample with a rotation frequency ω_R sidebands appear in the spectrum. The sidebands in MAS are spaced at exact multiples of the spinning speed of the rotor $n\omega_R$ ($n = \pm 1, \pm 2, \pm 3, \dots$) away from the isotropic or central line. The intensities of spinning sidebands become negligibly weak when $\omega_R \gg$ dipolar width $\Delta\omega_d$. The total intensity is then found in the central band (figure 5.20).

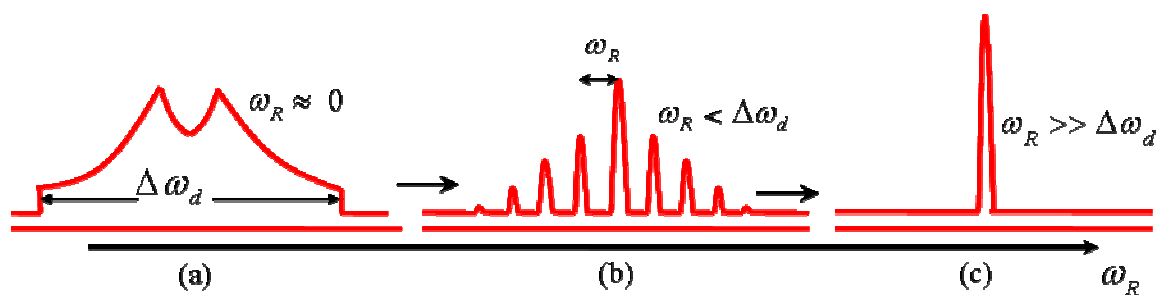


Figure (5.20): The change of a dipolar powder pattern under MAS conditions and the dependence on the spinning rate.

5.4 Types of Line Broadening [4, 27-29]

The width of an NMR line is defined as the full width at half height (FWHM) of the resonance line and is a factor affecting the resolution of the NMR spectra. Interactions like the spin-spin dipolar couplings and the anisotropic chemical shift broaden the resonance lines of a solid sample and hinder the spectral resolution. To obtain highly resolved spectra of solids it is necessary to

reduce the line broadening as efficiently as possible. As described above one of the line narrowing techniques is MAS. There are several factors contributing to the remaining linewidth. In principle, line-broadening effects can be divided into two parts: inhomogeneous broadening as CSA, dipole-dipole interactions of unlike spins, and homogeneous broadening as dipole-dipole interactions between like spins. Important particularly in this work is the proton dipolar coupling $^1\text{H}-^1\text{H}$.

In principle every broadened line can be represented by a superposition of many narrow peaks (line width $\delta\omega$), often called spin packets, each with a slightly different frequency $\omega_0 \pm \omega_1, \omega_0 \pm \omega_2, \omega_0 \pm \omega_3$, etc., as represented in figure (5.21 a). Different spin packets have different resonance frequencies due to the dipolar and chemical shift interactions. The difference between inhomogeneous and homogeneous line broadening lies in how long individual spin packets keep their resonance frequency. For inhomogeneous broadening each spin packet keeps its resonance frequency practically forever, because it is, for instance, determined by the orientation of the crystallite in which the spins of the spin packet are located. In a homogeneously broadened line individual spin packets continuously exchange their resonance frequency. The most important reason for that is that for like spins the B term of the dipolar interaction causes spin flip-flops. In a proton dipolar coupled network the flip-flops cause that a particular spin never keeps the same resonance frequency. The spin moves, with a rate determined by the dipolar B term, through the line, making the line homogeneous (figure. 5.21(b))



Figure (5.21): (a) An inhomogeneous broadening and (b) a homogeneous broadening.

The distinction between homogeneous (line width $\Delta\omega$) and inhomogeneous lines (total line width $\Delta\omega$, line width of the spin packets $\delta\omega$) is very important for the application of magic angle

spinning. For an inhomogeneous line MAS starts to narrow the line already for spinning rates larger than $\delta\omega$ but smaller than $\Delta\omega$. This is shown in figure 5.22 b) for the ^{13}C line of $(\text{cp})_2\text{ZrCl}_2$ which is broadened by the chemical shift anisotropy. The inhomogeneously broadened line splits up in spinning sidebands at spinning rates far below the total line width.

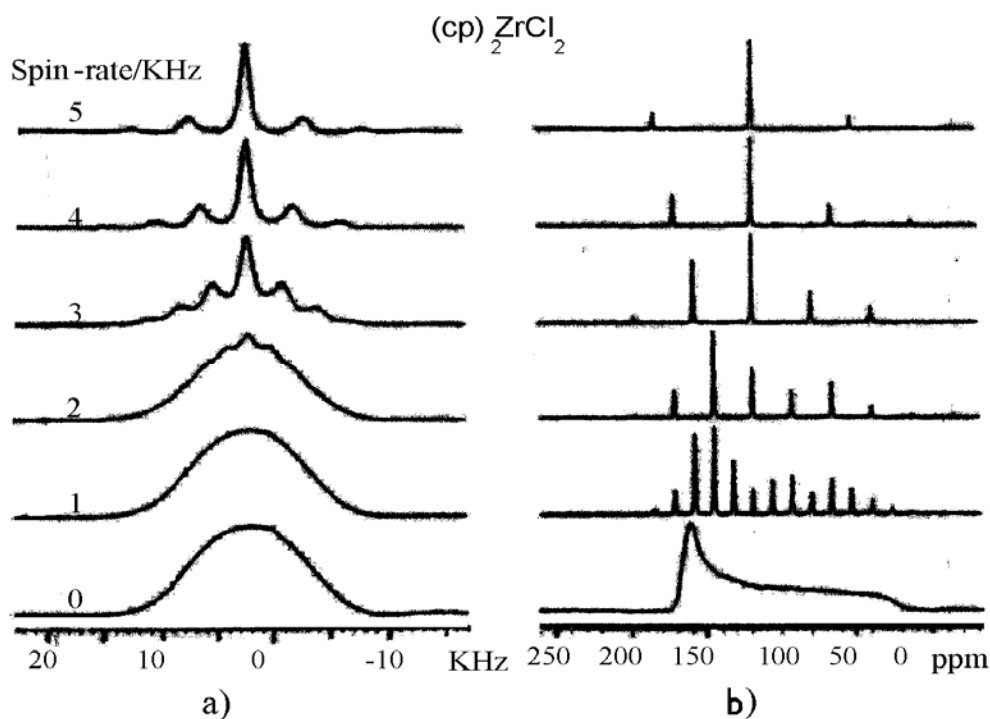


Figure (5.22): The effect of MAS on: (a) Proton spectra of homogeneous lineshape $(\text{cp})_2\text{ZrCl}_2$, (b) ^{13}C spectra of the same substance (R. K. Harris, summer school report).

The opposite situation is found for the proton spectrum of the same compound. Due to the B term of the dipolar interaction this line is homogeneously broadened and spinning sidebands only appear at much higher spinning rates. The spinning rate has to be larger than the dipolar B term.

A similar situation is found in fig. 5.23 for the proton spectrum of adamantane. Special here is that the adamantane molecules form a so called plastic crystal in which the molecules at room temperature rotate on their crystal sites. This decreases the size of the proton B term and therefore the proton line with an overall width of 13.7 kHz starts to narrow by MAS already at a spinning frequency of ca. 3 kHz.

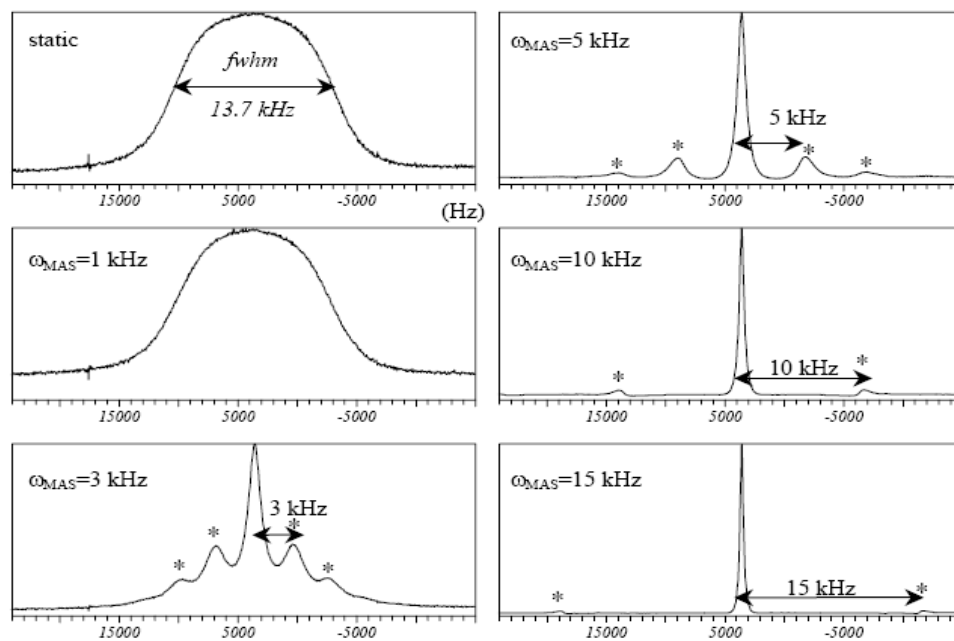


Figure (5.23): Influence of the MAS spinning speed on the ^1H -NMR spectrum of adamantane, at room temperature and for a ^1H frequency of 300.13 MHz; spinning sidebands are marked with * [30].

5.5 References to Chapter Five

- [1] E. M. Purcell, H. C. Torrey, R. V. Pound. *Phys. Rev.* **1946**, 69, 37.
- [2] F. Bloch, W. W. Hansen, M. Packard, *Phys. Rev.* **1946**, 69, 127.
- [3] R. Ernst, G. Bodenhausen, A. Wokaun, “*Principles of Nuclear Magnetic Resonance in One and Two Dimensions*”, Oxford University Press, **1990**.
- [4] M. H. Levitt. Spin Dynamics: “*Basics Principles of Nuclear Magnetic Resonance*”, Wiley, Chichester, England, **2001**.
- [5] W. G. Proctor, F. C. Yu, *Phys. Rev.* **1950**, 77, 717.
- [6] W. C. Dickinson. *Phys. Rev.* **1950**, 77, 736.
- [7] A. M. Kantola, G. R. Luckhurst, B. A. Timimi, A. Sugimura. *Mol. Cryst. Liq. Cryst.* **2003**, 402, 117.
- [8] J. Li, D. Geschke, R. Stannarius. *Liquid Crystals*, **2004**, 31(1), 21.
- [9] J. Guzman, B. C. Gates. *Dalton Trans.* **2003**, 3303.
- [10] S. Faggian, P. Fisticaro, E. Giamello, R. Gobetto, A. Viale, G. Berlier, C. Lamberti, I. Rossetti. *J. Phys. Chem. B*, **2003**, 107, 8922.
- [11] S. A. Bagshaw, S. Jaenicke, C. G. Khuan. *Ind. Eng. Chem. Res.* **2003**, 42, 3989.
- [12] M. Duer. “*Solid-State NMR Spectroscopy, Principles and Applications*”, M. Duer. Blackwell Science Ltd, **2002**.
- [13] E. R. Andrew, A. Bradbury, R. G. Eades, *Nature* **1959**, 183, 1802.
- [14] I. J. Lowe. *Phys. Rev. Lett.* **1959**, 2(7), 285.
- [15] E. O Stejskal, J. Schaefer, J. S. Waugh, *J. Magn. Reson.* **1977**, 28, 105.
- [16] A. Pines, M. G. Gibby, J. S Waugh, *J. Chem. Phys.* **1973**, 59, 569.
- [17] D. D. Laws, H.-M. L. Bitter, A. Jerschow. *Angew. Chem. Int. Ed.* **2002**, 41, 3096.
- [18] A. Fersht. “*Structure and Mechanisms in Protein Science*”, W. H. Freeman & Company, New York, **1998**.
- [19] W. S. Veeman *Phil. Trans. R. Soc. Lond.*, **1981**, A299, 629.
- [20] W. Massa, “*Crystal Structure Determination*” Springer-Verlag, Berlin, **1991**.
- [21] M. Philippopoulos, A. Mandel, Palmer III, A. G. & Lim, C. *Proteins: Struct. Funct. Genetics.* **1997**, 28: 481.
- [22] D. Canet, “*Nuclear magnetic resonance, Concepts and methods*”. Chichester, Wiley, **1996**.

- [23] M. Mehring, Homogenous, inhomogeneous and heterogeneous lineshapes, In *Principles of High Resolution NMR in Solids*, 303, 2nd ed.; Springer-Verlag: Berlin, **1983**.
- [24] A. Abragam, Dipolar line width in a rigid lattice, In *The Principles of Nuclear Magnetism*, 97, 1st ed.; Oxford University Press: Oxford, UK, **1961**.
- [25] Abragam, A.; Theory of line width in the presence of motion of the spins, In *The Principles of Nuclear Magnetism*, 424, 1st ed.; Oxford University Press: Oxford, **1961**.
- [26] M. Mehring, "*Principles of High Resolution NMR in Solids*", Springer-Verlag. Berlin, 2nd edition, **1983**.
- [27] K. Schmidt-Rohr, H. W. Spiess, "*Multidimensional Solid-State NMR and Polymers*", Academic Press, London, **1994**.
- [28] C. P. Slichter, "*Principles of Magnetic Resonance*", Springer, Berlin, **1990**.
- [29] B. Crowan, "*Nuclear Magnetic Resonance and relaxation*", Cambridge University press, Cambridge, **1997**.
- [30] K. Saalwächter, Dissertation am Fachbereich Chemie und Pharmazie in Mainz, **2000**

The Nuclear Magnetic Resonance Techniques

Nuclear Magnetic Resonance Technique

The ^1H NMR experiments were carried out on three spectrometers: a Bruker Avance 400 MHz, Bruker ASX 400 MHz, both with static magnetic field strength of 9.4 Tesla, and Bruker MSL 200 MHz with static magnetic field of 4.7 Tesla. All spectrometers are equipped with high resolution magic angle spinning (HR MAS) probe heads and 4 mm zirconia rotors with Kel-F cap. The temperature range is 220-298K. The temperature was controlled by using a variable temperature unit (Bruker BVT 3000 Digital) with temperature stability of about 0.4 K. The temperature was calibrated according to the temperature dependence of the isotropic chemical shift of pure methanol. One-dimensional (1D) spectra were measured by using a single pulse excitation with pulse length $1\ \mu\text{s}$ (figure 6.1), corresponding to a flip angle much smaller than 90° . Signal acquisition involved 500 scans with 2s recycle delay. The proton chemical shift is referenced with respect to tetramethylsilane (TMS) at 0 ppm. It was found that the spectra depend only on the water weight fraction, regardless of whether the dry sample is exposed to water vapor in a sealed environment or when just the equivalent amount of liquid water is added to the sample. Therefore, all the experiments were performed with adding known amounts of water to the rotor filled with the dry sample. Before each loading of water the samples were dehydrated by putting the sample in an oven at $160\ \text{C}^\circ$. Water inside the rotor is easily loaded by using a syringe or a small pipette and care must be taken, that the cap is properly positioned.

In order for the rotor to spin stable and fast, it has to be well balanced. It is very difficult to spin the rotor filled with single-walled carbon nanotubes. The best procedure is to first fill the rotor with a small amount of sample and tap it lightly on a hard surface so that the sample is packed against the walls of the barrel and then more samples can be added to the rotor.

The precise setting of the magic angle is mandatory to obtain the maximum spectral resolution obtained by MAS. In order to adjust the magic angle, a sample of KBr (^{79}Br observe) is used.

Due to the quadrupole spin of the ^{79}Br ($I=3/2$), the resonance shows many spinning sidebands and the setting of the magic angle is very accurate.

The ^1H single pulse excitation is the simplest NMR experiment. Its pulse scheme is shown in Figure (6.1).

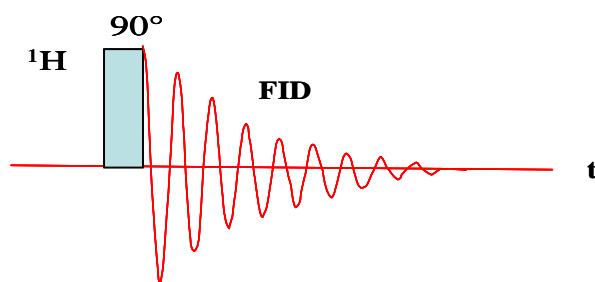


Figure (6.1): Pulse scheme of ^1H single pulse excitation.

It should be noted that the timescale can not be represented correctly in the pulse schemes shown here since the pulse durations are of the order of a few μs , while the delays between pulses are of the order of μs to ms , and the FID is of the order of several ms .

At equilibrium, the nuclear magnetization is along the main magnetic field B_0 axis. The 90° pulse, applied through an orthogonal magnetic field B_1 rotates it into the orthogonal xy plane. The detection of the magnetization is immediately done in the xy -plane, leading to the free induction decay (FID), and to the spectrum after Fourier transformation.

Chapter Seven: Results and Discussion

7. Introduction

^{13}C NMR clearly is the NMR technique of first choice to study single-wall carbon nanotubes. So far two groups have reported successful experiments (Goze Bac et al. [1] and Tang et al [2]). Both report MAS experiments, providing a carbon isotropic chemical shift at 126 ppm, typical for a sp^2 carbon, and from static experiments the chemical shift principal elements $\delta_{11}=240$ ppm, $\delta_{22}=171$ ppm and $\delta_{33}=-36$ ppm. They also found two spin-lattice relaxation times T_1 , a short one for metallic tubes and a long one for the semiconducting nanotubes. We tried to reproduce these results but in our samples (Fe catalyst) we could not detect any significant carbon NMR signal. Probably our samples still contained a too high concentration of Fe magnetic clusters. Also the reported experiments were performed on SWCNT with 10 % ^{13}C and 90 % enriched SWCNT with Ni/Y and Pt-Rh-Re catalysts, respectively.

The study of water in SWCNTs has been more popular. Mao et al. [3] used ^1H NMR to measure water adsorption in SWCNT and activated carbon at room temperature. They concentrated especially on the NMR lineshape at temperatures where the absorbed water is rigid.

Ghosh et al. [4] have carried out NMR investigations on water absorbed in SWCNT (arc discharge with Ni- Y_2O_3 catalyst, radius of the tube is 0.71 nm) as a function of temperature from 210 K to 300 K. In their experiments the NMR line shape at and below the freezing point of bulk water is composed of two components, the intensities of both components decrease with lowering the temperature below 273 K. One component (L_1), (left in the spectrum, see figure (7.1) vanishes below ~ 242 K and the other (L_2) component disappears below ~ 237 K. The authors claim that both components represent water inside the tube; the first component is due to water molecules at the center of the tube, the second component is associated with the water molecules at a distance of 0.3 nm from the wall of the tube. The disappearance of L_1 below ~ 237 K was interpreted as the transfer of the central water to the water-tube (L_2) which subsequently freezes at ~ 212 K [4]. The water mobility at room temperature is very high;

therefore, we cannot distinguish two positions of water molecule inside the tube, thus we have observed in our work only one signal attributed to water molecules inside the tube.

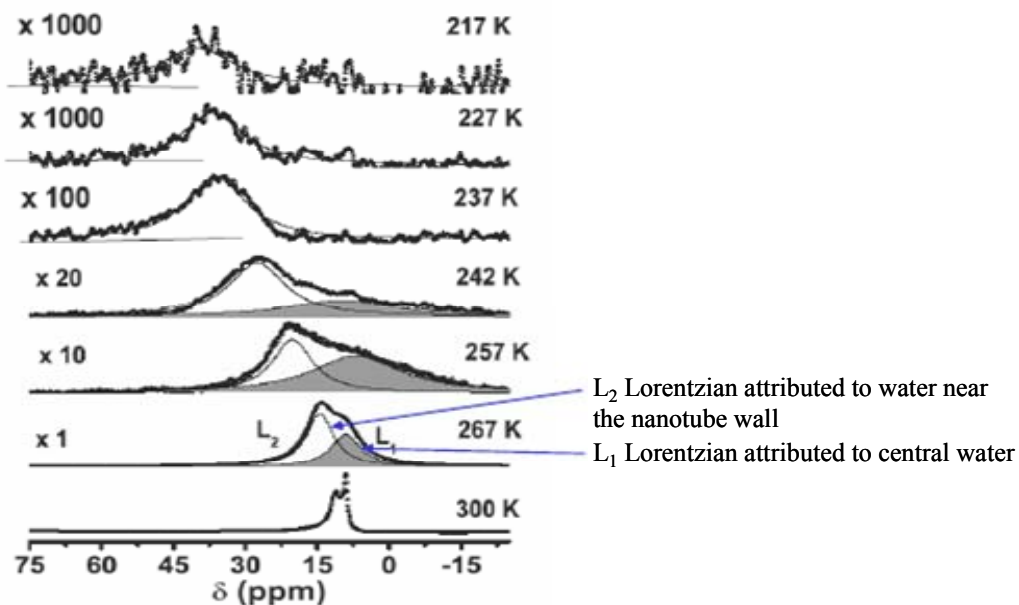


Figure (7.1): Temperature dependence of NMR spectra obtained by Ghosh et al. [4]

The NMR study of water absorbed in single-wall carbon nanotubes (SWCNTs) reported in this thesis differs from the other investigations in that here other tube diameters and catalysts are used to produce the SWCNT. In addition magic angle spinning is applied in order to increase the spectral resolution.

7.1 Experimental Results and Discussion

In chapter four we showed that for the production of carbon nanotubes magnetic catalysts are needed. In the magnetic field we use for the NMR experiment the unpaired electrons of these magnetic impurities generate a strong local magnetic field, whose direction and magnitude depends on the distance and relative orientation of the magnetic clusters with respect to the observed nuclear spins. The local field is caused by nuclear-electron dipolar interactions, similar as described in chapter 6 for nuclear spin-nuclear spin interactions. Although at beforehand we do not know if the nuclear-electron dipolar interaction leads to homogeneously or inhomogeneously broadened NMR lines, we do expect that the lower the concentration of the magnetic impurities the larger the average nuclear spin – unpaired electron spin distance will be and the smaller the dipolar interaction.

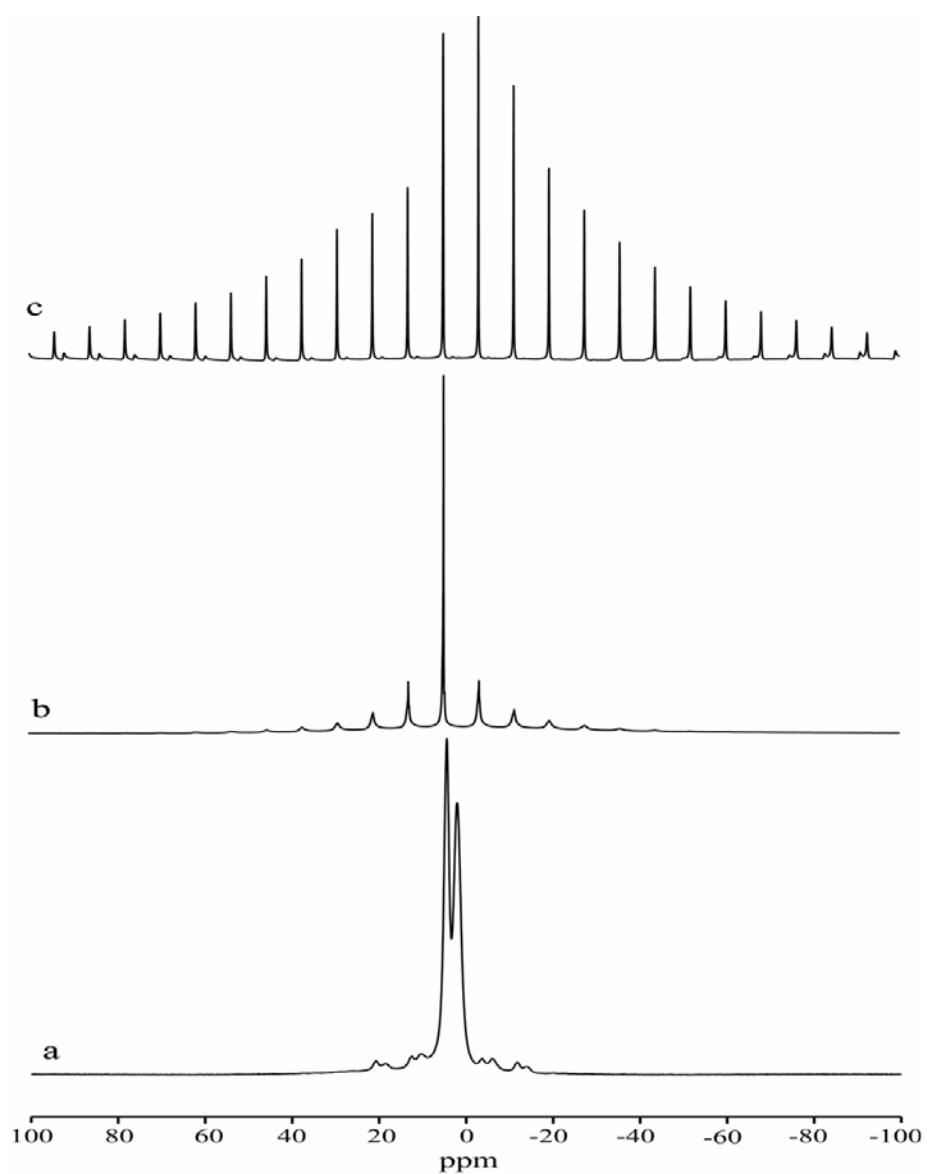


Figure (7.2): ^1H MAS-NMR spectra of SWCNT loaded with about 250 wt % water as a function of Fe impurity concentration (a) 5.9 wt %, (b) 13 wt % and (c) 20 wt %

Figure (7.2) shows the effect of the Fe impurity concentration on the ^1H MAS-NMR spectra of 250 wt% water absorbed in SWCNT at room temperature. The spectra show that at an impurity level of 20 wt% Fe the magnetic Fe nanoparticle clusters cause a strong broadening of the water NMR resonance line of circa 100 ppm (corresponding to 40 kHz), which is broken up into spinning sidebands by magic angle spinning. As expected, at lower metal impurity levels the

broadening significantly decreases until at a level of 5.9 wt% the broadening by magnetic clusters seems to have practically disappeared.

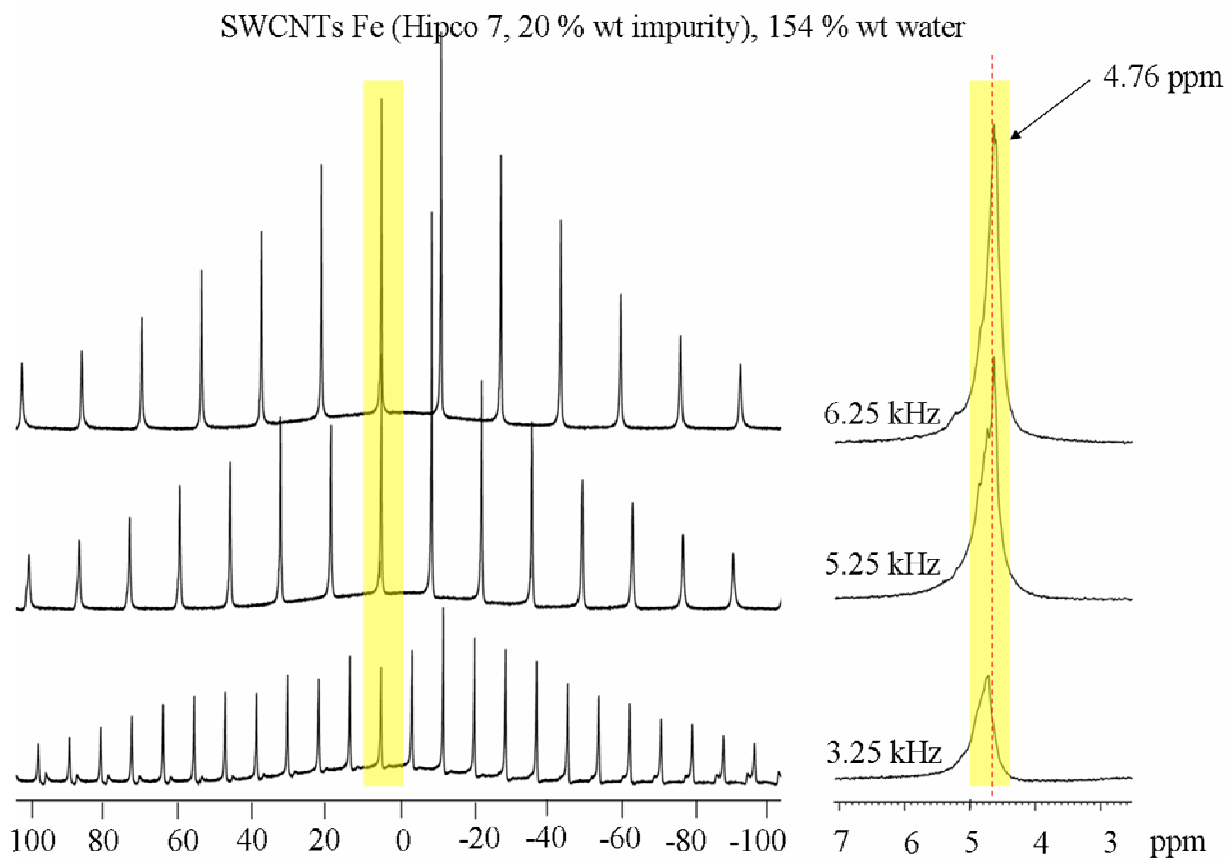


Figure (7.3): A different spinning rate is used to determine the center band of the ^1H MAS SWCNT spectrum (20% Fe impurity), (yellow line shows the centerband).

In figure (7.3) the procedure is shown how to find the centerband of a MAS spectrum with many spinning sidebands. The strongest line is not always the centerband.

There are three features of the spectra in figure 7.2 that need to be mentioned. First, the resonance line for water molecules in SWCNTs with 20 wt% Fe is inhomogeneously broadened; already a relatively low MAS frequency is sufficient to break up the broad line into many spinning sidebands. Secondly, at low Fe concentration the water NMR lines are very narrow, the dipolar interaction between the two proton spins in one water molecule is largely averaged to zero. This means, as can be expected at room temperature, that the water molecules are free to

rotate or tumble. Thirdly, the sample with the lowest Fe concentration shows two lines (apart from the sidebands), while the other two spectra show only one center band. An explanation could be that at the higher Fe concentrations the Fe clusters block the entrances of the nanotubes, preventing water to penetrate into the tubes.

The impurity also affects spin relaxation; the spin-lattice relaxation time T_1 for the most pure SWCNT is about 200 ms, but for the sample with 20 wt% Fe only 32 ms.

The next dependence we investigate is the effect of the amount of water added to the most pure sample. Figure (7.4) shows the effect of water concentration on the proton spectra of the SWCNT sample with 5.9 wt% Fe. At the lowest water loading (37wt %) there are two lines around 1.3 ppm and -15.1 ppm. As more water is added, the line at -15 ppm weakens and the line at 1.3 ppm grows in intensity. Also this line moves slowly somewhat towards low field when the amount of water is increased, possibly because of exchange with the new line that appears at 4.6 ppm at around 214 wt % of water.

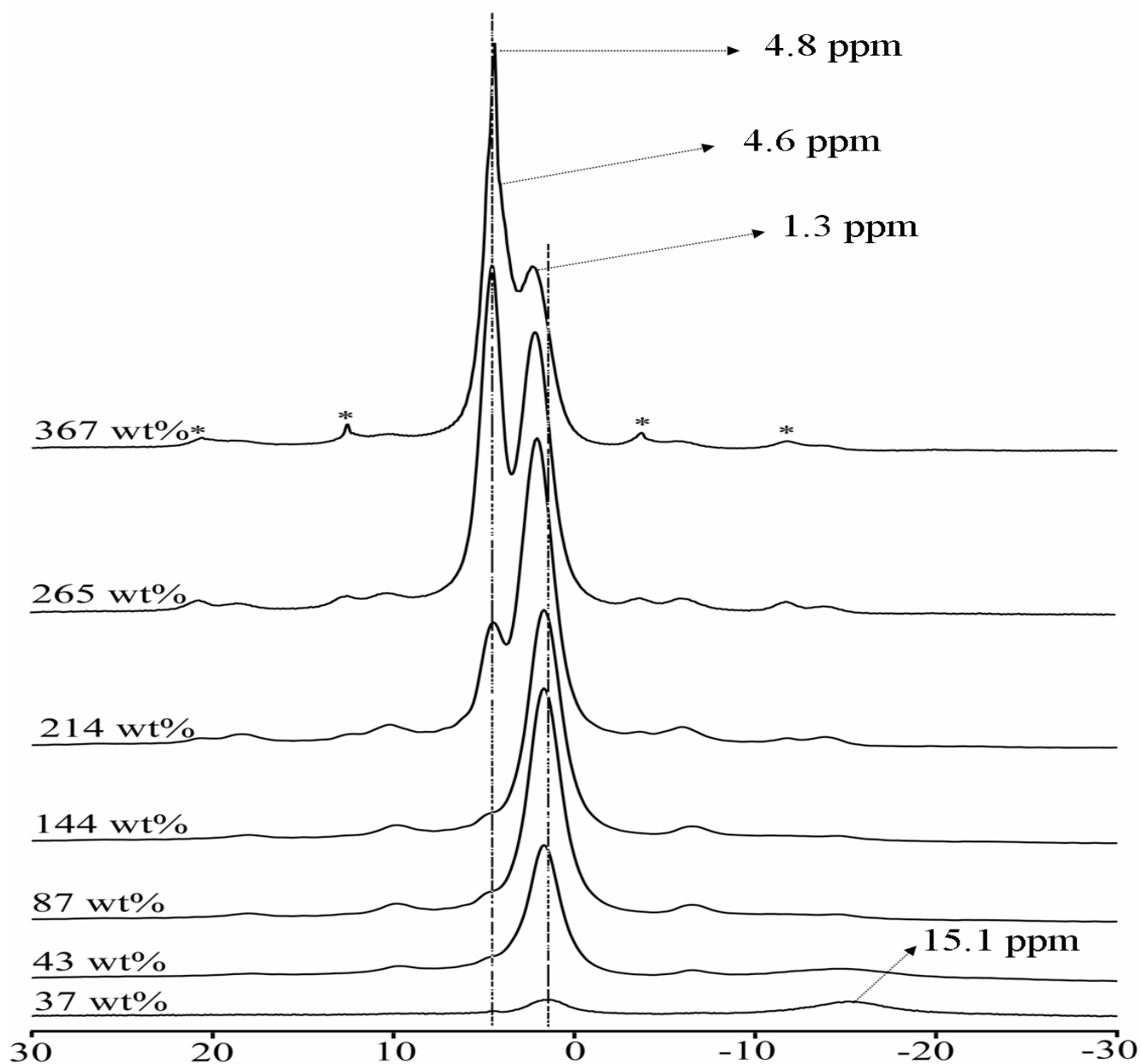


Figure (7.4): ^1H MAS-NMR spectra of water in SWCNT with 5.9 % Fe as a function of the increasing amount of water (*= sidebands).

We observed that the line at 4.6 ppm, whose chemical shift is near to that of free water (4.8 ppm), becomes stronger and stronger and shifts to 4.8 ppm by adding more and more water. At a very high water content the 4.8 ppm completely overwhelms the other lines (not shown). This is a strong indication that the water resonating first at 4.6 ppm and at very high water loadings at

4.8 ppm, is the water present outside the nanotubes. Water responsible for the 1.3 ppm could be from water inside the nanotubes

If this assignment of the two water peaks is correct, then the spectra of fig. (7.4) shows that the first water that is absorbed by the SWCNT sample is absorbed only inside the tubes; this is not completely in agreement with the findings of Ghosh et al. [4].

It is known that water present inside nanotubes should freeze at lower temperatures than bulk water [4, 5]. It is therefore interesting to follow the water NMR lines as a function of temperature. The NMR technique is very sensitive in detecting the difference between the liquid and the solid phase of water (fig. 7.5). The resonance of ice is approximately 50000 Hz wide [6], compared to that of (unconfined) liquid water for which usually the line width is of the order of 1 Hz.

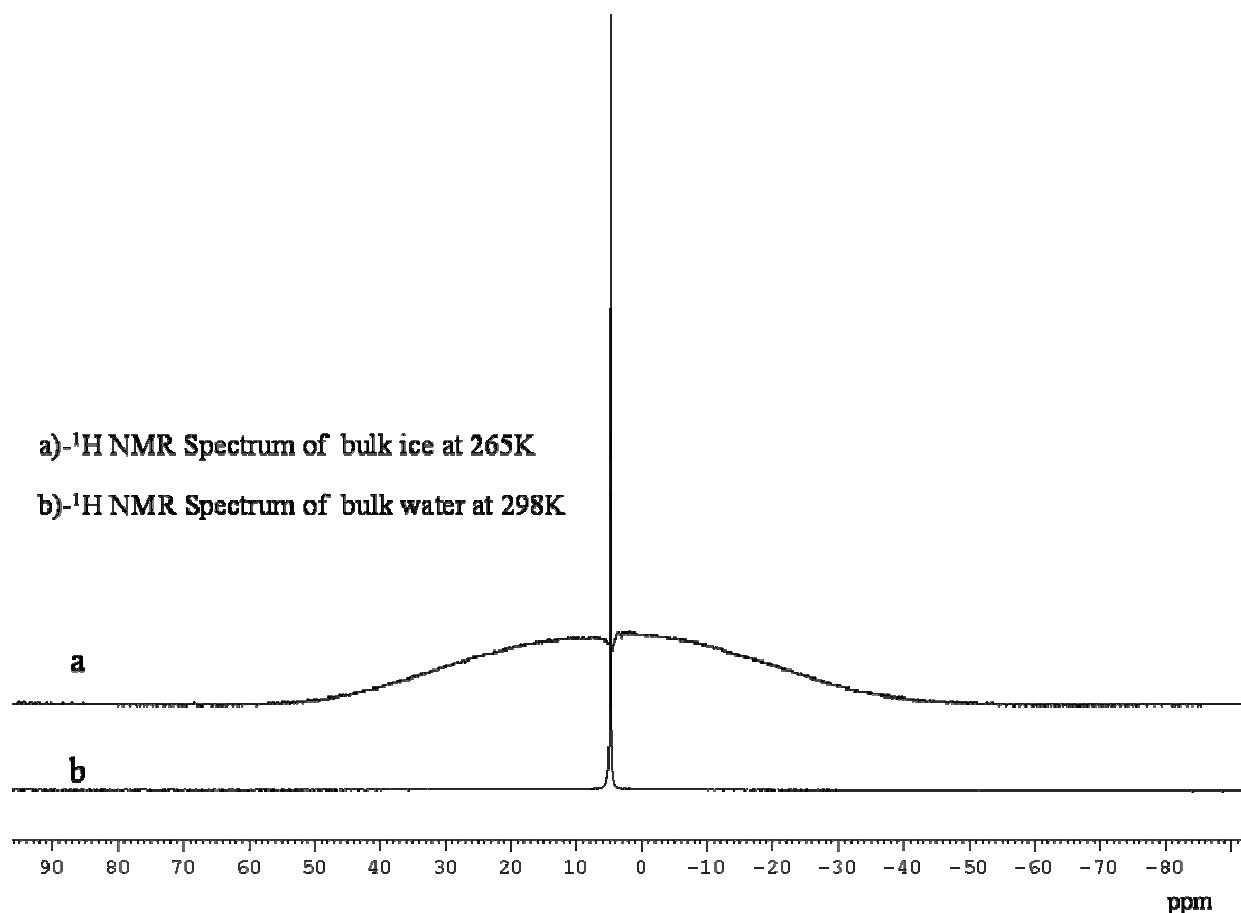


Figure (7.5): ^1H NMR spectra of a) solid water (ice) and b) liquid water at 400 MHz.

A possible transition from water to ice would cause the complete disappearance of the water line from our high resolution spectra.

In figs. 7.6, 7.7, 7.8, 7.9 and 7.10 we show the change of the proton spectra for five different water concentrations on lowering the temperature from 298 K to a temperature where the NMR lines have practically disappeared by broadening. The line at around 4.6 ppm, whose presence is clear only in the spectra with 214% (fig. 7.9) and 318 % water (fig.7.10), disappears at temperatures at around 250 K. In contrast, the water responsible for the line at around 1.3 ppm is liquid down to a temperature of at least 244 K for 87 % water (figure (7.7) and 144 % water figure (7.8)) and down to at least 220 K for 214 to 366 % water (fig. 7.8 and fig. 7.9). All lines do not change when passing the freezing temperature of bulk water. This finding also strongly supports the assignment of the 4.6 ppm resonance to more or less free water, adsorbed at the outside of the nanobundles and the 1.3 ppm line to water inside the nanotubes.

It is difficult to compare our spectra of figures (7.6) and (7.7) with previously published wide line spectra [3, 4], because in these Letters the amount of water in the samples has not been reported, nor has the chemical shift reference. At low water content, except for the unassigned line at -15 ppm, we have one line at 1.3 ppm, which could be the line detected by Mao et al. [3]. The spectrum at 300 K published by Ghosh et al. [4], figure (7.1), in the absence of MAS also shows two lines, but their behavior with temperature differs from that of our two lines at 4.6 and 1.3 ppm at higher water loadings: in the spectrum of Ghosh et al. the high field line disappears first when the temperature is lowered, while in our case the low field line disappears first.

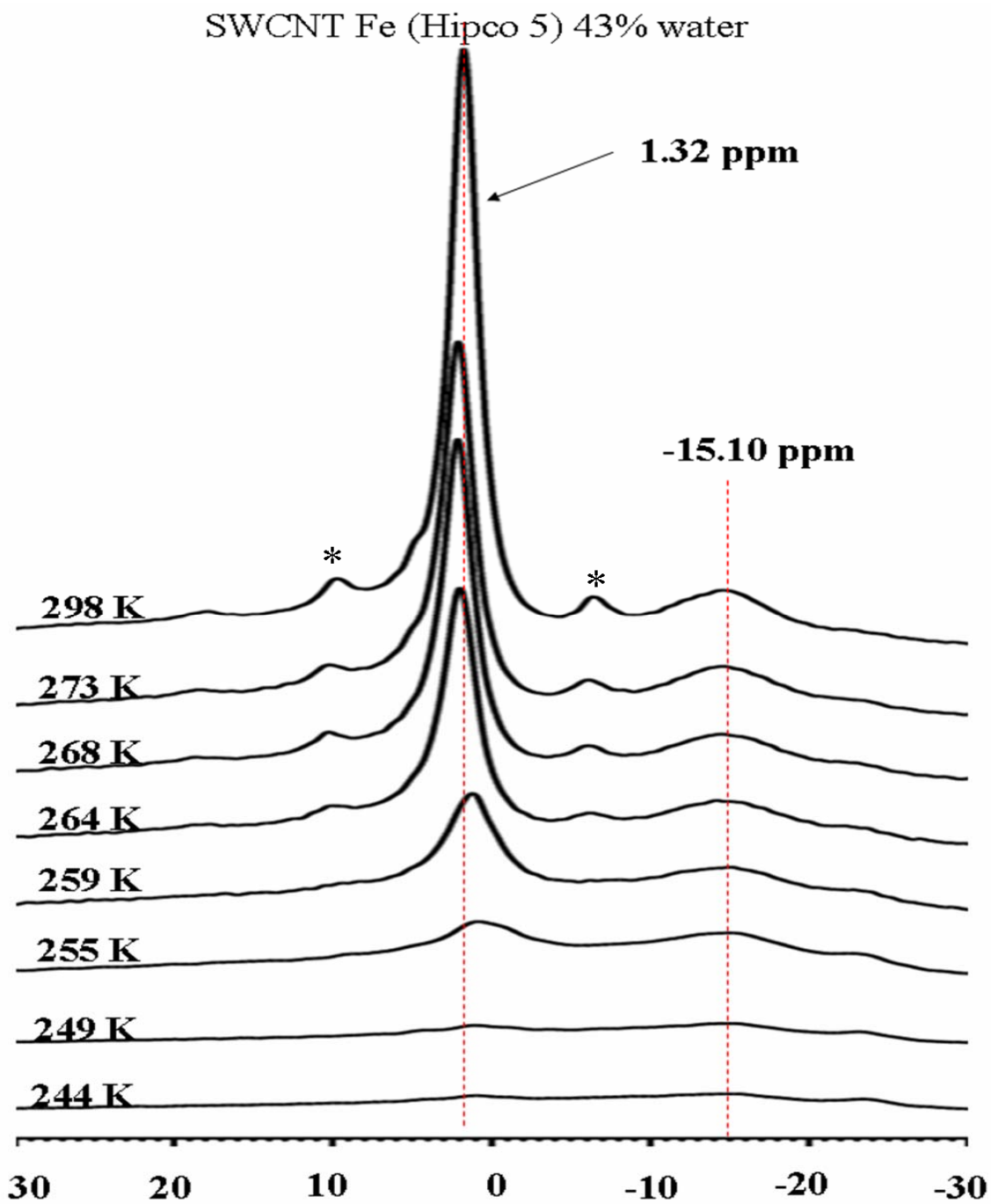


Figure (7.6): ^1H NMR spectra of water in SWCNT HiPCO (5.9 % Fe) as a function of temperature with 43 wt % water (sidebands).*

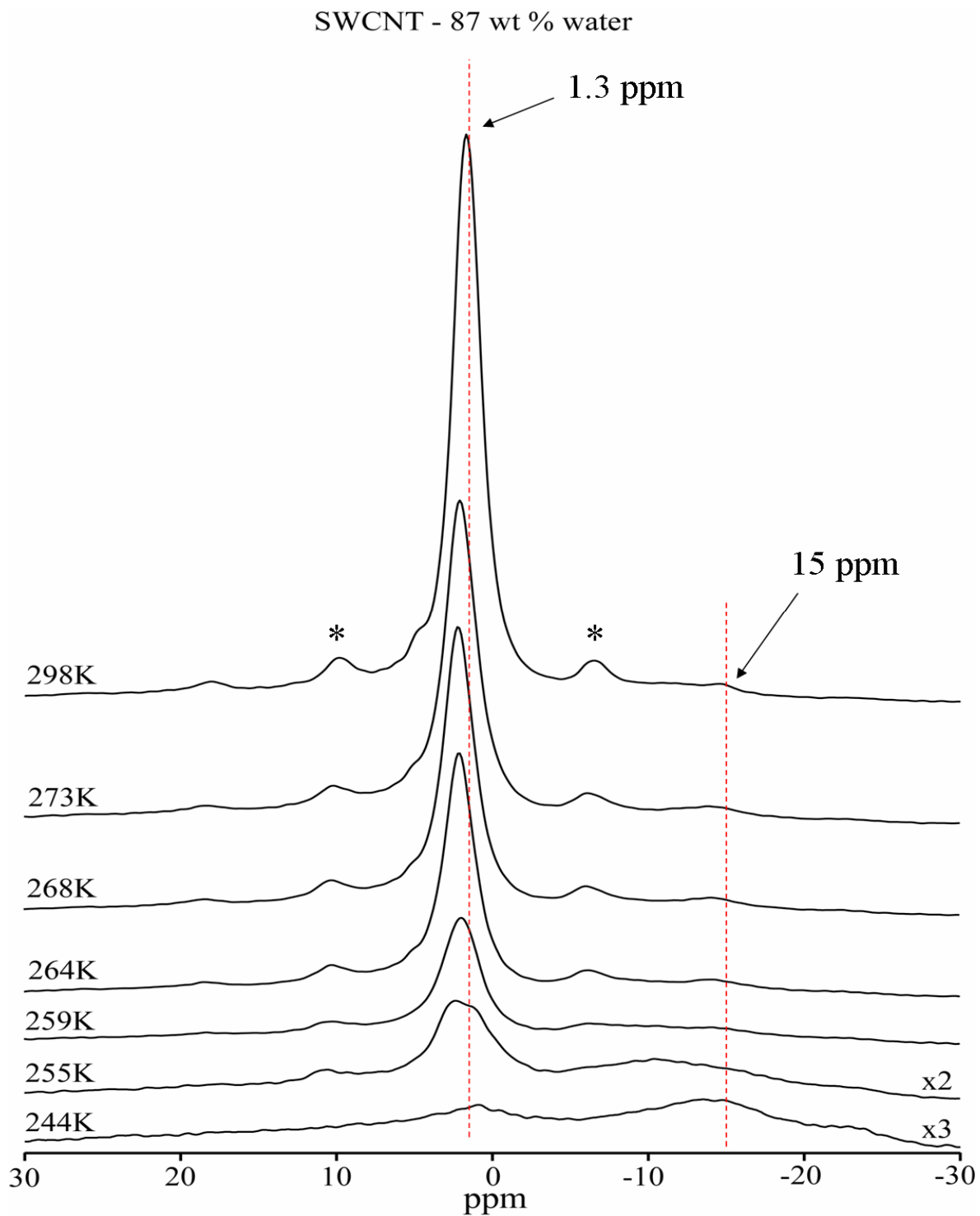


Figure (7.7): ^1H MAS NMR spectra of water in SWCNT HiPCO (5.9 %) as a function of temperature with 87 wt % water (* sidebands).

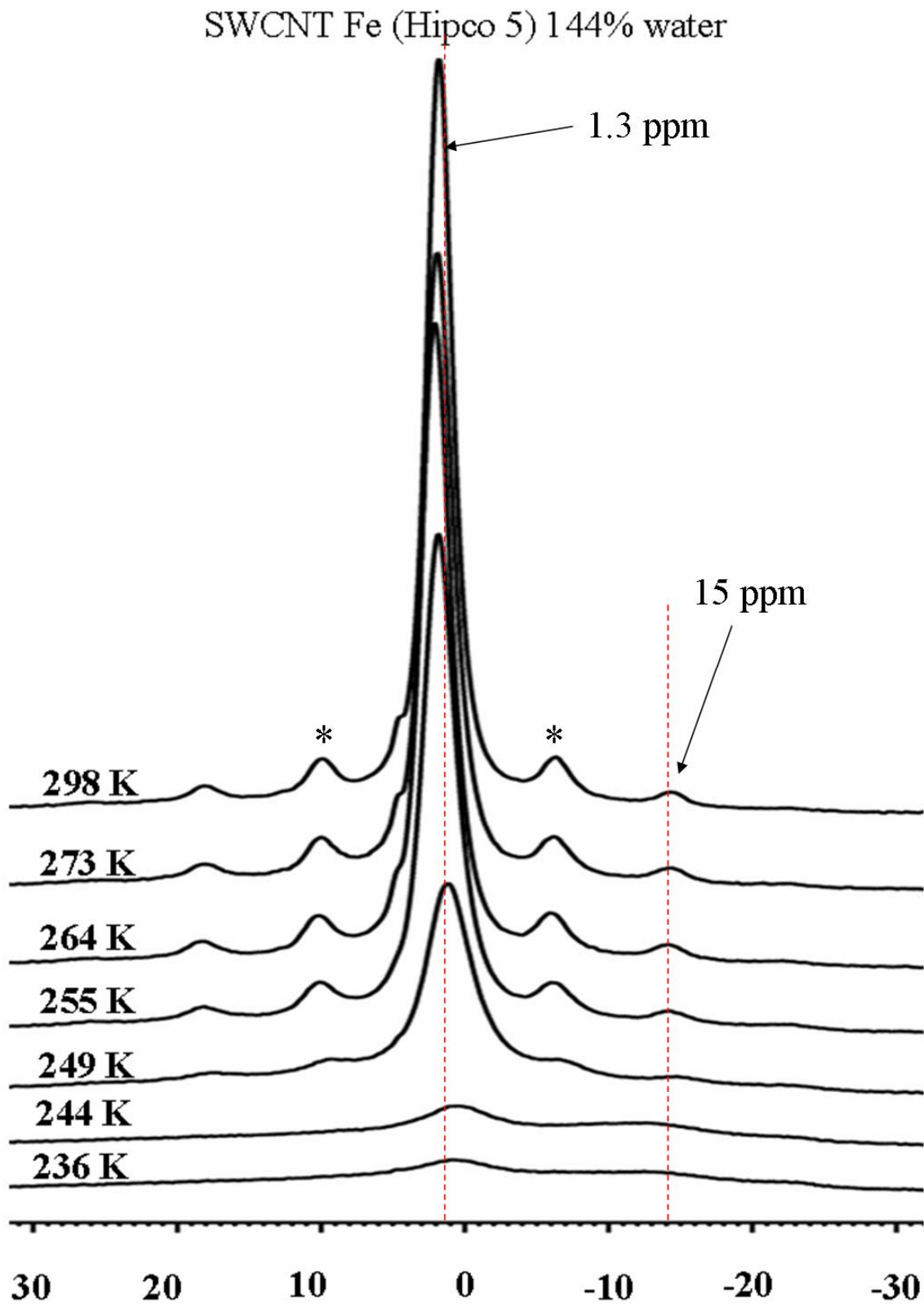


Figure (7.8): ^1H MAS NMR spectra of water in SWCNT HiPCO (5.9 % Fe) as a function of temperature with 144 wt % water (= sidebands).*

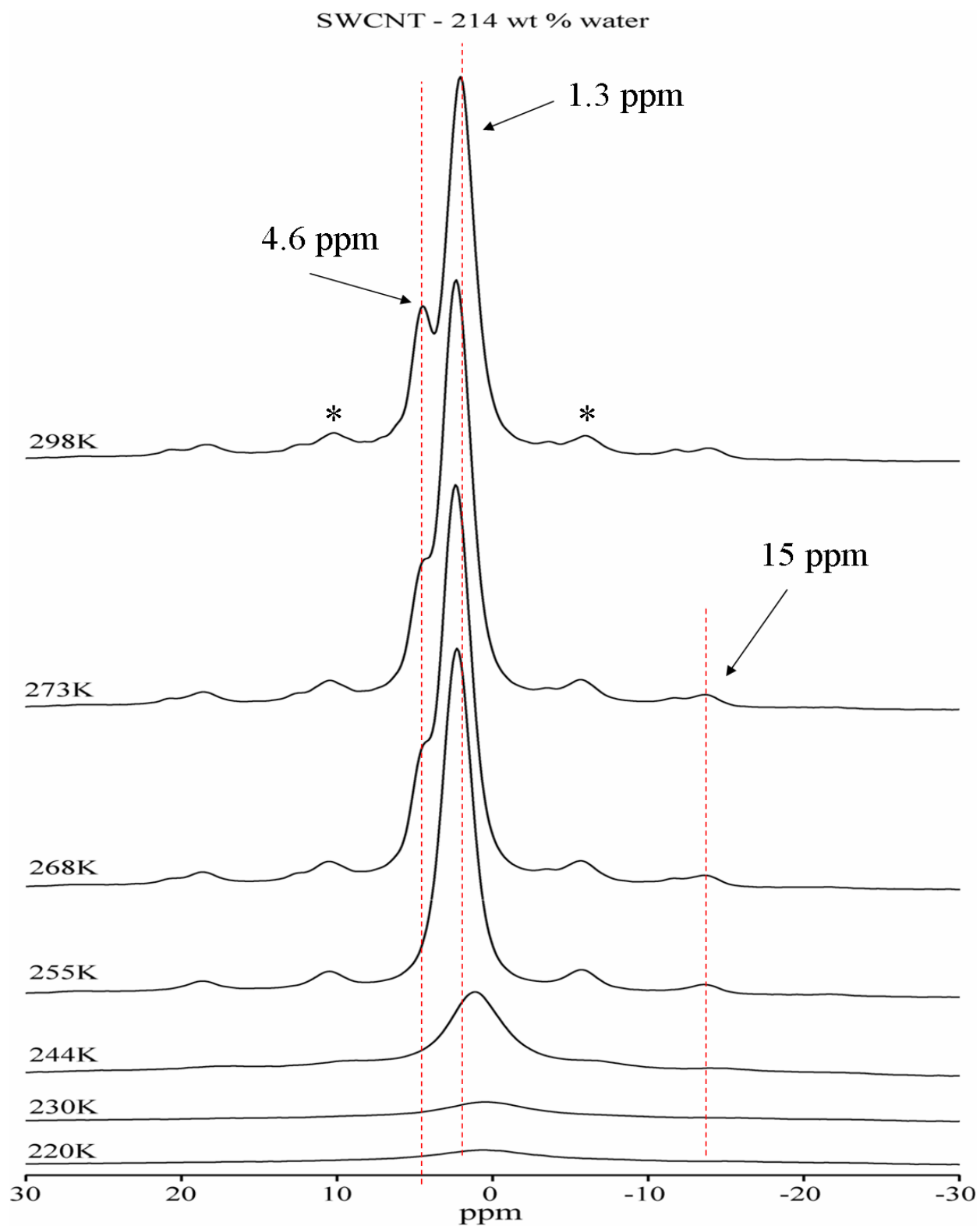


Figure (7.9): ^1H MAS-NMR spectra of water in SWCNT (5.9 % Fe) as a function of temperature with 214 wt % water (*= sidebands).

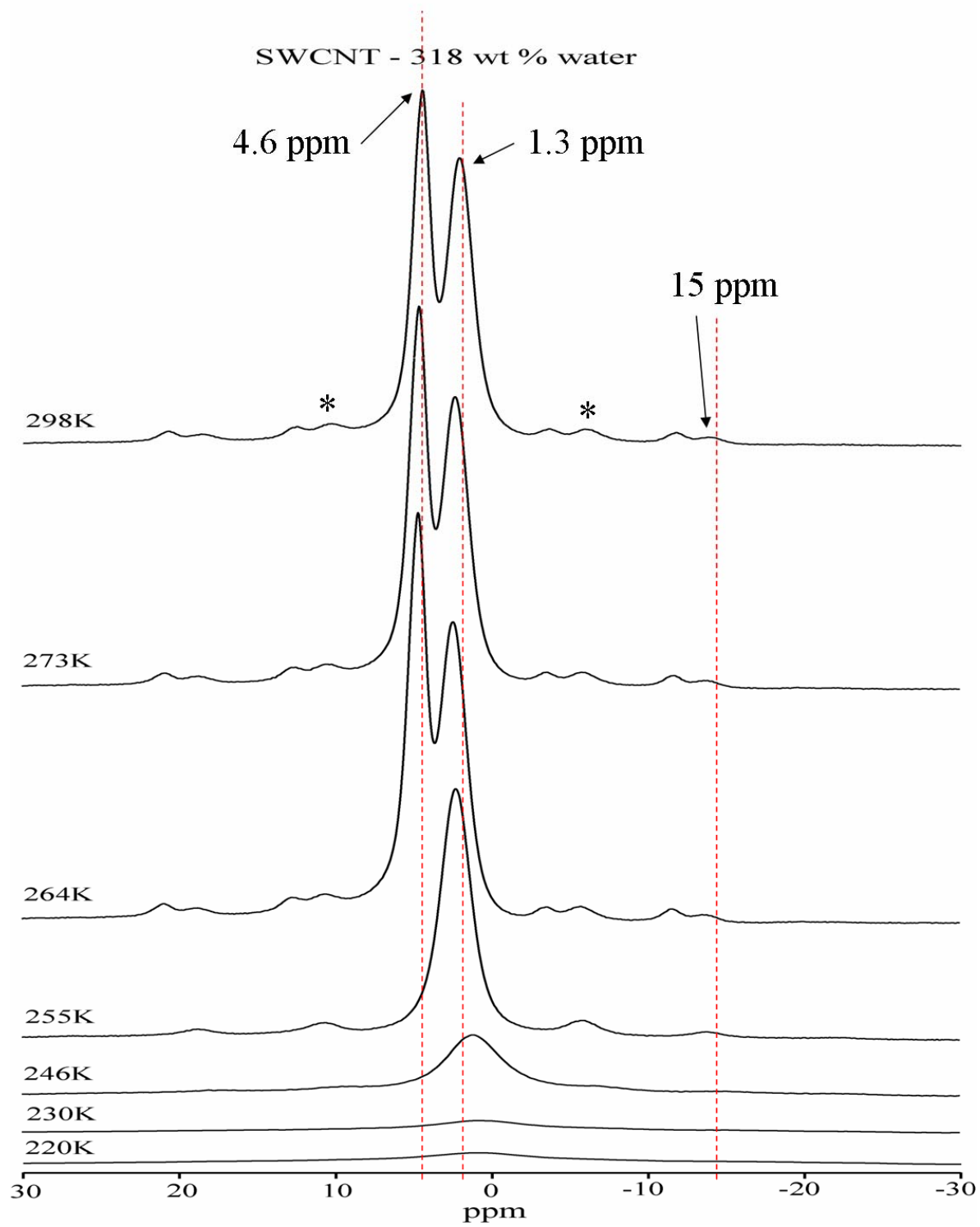


Figure (7.10): ^1H MAS-NMR spectra of water in SWCNT (5.9 % Fe) as a function of temperature with 318 wt % water (*= sidebands).

From the above ^1H spectra, as a function of the water concentration and as a function of temperature, it seems more than likely that the 1.3 ppm line is due to water inside the nanotubes and the 4.6 – 4.8 ppm line due to outside water. In figure 7.2 we saw that only at the lowest Fe concentration two lines are found. At higher Fe concentrations only the centerband at ca. 5 ppm shows up. In principle this could be due to some isotropic shift the water protons experience from the magnetic clusters. A second possibility, which we mentioned already, is that the Fe clusters may block the nanotubes so that the water molecules cannot penetrate into the tubes. This hypothesis can be tested by monitoring the temperature dependence of the water line in the samples with higher Fe concentration, inside water should freeze at much lower temperatures than 273 K. We first show the room temperature spectra of the SWCNTs with 13 wt % Fe as a function of the water loading, then followed by the temperature dependence of the proton spectra for water loaded SWCNTs with 13 wt % and 20 wt % Fe.

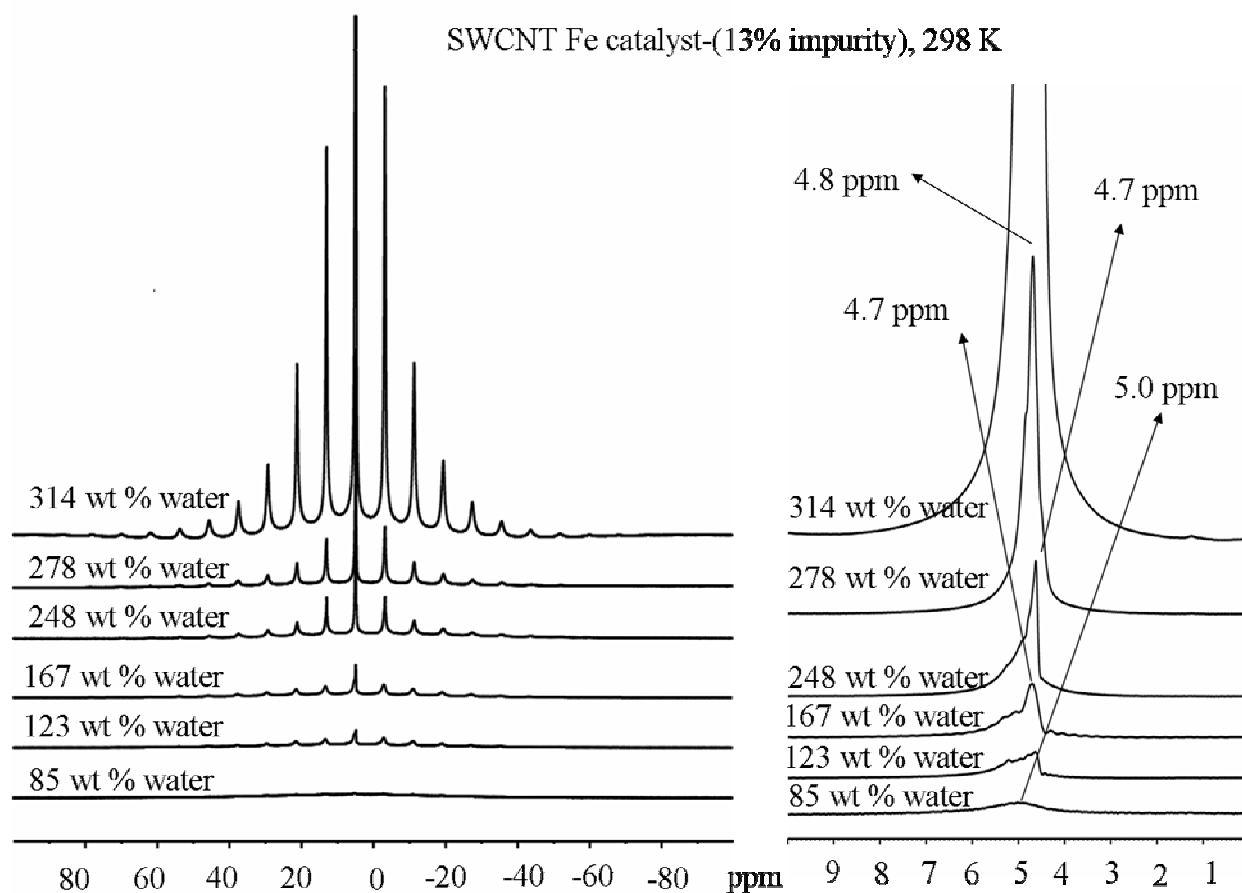


Figure (7.11): The effect of water concentration on the proton spectra of SWCNT with 13 wt % Fe; at the left the total spectrum is shown, at the right the centerbands.

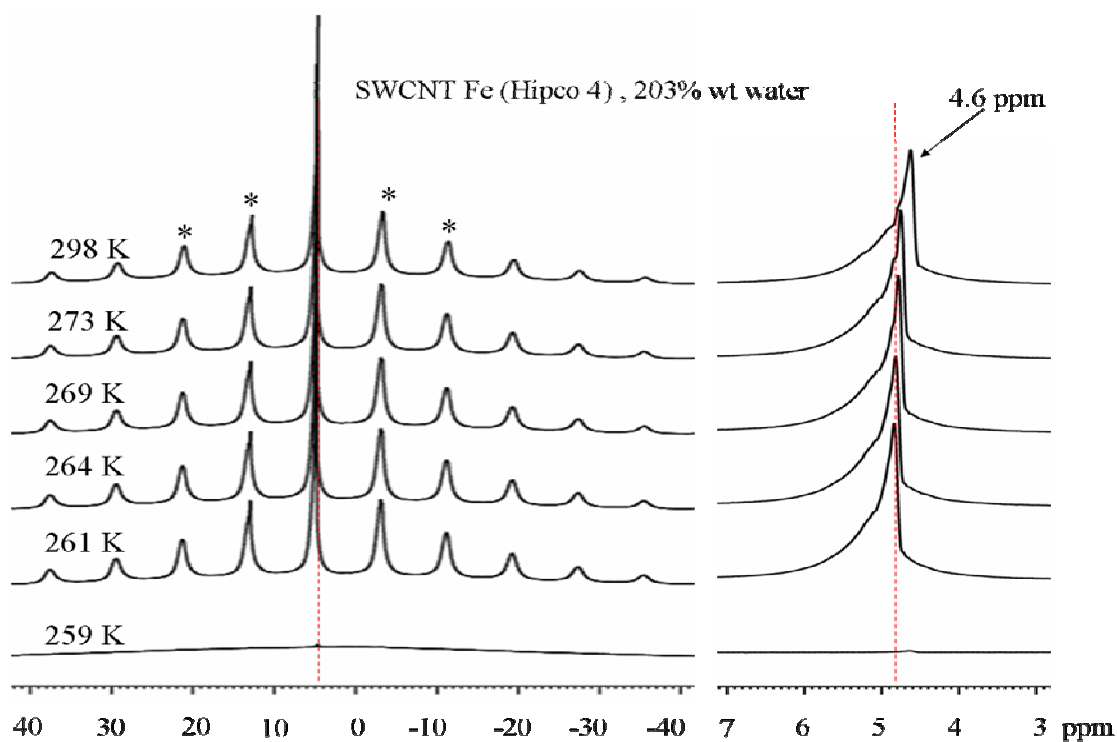


Figure (7.12): ^1H MAS-NMR spectra of water in SWCNT (13wt% Fe) as a function of temperature with 203 wt % water (*= sidebands).

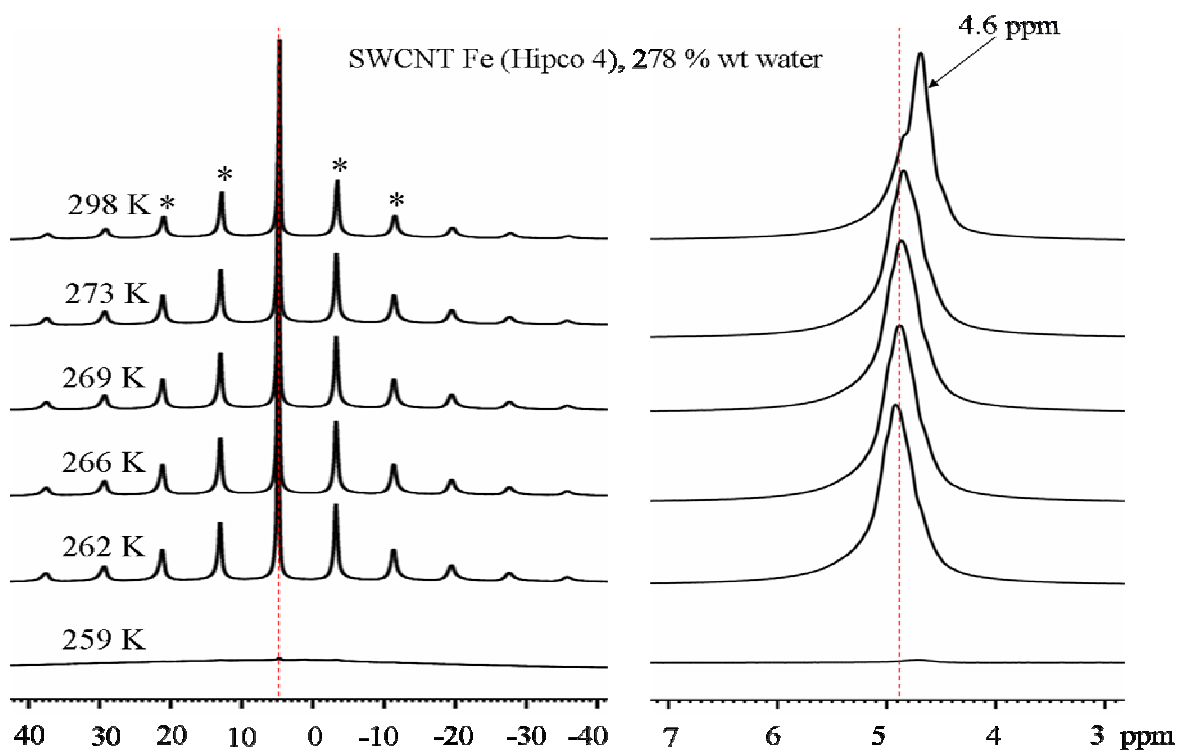


Figure (7.13): ^1H MAS-NMR spectra of water in SWCNT (13wt% Fe) as a function of temperature with 278 wt % water (*= sidebands).

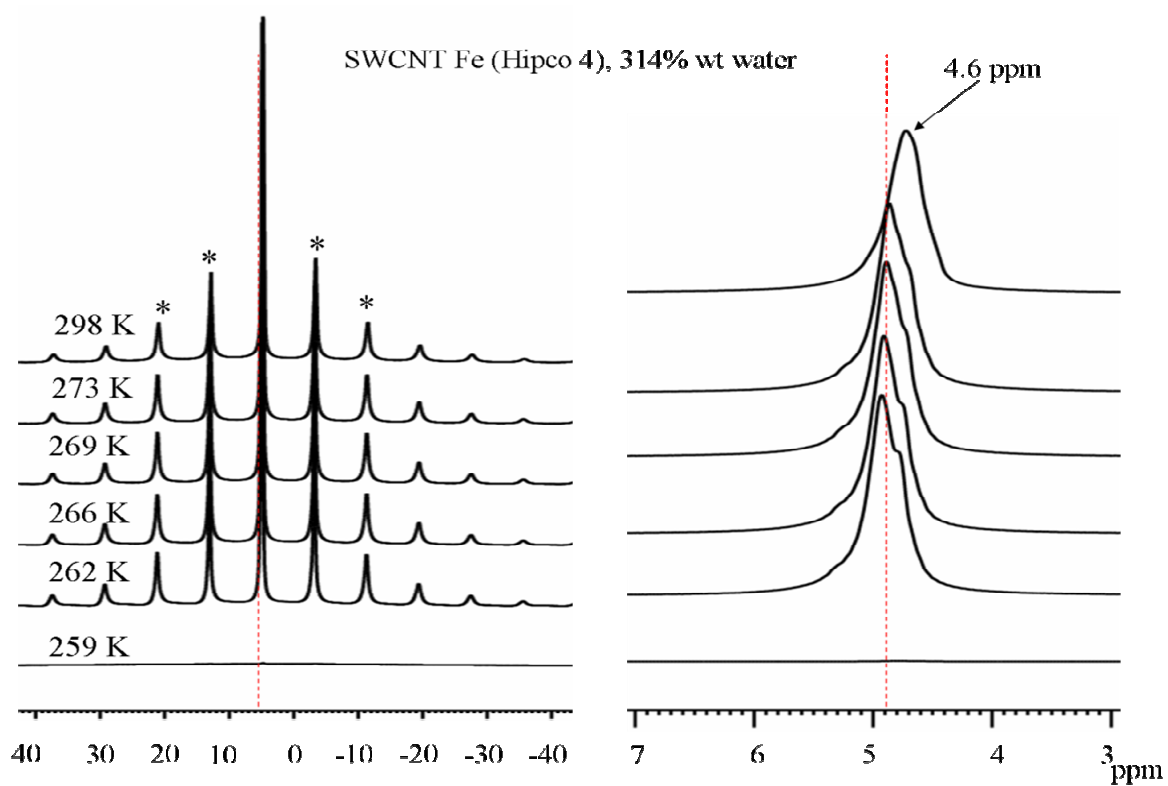


Figure (7.14): ^1H MAS-NMR spectra of water in SWCNT (13wt% Fe) as a function of temperature with 314 wt % water (*= sidebands).

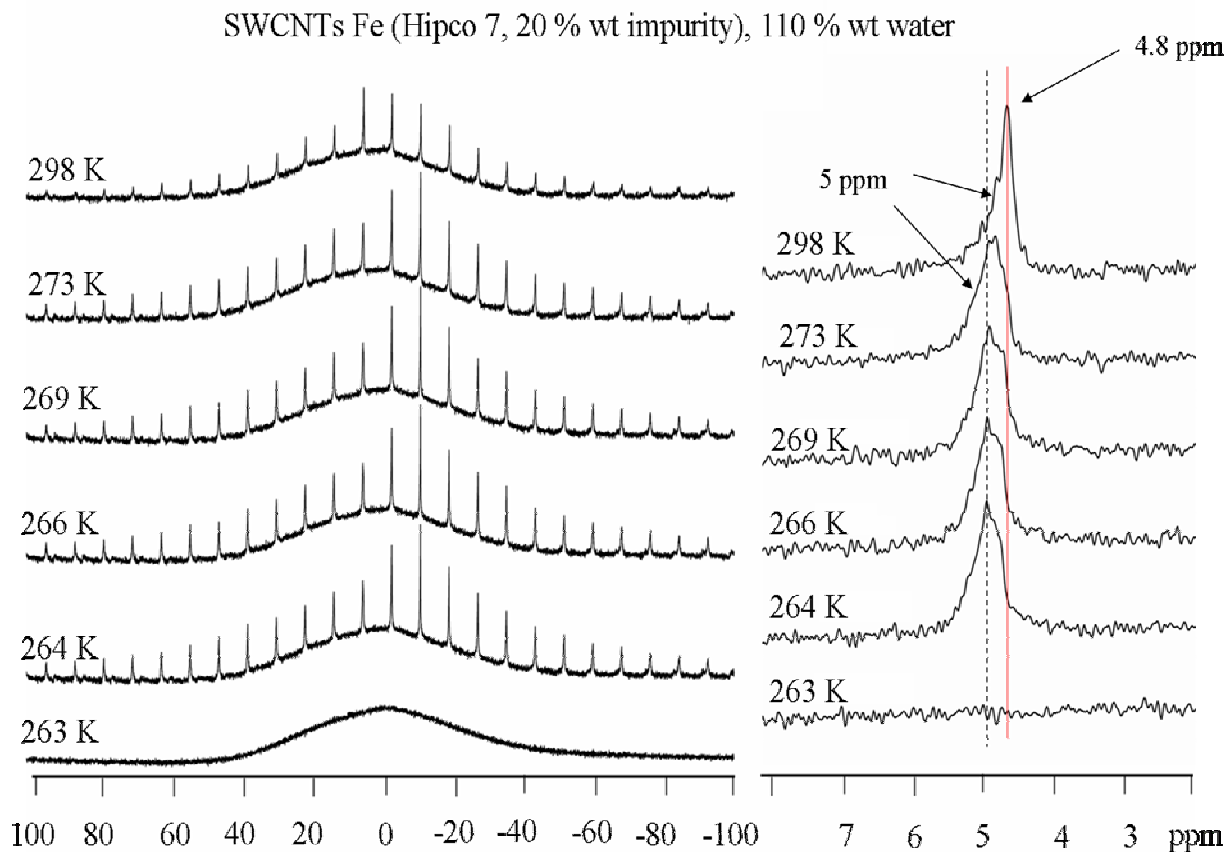


Figure (7.15): ^1H MAS-NMR spectra of water in SWCNT Fe (20 wt% impurity) as a function of temperature with 110 wt % water, the spinning speed was 3250 Hz spectrum at different temperatures.

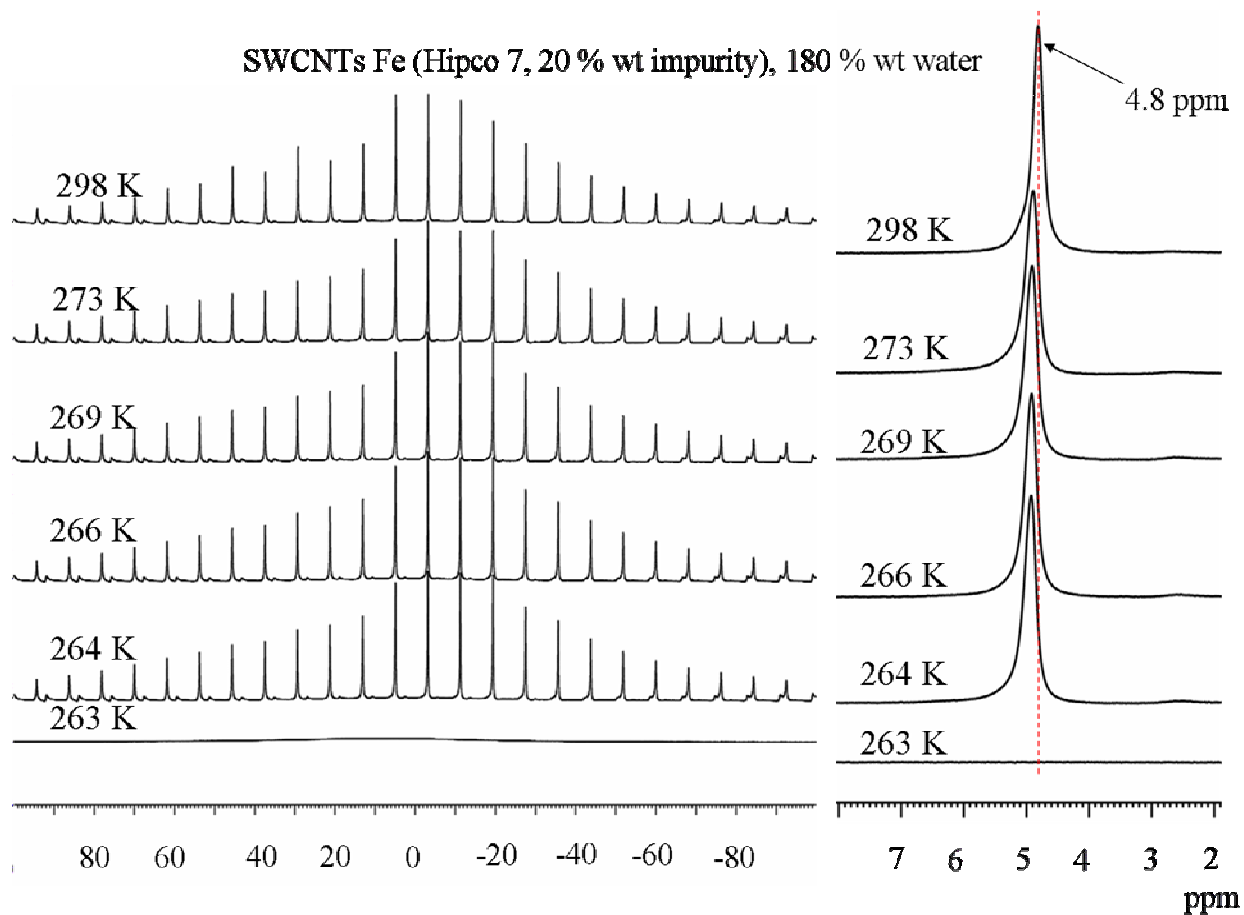


Figure (7.16): ^1H MAS-NMR spectra of water in SWCNT Fe (20wt % impurity) as a function of temperature with 180 wt % water, the spinning speed was 3250 Hz.

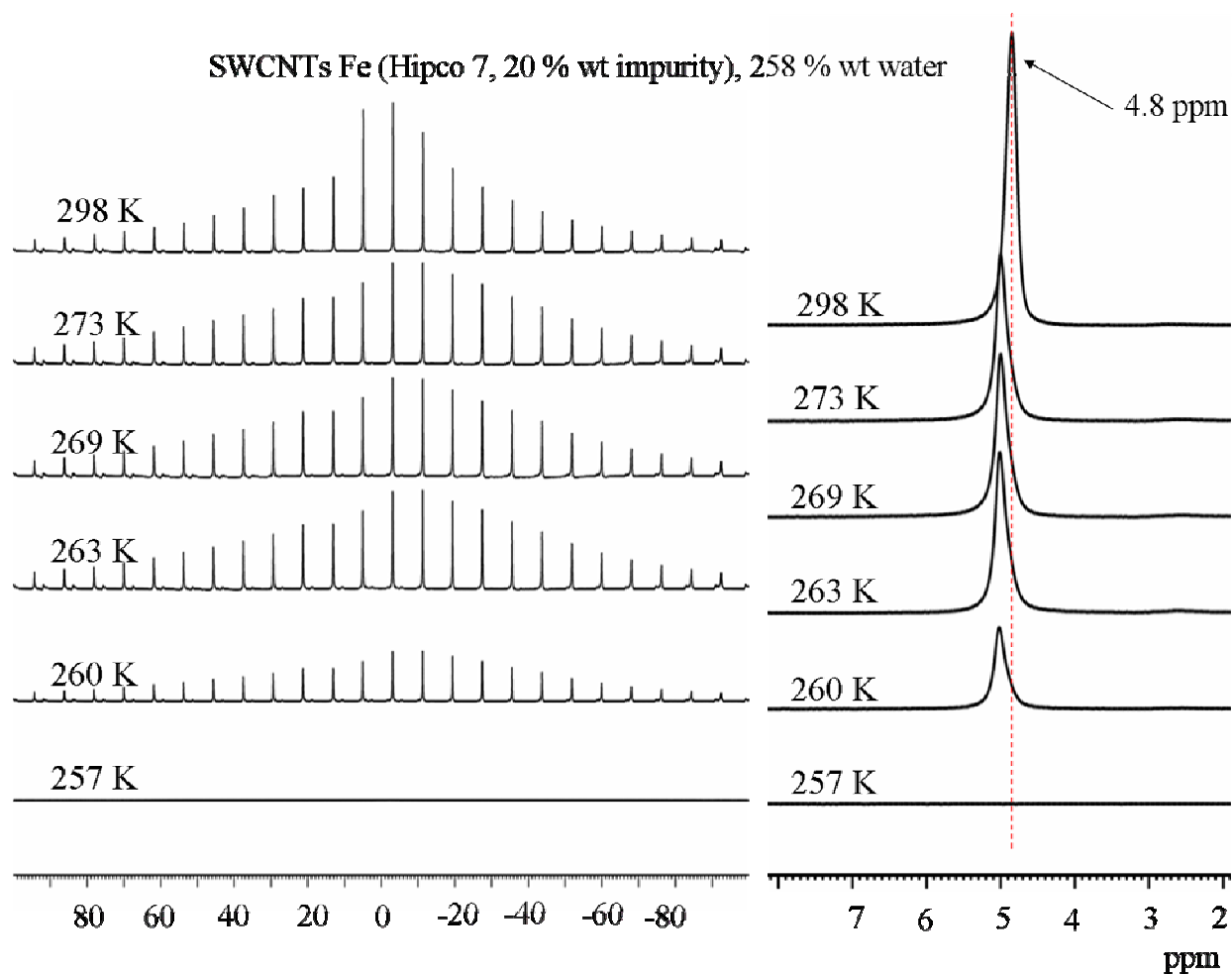


Figure (7.17): ^1H MAS-NMR spectra of water in SWCNT Fe (20wt % impurity) as a function of temperature with 258 wt % water, the spinning speed was 3250 Hz.

From the spectra in figures (7.12) to (7.16) we can conclude that in all cases all resonances disappear at around 260 K. The resonances certainly do not originate from water inside the nanotubes.

7.3 The chemical shift of water inside a single wall carbon nanotube

As discussed in the previous part of this chapter we find two distinct water signals, one of water inside the nanotubes at ca. 1.3 ppm and one of water outside the tubes at ca. 4.6 – 4.8 ppm. Fig. 7.18 shows the relative sizes of water and the nanotube with 1.0 nm diameter. Water is clearly much smaller in size than the nanotube and from that point of view it is no surprise that water can enter the tube.

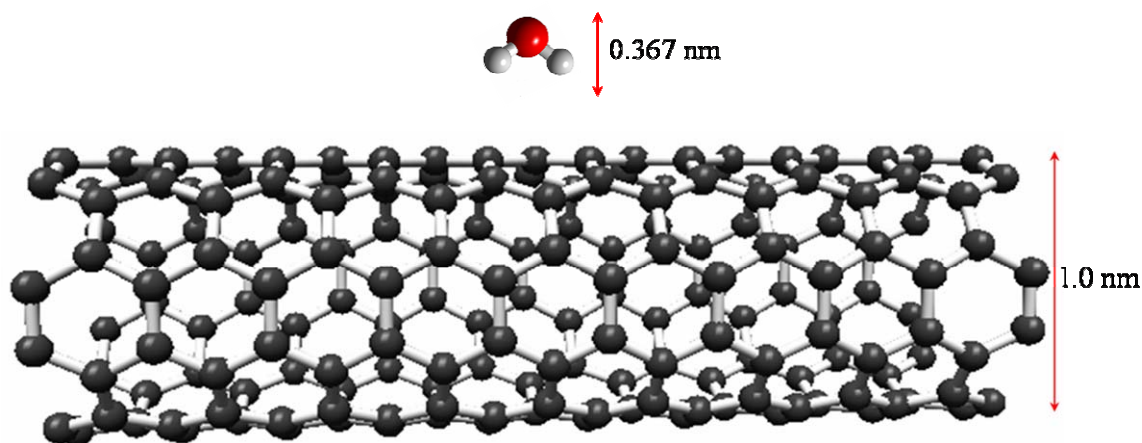


Figure (7.18): The dimension of water molecules relative to the nanotube.

The question is where the outside water is located. The SWCNTs are usually packed in a bundle with inter-tube distance of 0.34 nm (see figure 7.19). Since the inter-tube space is of the same order of magnitude as the water molecule dimension, we assume that water cannot penetrate the inter-tube void. The outside water must therefore be found in the space between the bundles, probably as small droplets or as water adsorbed at a tube at the outside of a bundle. The chemical shift of bulk water is 4.8 ppm. The temperature dependent shift we observe for the outside water, between 4.6 and 4.8 ppm, is probably due to exchange of water molecules between the bulk droplets and a state in which they are adsorbed at the outside of the bundle.

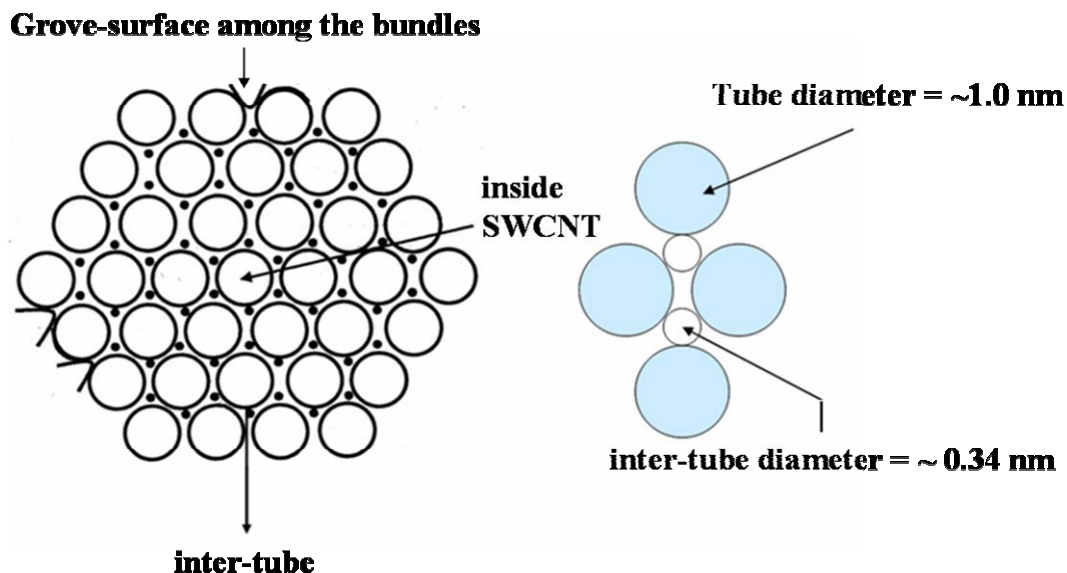


Figure (7.19): Schematic structure of a SWCNT bundle.

An important question in our discussion is the sign and the size of the shift of the resonance of water inside the nanotubes (1.3 ppm) relative to that of free water at 4.8 ppm. There can be many causes for such a shift. First, it has been proposed in the literature that water molecules inside the carbon nanotubes have less hydrogen bonds at room temperature towards each other than in bulk water [5, 7-10, 11-15]. This should cause an upfield shift relative to bulk water [16], which agrees with our findings.

It is further known that SWCNTs can be metallic or semiconducting depending on their radius and helical arrangement. As has been mentioned in chapter two, the typical ratio of the number of metallic to semiconductor tubes is 2 to 1. A very interesting question in this respect is: would water in a metallic tube have a different chemical shift than water in a semiconducting tube? Both lines should show the freezing point depression; therefore it is sure that the two lines we observe are not due to water in metallic and in semiconducting tubes. Since we observe only one line due to inside water in the investigated temperature range, water in metallic and in semiconducting tubes must have, at least approximately, the same chemical shift!

Another possible cause for a shift of the water proton resonance frequency is the shielding from the external magnetic field B_0 by ring currents induced in the tubes. To calculate at least the sign

of the shift due to ring currents, up-field or down-field, we have the problem of not knowing the paths nor the strengths of the currents in the complex topology of the carbon nanotube. In a first approximation, we assume that the ring currents exist only in the benzene hexagons and simply add the effects of all benzene rings. This also circumvents the difficult problem of how to treat metallic and semi-conducting tubes.

The concept of ring current has been used since a long time to account for the chemical shift of protons close to one or more aromatic rings [17, 18, 19, 20]. The chemical shift tensor of a nuclear spin close to an aromatic ring can be written as $\sigma = \sigma_{rc} + \sigma_{local}$, where σ_{rc} is the ring current contribution to the chemical shift tensor and σ_{local} is the contribution from all other shielding mechanisms (see figure 7.20).

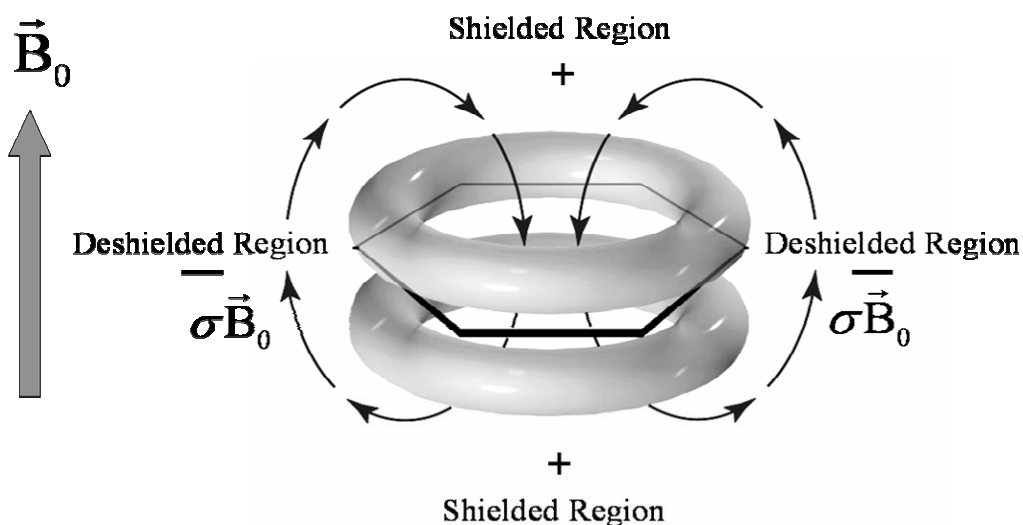


Figure (7.20): The ring-current effect

According to the Waugh and Fessenden [19] model, the ring current contribution part σ_{rc} comes from the additional induced magnetic field due to the six circulating π electrons. It is known that the π electron cloud has its maximum density in two doughnut-like rings on either side of the plane of ring. The distance between these loops is found to be 0.64 \AA [17]. The contribution to σ_{rc} from each current loop is calculated in the coordinate frame whose origin is at the center of benzene ring with the z axis defined by the ring normal and x axis is chosen to be in the plane of

the ring, so that the field induced by the ring current has no y- component using electrodynamic formalism described by Smythe [18].

The magnetic field at an arbitrary point P(x, y, z) induced by a circular current loop I of radius a located in the x-y plane and centered at the origin is shown in figure (7.21).

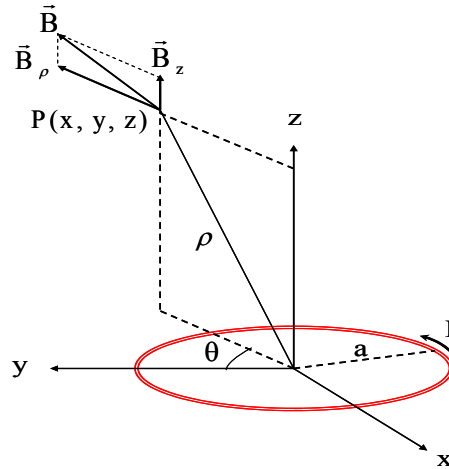


Figure (7.21): The magnetic field induced by a circular current loop located in x-y plane.

The magnetic field components are expressed in terms of cylindrical coordinates and elliptic integrals of first and second order, as shown below [18]:

$$B_{\rho} = \frac{\mu_0 I}{2\pi} \cdot \frac{z}{\rho \sqrt{[(a+\rho)^2 + z^2]}} \cdot \left[\frac{a^2 + \rho^2 + z^2}{(a-\rho)^2 + z^2} E(k) - K(k) \right] \quad (7.1)$$

$$B_z = \frac{\mu_0 I}{2\pi a} \cdot \frac{z}{\sqrt{[(a+\rho)^2 + z^2]}} \cdot \left[\frac{R^2 - \rho^2 - z^2}{(a-\rho)^2 + z^2} E(k) + K(k) \right] \quad (7.2)$$

$$B_0 = 0 \quad (7.3)$$

where ρ in units of a is the vector from the observed proton to the origin of the aromatic ring and k is the modulus of the complete elliptic integrals K and E that can be expressed by

$$k = \sqrt{4\rho / \{(1+\rho)^2 + z^2\}} \quad (7.4)$$

where E and K are the complete elliptic integrals of second and first kind, respectively,

$$E(k) = \int_0^{2\pi} (1 - k^2 \sin^2 \phi)^{1/2} d\phi \quad (7.5)$$

$$K(k) = \int_0^{2\pi} (1 + k^2 \sin^2 \phi)^{-1/2} d\phi \quad (7.6)$$

defined on the variable k :

$$k^2 = \frac{4a\rho}{(a+\rho)^2 + z^2} \quad (7.7)$$

The contribution to the σ_{rc} from each current loop is given by equation (7.8) [18, 19].

$$\sigma_{zz}^{rc} = \frac{3e^2}{6\pi mc^2 a} \cdot \frac{1}{\sqrt{[(1+\rho)^2 + z^2]}} \cdot \left[K(k) + \frac{1-\rho^2-z^2}{(1-\rho)^2+z^2} E(k) \right], \quad (7.8)$$

Figure (7.22) shows the isoshielding ring current contributions to the isotropic chemical shift for points inside and outside the carbon nanotube in a plane perpendicular to the tube. These calculations have been done by Dr. Kotecha by using Matlab program.

The orientation of the tube relative to the external static magnetic field is along the magic angle. This would be the average orientation of every tube during MAS. For positions at the center of the tube, there is a more or less constant upfield shift of 5-5.5 ppm.

The calculated shift then becomes $4.8-(5 \text{ to } 5.5) = -0.2 \text{ to } -0.7$ ppm, not far from the experimental value when we take into account that the shift becomes smaller when the water molecule moves off-center. The final conclusion about the 1.3 ppm line is that the shift from the bulk water chemical shift has the right sign. More accurate calculations have to be done to see if this agreement is accidental or whether it means that the largest ring currents are indeed in the benzene rings.

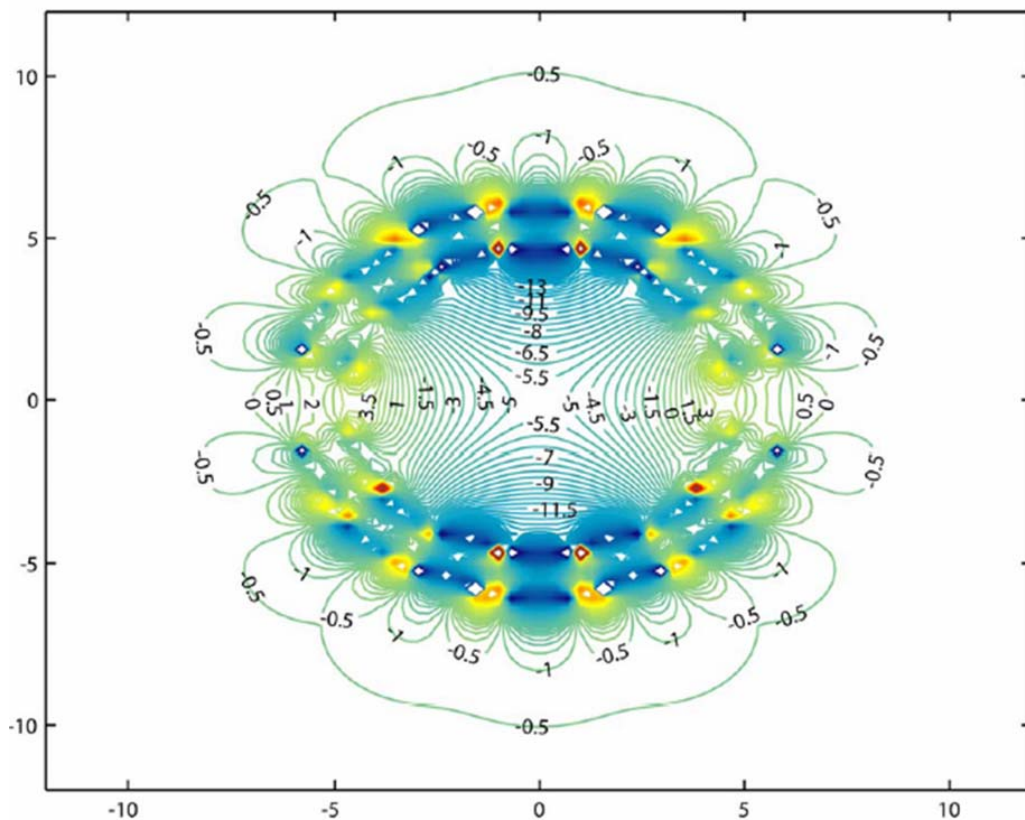
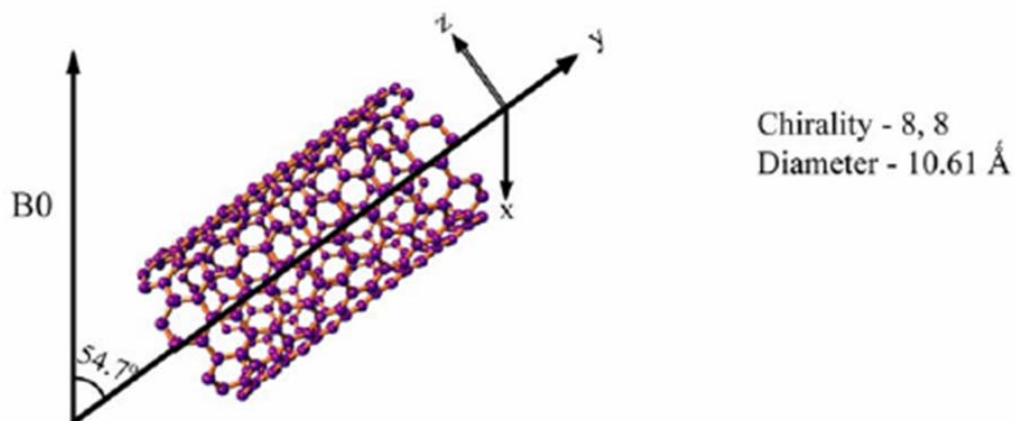


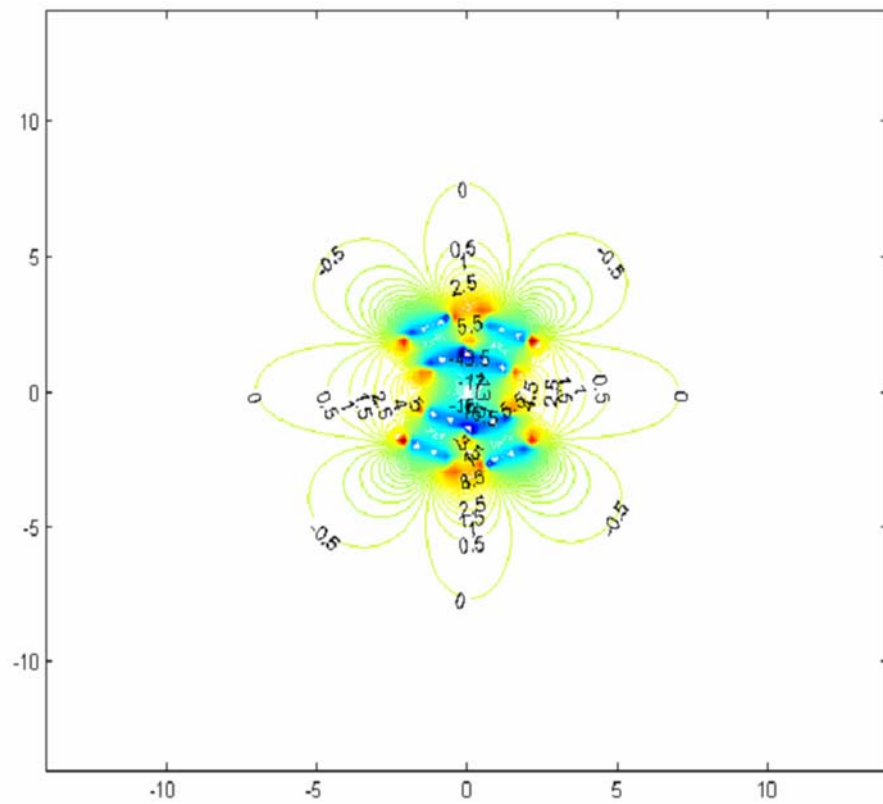
Figure (7.22): The calculated isoshielding lines for a tube (8, 8) with $d \approx 1.06$ nm making the magic angle with \mathbf{B}_0 [21].

The following figures show the calculated isoshielding lines for nanotubes of different diameters. The lines represent the ring current contribution to the isotropic chemical shift for a

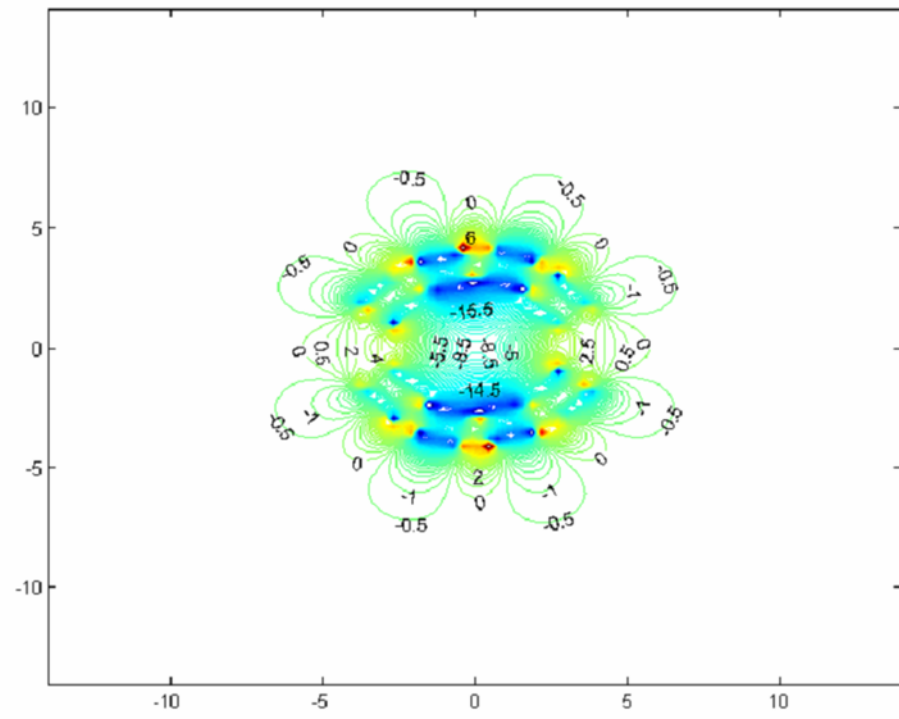
tube making the magic angle with the external magnetic field. The tube length ranges from 3.98 - 26.54 Å. The distance of the current loops from the plane of the benzene ring = 0.64 Å, the chirality (n, m) = (3, 3) till (20, 20) leads to a tube diameter of $\frac{\sqrt{3}}{\pi} a \sqrt{m^2 + mn + n^2}$ Å. The results are summarized in Table (7.1).

Table (7.1): The isoshielding ring current contribution inside single wall carbon nanotube varies inversely with the diameter of the tube.

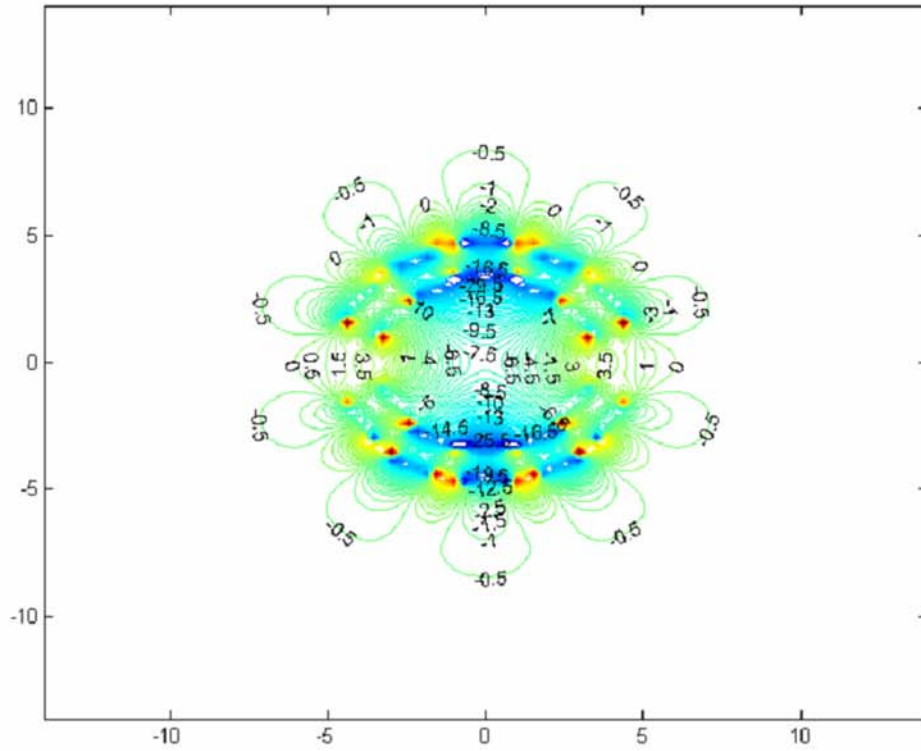
Chirality (m, n)	Nanotube Diameter(Å)	Relative shift at different point inside tube
(3.3)	3.98	13-17
(4.4)	5.30	9 - 11.5
(5.5)	6.64	8.5 - 9.5
(6.6)	7.96	6.5 - 7.5
(7.7)	9.23	6 - 6.5
(8.8)	10.61	5 - 5.5
(9.9)	11.94	4.5 - 5
(10.10)	13.27	3.5 - 5
(11.11)	14.60	3 - 3.5
(12.12)	15.92	2.5 - 3.5
(13.13)	17.25	2.5 - 3
(14.14)	18.57	2 - 2.5
(15.15)	19.90	2-2.5
(16.16)	21.23	1.5 - 2
(17.17)	22.55	1.5 - 2
(18.18)	23.88	1 - 1.5
(19.19)	25.21	1 - 1.5
(20. 20)	26.54	1 - 1.5



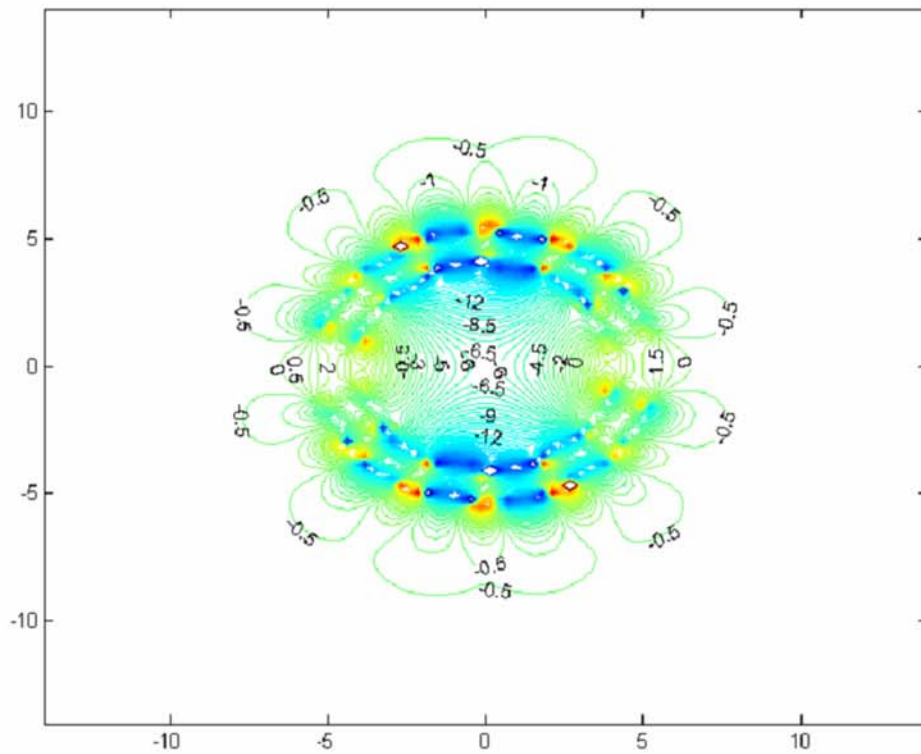
$(n, m)=(3, 3), d=3.98 \text{ \AA}^\circ$



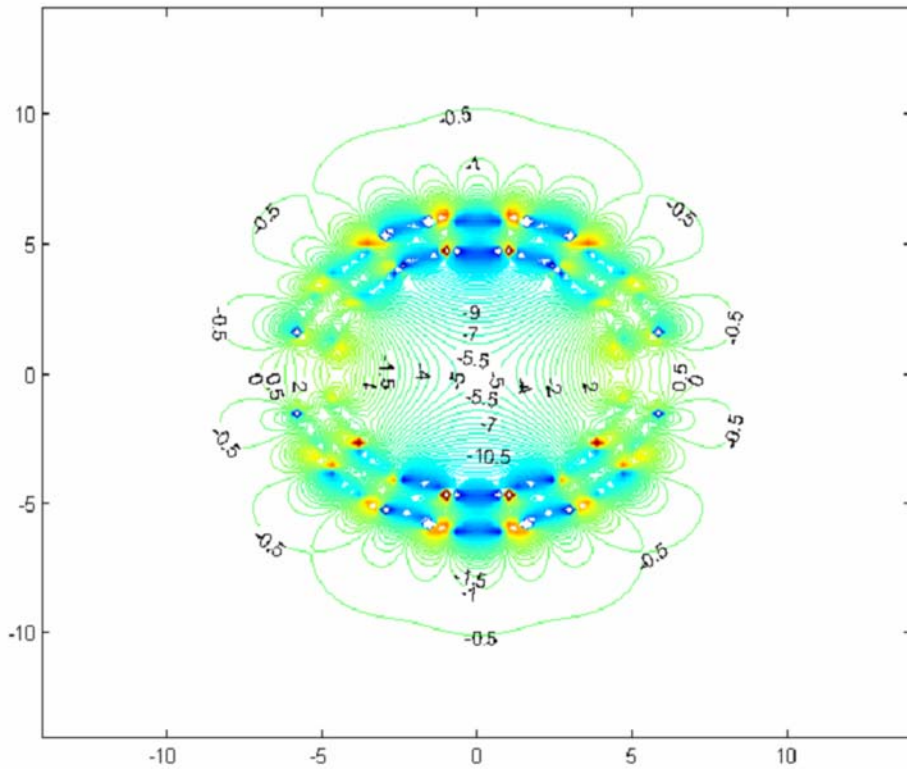
$(n, m)=(5, 5), d=6.64 \text{ \AA}^\circ$



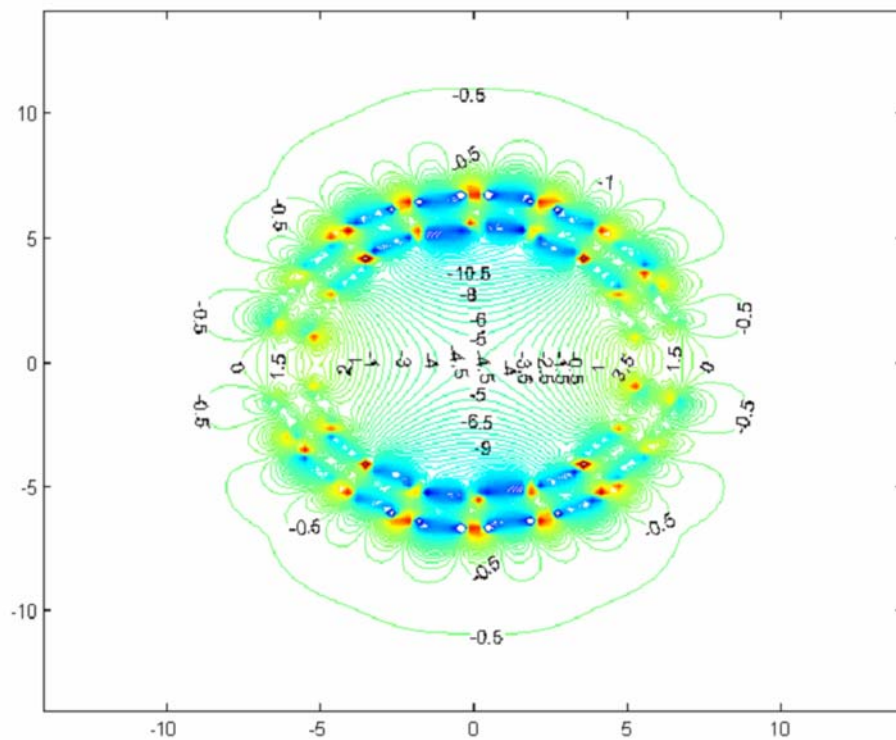
$(n, m)=(6, 6), d=7.96 \text{ \AA}$



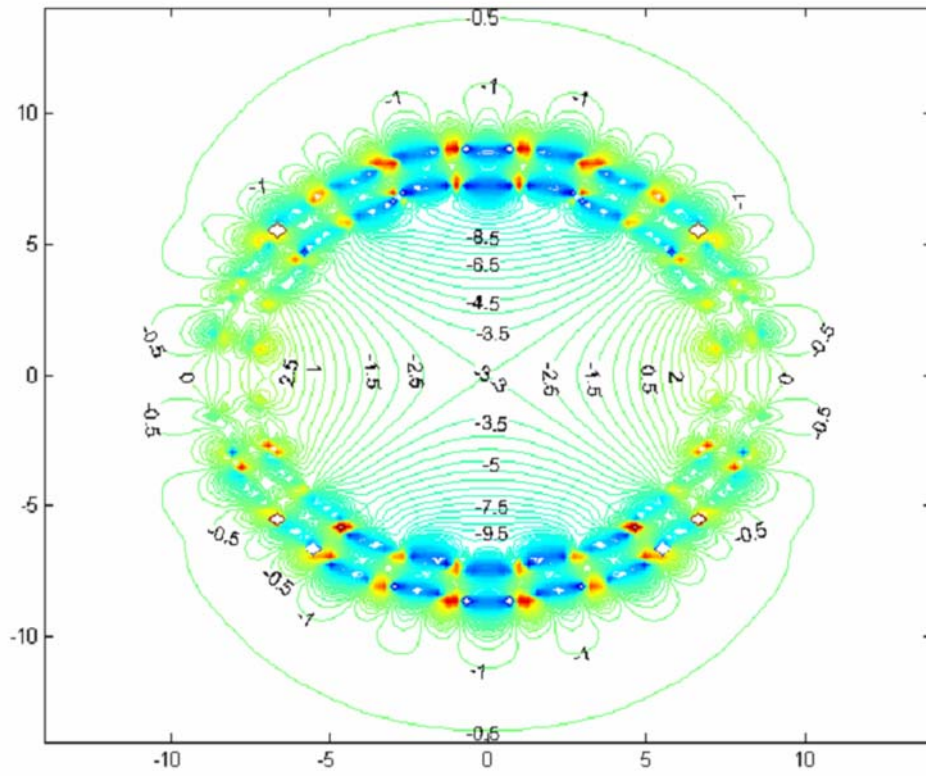
$(n, m)=(7, 7), d=9.23 \text{ \AA}$



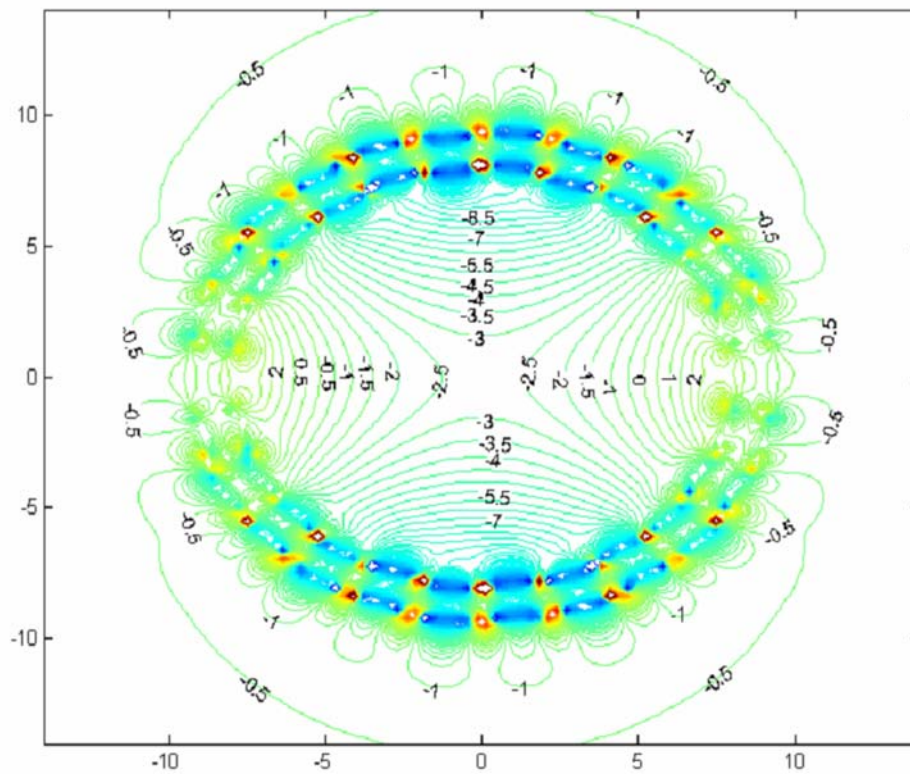
$(n, m) = (8, 8)$, $d = 10.61 \text{ \AA}$



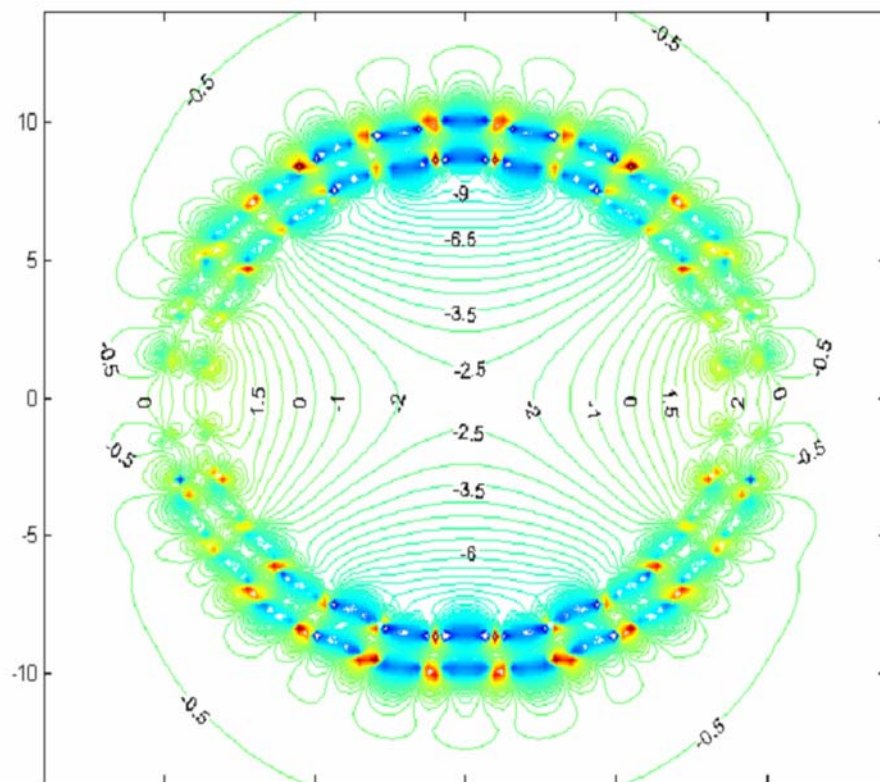
$(n, m) = (9, 9)$, $d = 11.94 \text{ \AA}$



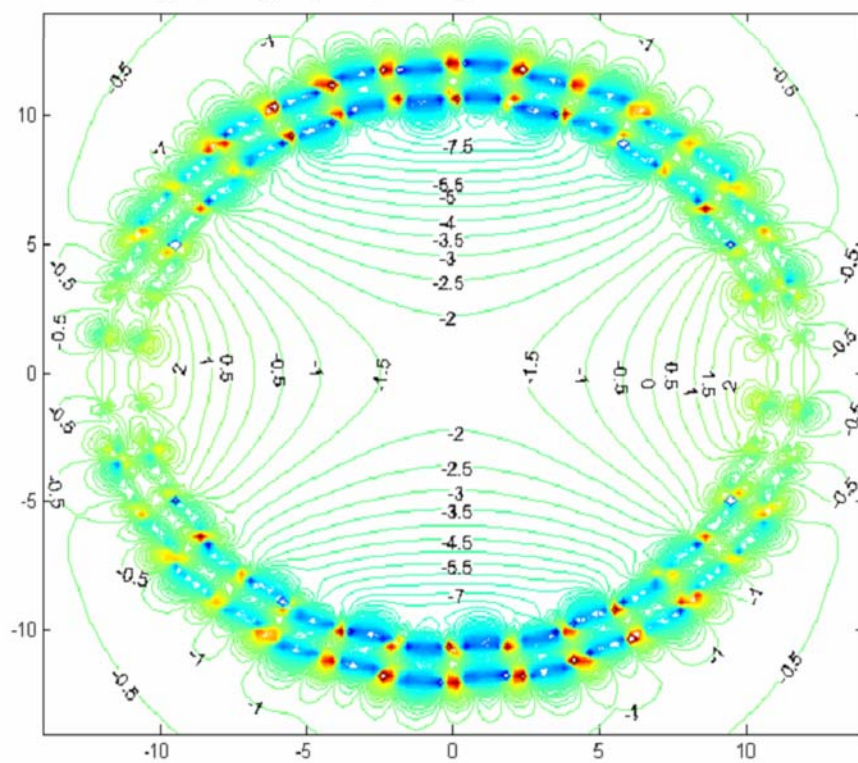
$(n, m)=(12, 12), d=15.92 \text{ \AA}^\circ$



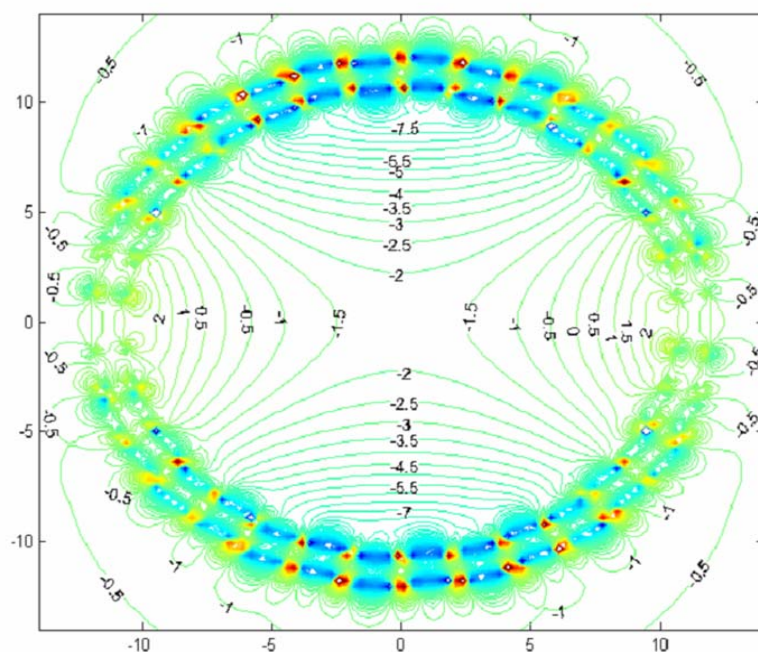
$(n, m)=(13, 13), d=17.22 \text{ \AA}^\circ$



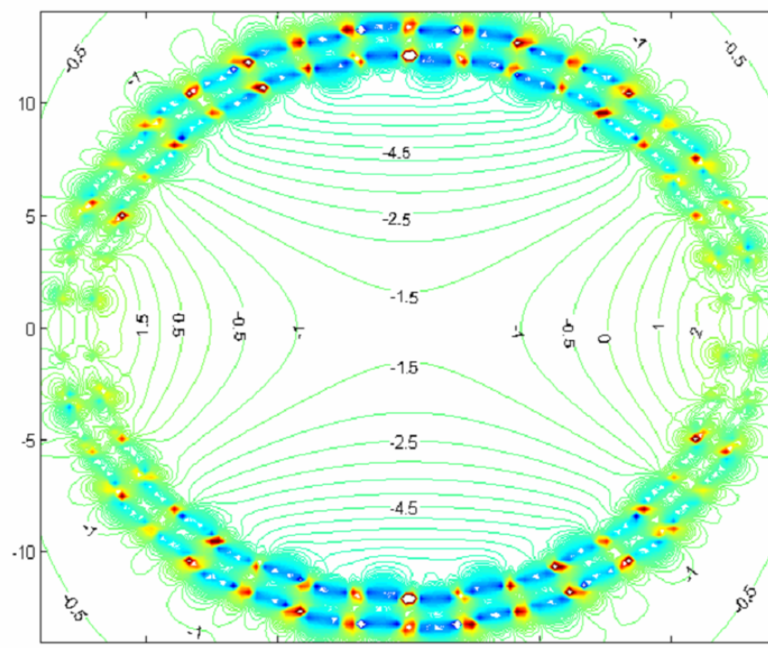
$(n, m) = (14, 14)$, $d = 18.57 \text{ \AA}$



$(n, m) = (15, 15)$, $d = 19.90 \text{ \AA}$



$(n, m) = (16, 16)$, $d = 21.23 \text{ \AA}$



$(n, m) = (17, 17)$, $d = 22.55 \text{ \AA}$

Figure (7.23): The calculated isoshielding lines for nanotubes with varying diameters.

The final conclusion from the simulations is that the ring current effects of the combined benzene rings give a shift for water at the center of the tube depending on the diameter of the tube. For a tube, resembling the tube of our experiments, the calculated shift has the correct sign and size. More accurate calculations have to be done to see if this agreement is accidental or whether it means that the largest ring currents are indeed in the benzene rings. As mentioned above, the calculation completely neglects the metallic or semiconducting properties (or the chirality) of the nanotube.

A yet unsolved problem is the assignment of the resonance at -15 ppm. The large upfield shift seems too large for water in the nanotubes or from protons of functional groups attached to SWCNTs [3]. The large shift and the relatively small line width seem to point to mobile water in contact with the magnetic clusters. Since the magnetic catalyst clusters block the tubes, this water could be water in short parts of the tube blocked at two sides by magnetic clusters. This line is already present at the lowest amount of added water and slowly disappears with increasing amount of water. Also it is not observed when the catalyst concentration is higher.

7.4 References to Chapter Seven

- [1] X.-P. Tang, A. Kleinhammes, H. Shimoda, L. Fleming, K. Y. Bonnoune, C. Bower, O. Zhou, Y. Wu, *Science* **2000**, 288, 492.
- [2] C. Goze Bac, S. Latil, L. Vaccarini, P. Bernier, P. Gaveau, S. Tahir, V. Micholet, and R. Aznar, *Phys. Rev B*, 2001, 63, 100302(R).
- [3] S. Mao, A. Kleinhammes, Y. Wu, *Chem. Phys. Lett.* **2006**, 421, 513.
- [4] S. Ghosh, K.V. Ramanathan, A.K. Sood, *Europhys. Lett.* **2003**, 65, 678.
- [5] A.I. Kolesnikov, J-M. Zanotti, C-K. Loong, P. Thiyagarajan, A.P. Moravsky, R.O. Loutfy, C.J. Burnham, *Phys. Rev. Lett.* **2004**, 93, 035503.
- [6] D.E. Barnaal, I.J. Lowe, *J. Chem. Phys.* (1966), 46, 4800.
- [7] Y. Maniwa et al., *Chem. Phys. Lett.* **2005**, 401, 534.
- [8] M.C. Gordillo, J. Marti, *Phys. Rev. B* **2003**, 67, 205425.
- [9] D.J. Mann, M.D. Halls, *Phys. Rev. Lett.* **2003**, 90, 195503.
- [10] J. Marti, M.C. Gordillo, *J. Chem. Phys.* **2001**, 114, 10486.
- [11] J. Marti, M.C. Gordillo, *Phys. Rev. B* **2001**, 63, 165430.
- [12] J. Marti, M.C. Gordillo, *Phys. Rev. E* **2001**, 64, 021504.
- [13] J. Marti, M.C. Gordillo, *J. Chem. Phys.* **2003**, 119, 12540.
- [14] G. Hummer, J.C. Rasalah, J.P. Noworyta, *Nature*, **2001**, 414, 188.
- [15] M.S.P. Sansom, P.C. Biggin, *Nature*, **2001**, 414, 156.
- [16] R.J. Abraham, J. Fisher, P. Loftus, *Introduction to NMR Spectroscopy*, **1988**, John Wiley and Sons.
- [17] C.W. Haigh, R.B. Mallion, *Prog. Nucl. Mag. Res. Sp.* **1980**, 13, 303.
- [18] W. R. Smythe, *Static and Dynamic Electricity*, 2nd ed. McGraw-Hill, New York, **1950**.
- [19] J.S. Waugh, R.W. Fessenden, *J. Am. Chem. Soc.* **1957**, 79, 846.
- [20] C.E. Johnson Jr., F.A. Bovey, *J. Chem. Phys.* **1958**, 29, 1012.
- [21] W. Sekhaneh, M. Kotecha, U. Dettlaff-Weglikowska, W. S. Veeman. *Chem. Phys. Lett.* **2006**, 428, 143.

8

Chapter Eight: Conclusions

From the Nuclear Magnetic Resonance investigations on water in single wall carbon nanotubes (SWCNTs), as described in this thesis, we can draw the following conclusions:

- Water is not absorbed inside SWCNTs, synthesized by the HiPCO method with a Fe catalyst, without further purification. The only water that is sorbed by the sample is water adsorbed at the outside of the nanotubes with a chemical shift of 4.6 – 4.8 ppm.
- Acid treatment removes the Fe clusters. After this treatment two water signals are detected, at 4.6 – 4.8 ppm and at 1.3 ppm.
- Temperature dependent NMR spectra show that the water which is responsible for the 1.3 ppm line freezes at a temperature much lower than the freezing point of bulk water. This water is assigned to water absorbed inside the nanotubes.
- The NMR spectra as a function of the amount of water added to the SWCNT sample shows that the first water that is added to the sample, is absorbed in the tubes. In spite of the hydrophobicity of the inside of the carbon nanotubes water is absorbed due to the water surface tension.
- The investigated sample contains SWCNTs with diameters ranging from 0.9 to 1.1 nm and different chiralities. Also from theory it is expected that the tubes can be divided in metallic and semi-conducting tubes. Nevertheless the diameter range, the chirality and the conductivity of the tubes seem to have no effect on the chemical shift of absorbed water.
- A simple model calculation using the ring current contribution of each benzene ring of the SWCNT to the chemical shift of water located at the centre axis of the tube yields a water chemical shift value very close to the experimental value of 1.3 ppm.

List of Publications and Participation in Conferences

W. Sekhaneh, M. Kotecha, U. Dettlaff-Weglikowska, W. S. Veeman. *Chem. Phys. Lett.* **2006**, 428, 143.

22. NRW-Frühjahrssymposium Magnetische Resonanz, Dortmund, 26. März 2002.
34th IFF Spring School - Fundamentals of Nanoelectronics. Research Center Jülich, Jülich, 10.March 2003 - 21.March 2003.
11. Anwendertreffen. Röntgenfluoreszenz und Funkenemissionsspektrometrie (X-Ray Spectroscopy). Deutscher Arbeitskreis für Angewandte Spektroskopie. Universität Duisburg-Essen. From 8.-9. March 2004.
35th - Physics Meets Biology, From Soft Matter to Cell Biology 22 March 2004 - 2 April 2004 . Jülich . Germany.
XIII International Conference on Hyperfine Interaction. XVII International Symposium on Nuclear Quadrupole Interaction. Bonn, Germany, 23. 8. - 27. 8. 2004. Helmholtz - Institut für Strahlen- und Kernphysik (institute of Radioactivity and nuclear Physics).
36th IFF Spring School - Magnetism goes Nano. February 14 - 25, 2005 . Jülich . Germany

CURRICULUM VITAE

Personal Details

Full name: Wassef Al Sekhaneh
Date of birth: 06th of November 1962
Telephone: (+49) 2102471538, (+49)17620913443, (+49) 2102531267
E-mails: Sekhaneh.wassef@uni-Duisburg.de
Sekhaneh@yahoo.de

Education

1981-1982 Secondary education at the Turra, Irbed School in Jordan.
1982-1986 Yarmouk University, Irbed, Jordan.
Bachelor of Physics.
1989-1995 Master in Science (M.Sc.)
2001-2008 Ph.D in Solid State NMR and Carbon Nanotubes, Duisburg-Essen University, Essen, Germany.

Work Experience

1986 - 1987 Teacher of Physics at Ministry of Education, Alturra, Jordan.
Sep. 1987 –1994 Teacher of Physics and mathematics at the Jordanian royal Airforce, Jordan and Al Balga university in Jordan
Aug. 2001 – May 2008 Ph. D at Duisburg-Essen University in Physics- Chemistry departments.

Wassef Al Sekhaneh